Alma Mater Studiorum – Università di Bologna

DOTTORATO DI RICERCA IN MODELLISTICA FISICA PER LA PROTEZIONE DELL'AMBIENTE

Ciclo XXII

Settore scientifico disciplinari di afferenza: FIS/06

Cold cloud climatology over Europe and the Mediterranean during the warm season from Meteosat IR imagery

Presentata da: Francesca Pinelli

Coordinatore Dottorato	**Relatori**
Prof. Rolando Rizzi	**Prof. Rolando Rizzi** **Dott. Vincenzo Levizzani**

Esame finale anno 2010

To my family.
To the paths I will follow.

Acknowledgments

Meteosat imagery was made available and is copyrighted by EUMETSAT.

Then I would thank the numerous individuals that have contributed in diverse ways to the completion of this study for which I am deeply thankful.

I thank Dr. Vincenzo Levizzani and the members of his research group Dr. Elsa Cattani, Dr. Francesca Torricella, and Dr. Sante Laviola for their suggestions and positive feedback which helped me a lot and for providing me with a pleasant work environment without which this work would never be possible. Thanks to Dr. Samantha Melani and Dr. Massimiliano Pasqui for their comments and interaction. Thanks to Dr. Roberto Ginnetti for his software assistance.

I thank Dr. Thomas Werner for his precious support that dated back from before I graduated.

I thank Prof. Richard E. Carbone for his invaluable suggestions and insightful discussions.

Thanks should be given to Dr. Jörg Schulz and the Deutscher Wetterdienst staff (scientific and technical) who helped me during my stay in Offenbach. A very brief but intense period!

I thank Prof. W. Paul Menzel, his research group, the team of the Remote Sensing summer school held in Benevento in the 2006 and all the students (Utkan in particular) that spent with me those exciting 10 days.

I am very much thankful to my family and all my friend that supported and assisted me in many ways. In particular thanks to Paola and Stefania for the time we spent together, physically close by or far away from each other: it was so helpful for me and contributed to encourage me in pursuing the task. Thanks, Silvia, for your friendship and moral support. Thanks, Cristina, for your hugs and your words that made me feel better when I was not much motivated.

Finally, thanks to everyone who believe that, if we want, we can change everything in our life in any moment, without repudiate our past, but becoming stronger and wiser by virtue of it…like I do!

Index

Index of figures

Index of tables

Abstract

Thermal infrared (IR, 10.5 – 12.5 μm) images from the Meteosat Visible and Infrared Imager (MVIRI) of cold cloud episodes (cloud top brightness temperature < 241 K) are used as a proxy of precipitating clouds to derive a warm season (May-August) climatology of their coherency, duration, span, and speed over Europe and the Mediterranean. The analysis focuses over the 30°-54°N, 15°W-40°E domain in May-August 1996-2005.

Harmonic analysis using discrete Fourier transforms is applied together with a statistical analysis and an investigation of the diurnal cycle.

This study has the objective to make available a set of results on the propagation dynamics of the cloud systems with the aim of assist numerical modellers in improving summer convection parameterization.

The zonal propagation of cold cloud systems is accompanied by a weak meridional component confined to narrow latitude belts. The persistence of cold clouds over the area evidences the role of orography, the Pyrenees, the Alps, the Balkans and Anatolia. A diurnal oscillation is found with a maximum marking the initiation of convection in the lee of the mountains and shifting from about 1400 UTC at 40°E to 1800 UTC at 0°. A moderate eastward propagation of the frequency maximum from all mountain chains across the domain exists and the diurnal maxima are completely suppressed west of 5°W. The mean power spectrum of the cold cloud frequency distribution evidences a period of one day all over Europe disappearing over the ocean (west of 10°W). Other maxima are found in correspondence of 6 to 10 days in the longitudes from 15° W to 0° and indicate the activity of the westerlies with frontal passage over the continent. Longer periods activities (from 15 up to 30 days) were stronger around 10° W and from 5° W to 15° E and are likely related to the Madden Julian Oscillation influence. The maxima of the diurnal signal are in phase with the presence of elevated terrain and with land masses.

A median zonal phase speed of 16.1 ms^{-1} is found for all events ≥ 1000 km and ≥ 20 h and a full set of results divided by years and recurrence categories is also presented.

1. Introduction

1.1 Literature review

Many aspects of the earth's water cycle are not well understood and the simulation of precipitation is still a problem for numerical weather prediction (NWP) models and climate system models; in particular warm season precipitation episodes represent a great challenge for quantitative precipitation forecasting (QPF).

The advent of non-hydrostatic and explicit models, together with the increasing spatial resolution of NWP models have further evidenced the low skills of QPF in the warm season (Olson *et al.,* 1995; Fritsch *et al.,* 1998) both in absolute terms and relative to predictions of the other seasons precipitation.

Several factors limit the predictability of warm season precipitation events. Among them, the different character and scale of precipitation events in winter with respect to summer. In fact, warm season precipitation is dominated by small-scale convective processes and less frequent mesoscale convective systems (MCS), that are difficult to be reproduced in the models, while during the cold season, synoptic-scale systems, marked by pronounced low-level warm-advection, tend to predominate. Additionally, warm season precipitation events occur with greater frequency at night (Maddox *et al.,* 1979), while cold season precipitation is more evenly distributed throughout the 24 h. Moreover, in winter, only 1 or 2 well organized weather systems may develop on a given day, on the contrary, during the warm season, there are likely to be several MCSs with lower predictability.

The extent to which warm season precipitation is intrinsically predictable is further limited by the nonlinear and chaotic nature of convective storms.

To some extent, the degree of predictability is dependent upon the longevity of coherent rainfall events. Apart from hurricanes, the longest reported duration of organized convective systems is associated with mesoscale convective complexes (MCC) and MCSs (Maddox 1980; Laing and Fritsch, 1997, 2000). As defined by satellite imagery-based criteria, MCCs have average lifetimes of 8 to 12 h in the Americas, China, Africa, and Australia.

The occurrence, characteristics, propagation and diurnal cycle of MCSs are found to be poorly represented in NWP models (Davis *et al*., 2003), which perform reasonably well only when rainfall maximizes in the late afternoon and remains a local phenomenon.

In general models have a premature onset of precipitation and produce precipitation that is too frequent and with insufficient intensity. The implication is that the build-up of instability that allows for heavy rainfall events to occur in nature fails to occur in models owing to a premature release of instability. The strong presence of a diurnal cycle in summer rainfall over land is also a clear indication of the influence of solar radiation, surface fluxes, and boundary layer processes, complicated by clouds and long-wave radiation effects.

Problems arise also when investigating the predictability of extreme warm season precipitation events, which lead to flooding conditions (Zhang *et al.*, 2008). The authors found that substantial improvements of the forecasting accuracy could be gained by refining the initial analysis and adopting better assimilation techniques or enhanced observations, together with the introduction of better resolved or parameterized physical processes.

A workshop was held in 2002 (Fritsch and Carbone, 2004) focusing on research needs for improving convective precipitation predictability in the warm season. Its conclusions dwelled on the necessity of improving process representation through adequate observing strategies for a better understanding of organized convection including factors associated with propagation, dissipation and regeneration.

The high societal impact of warm season rainfall, together with its implications for the hydrological cycle and feedbacks, such surface latent heat exchange and radiative effects of large cloud systems that persist during night-time, suggest the need for improvement in warm season QPFs that can be obtained through a better understanding of the development and the main features of the environment that characterize summer precipitation systems.

In recent decades, studies of the MCS life cycle and propagation together with the analysis of the internal structure and evolution of storms were conducted by several authors in various part of the world with the intention of improving our knowledge of summer convective processes.

In the United States (US), investigations on the lifecycles of MCSs have found that the majority of these systems initiate in the lee of the Rocky Mountains, move eastward and produce an overnight precipitation maximum across the central plains, sometimes while undergoing various cycles of regeneration (e.g., Maddox, 1980; Fritsch *et al.,* 1986; Augustine and Caracena, 1994; Anderson and Arritt, 1998; Trier *et al.,* 2000). Using the Weather Surveillance Radar-88 Doppler (WSR-88D) data, Carbone *et al.* (2002) reported the existence of coherent warm season precipitation patterns at continental scale with a zonal span up to 3000 km, and exhibiting durations well in excess of typical mesoscale convective lifecycles and characteristics of propagating events. These episodes often correspond to organized convection such as squall lines and MCSs and are frequently initiated in response to diurnal and semidiurnal forcing. The most interesting property of the episodes, however, is their longevity, which can be up to 60 h. This suggests an intrinsic predictability associated with warm season rainfall.

For the region of East Asia, Wang *et al.* (2004) developed a climatology of warm season precipitation episodes using infrared (IR) brightness temperatures from the Japanese Geostationary Meteorological Satellite-5 (GMS-5). They found that the major events of cold cloud cluster (or quasi-precipitation episodes) were on average smaller (for systems spanning more than 2500 km) and short-lived (up to 40 h) and tended to travel at a slightly faster speed than their North American counterparts, but their properties, including their coherent pattern and eastward propagation, were on the whole similar to precipitation episodes found in the US.

Laing *et al.* (2008) developed a similar climatology over Africa using IR brightness temperatures from EUMETSAT's Meteosat satellites. They showed that convection in Africa exhibits coherent patterns and propagating characteristics analogue to North America and Asia except for westward propagation. In particular, they found that in Northern Tropical Africa convective episodes tend to initiate in the lee of high terrain, which is consistent with the principles of thermal forcing from elevated heat sources. They propagate westward under the influence of moderate low to mid-tropospheric shear, which itself varies with the African Easterly Jet migration and the West African monsoon phases, and have zonal span and duration longer than those on other continental regions. The highest frequency of intense convection occurs close to local shear maxima near high terrain features and the average diurnal frequency maxima results from the superimposition of local diurnal maximum with the delayed phase arrival of systems propagating from the east.

The study of warm season cold cloud-top episodes in the Australian-Indonesian region has been recently undertaken by Keenan and Carbone (2008) using the GMS IR data as a proxy for rainfall. As this region spans from midlatitudes to equatorial regions, precipitation is related to such diverse forcing as monsoon, frontal zones, and subtropical influences under widely varying environmental flow. Additionally, Australian topography has a limited vertical extent with respect to the other regions. Nevertheless, "long episodes" of convective streaks, with a span and duration typically larger than those observed by Carbone *et al.* (2002), are found to consistently occur at all latitudes in the region, albeit with decreasing frequency poleward. The life cycles of these streaks are shown to be linked to diurnally forced heating associated with orography and land-sea contrast coupled with favourable synoptic conditions and coherent regeneration process. Compared to condition in North America and East Asia, in the Australian region transient synoptic-scale forcing seems to play a more important role, and the triggering of events by elevated terrain sources is clearly evident, but with a lower frequency.

The results of Carbone *et al.* (2002) and of other scientists around the world have allowed to show that the precipitation streaks occur globally in the lee of orography, with stronger streak intensity evident when the topography is steeper. These results, numerical simulation, and dynamical studies indicate that orography acts as an elevated heat source to initiate the organized convection when proper convective available potential energy (CAPE) and vertical wind shear profile are present. Organized convection travels at a speed determined by the interaction between the shear flow and the dipole heating (latent heat release aloft and cooling near the surface due to evaporation in downdrafts). As convection moves away from the mountains, it impacts the diurnal cycle of precipitation at location far away from the sources thus creating a sort of semi-diurnal precipitation events.

Another interesting aspect concerning warm season convective episodes, especially when such episodes exceed the duration of individual convective systems, is the understanding, and consequently the adequate representation in models, of coherent rainfall regeneration causes. Regeneration is often associated with drylines, colliding mesoscale “boundaries” (Wilson and Schreiber, 1986), gravity currents, bores, solitary waves, and other forms of trapped gravity waves (Carbone *et al.,* 1990; Crook *et al.,* 1990). Koch and O’Handley (1997) identified mesoscale gravity waves in unbalanced flow at synoptic scale as a regeneration mechanism. Investigations by some authors (e.g., Trier *et al.,* 2000; Davis *et al.,* 2002) have pointed out the significant role of mesoscale convective vortexes (MCVs) for the initiation of secondary convection that is likely crucial in extending the lifetime of precipitation episodes, even if it is suggested that other disturbances may prove to be equally or more important.

As regards to European and Mediterranean region, several studies based on reanalyses and/or ad hoc simulations have tackled the characterization of the areas of cyclogenesis, the seasonal dependence and the generating mechanisms of precipitation systems. Among others, Alpert *et al.* (1990a) and Trigo *et al.* (1999) used the European Centre for Medium-Range Weather Forecasts (ECMWF) 15-years reanalysis (ERA-15) to show that over 65% of Mediterranean cyclones have a radius less than 550 km and an average duration of about 28 h. Larger, short-living cyclones were found over the western Mediterranean by other authors spanning between 150 and 300 km. These and other studies have shown the existence of different generation areas and generating mechanisms, with strong seasonal and inter-monthly variability (Alpert *et al.,* 1990a, b; Trigo *et al.,* 1999, 2002). As is to be expected, the intensity of the cyclogenetic activity appears to be dominated to a large extent by large scale forcing. However, local forcing, as orography and latent heat release at the sea surface, plays a role.

Very few observational studies exist on the span and duration of convective precipitation systems in Europe although several studies have tracked individual storm systems over specific regions of Europe. For example, Schiesser *et al.* (1995) found that MCSs over Switzerland were not as well organized as those in the US and Hernandez *et al.* (1998) summarized the characteristics and environments of MCCs over the Iberian Peninsula and western Mediterranean during 1990-1994. Chaboureau and Claud (2003) have devised a technique based on the storm signature on clouds and precipitation as observed from the TIROS-N Operational Vertical Sounder (TOVS). They used three retrieval fields, temperature of the lower stratosphere, cloud top pressure, and precipitation index to characterize the intraseasonal variability of wintertime large precipitating systems over North Atlantic Ocean. Chaboureau and Claud (2006) have recently adapted their technique to Mediterranean cyclones, providing a typology of cloud systems for each season, to determine the proportion of lows for which the dynamics is dominated by the upper-level conditions and to examine the potential relationship between individual cloud systems and low-frequency variability.

Given the results obtained from the analysis of warm season precipitation in the other continents, and their likely connections, this study extends the work done by Levizzani *et al.* (2006) and aims to describe and understand the propagation characteristics of organized convection over Europe and the Mediterranean, using IR data from EUMETSAT's Meteosat satellites. This work represents a further contribution to the global study launched by the World Weather Research Programme (WWRP) in order to seek information on the possible universality of forcing, propagation, and the coherent regeneration of warm season precipitation. A paper on a major scientific journal (Levizzani *et al.*, 2010) largely dwells on the findings of the present research work and provides unprecedented results for the weather and regional climate modelling in summer over the area. These global studies are essential for QPF improvement and to improve the representation of the atmospheric part of the water cycle in climate models.

2. *The meteorological satellites*

2.1 Background

The meteorological and climatological community including global change, hydrology and oceanography all over the world are now able to take advantage of a wealth of observational data, products and services from highly sophisticated environmental observation satellites. An environmental observation satellite is an artificial Earth satellite providing data on the Earth system and a meteorological satellite is a type of environmental satellite specifically conceived for meteorological observations. Meteorological observations using meteorological satellites have several advantages compared with conventional ground-based observing systems so that environmental satellite data can be considered unique with respect to data from other sources. Some of the most important factors are:

- An environmental satellite can provide a regular supply of data from those areas of the globe yielding very few conventional observations, because of its high vantage point and broad field of view;
- The atmosphere is broadly scanned from satellite altitude and enables large-scale environmental features to be explored in a single view;
- The ability of certain satellites to continuously view a major portion of the atmosphere from space makes them particularly well suited for the monitoring and warning of short-lived meteorological phenomena; and
- The advanced communications systems developed as an integral part of the satellite technology allows for the rapid transmission of data from the satellite, or their relay from automatic stations on the Earth surface and in the atmosphere, to operational users.

These factors are incorporated in the design of meteorological satellites to provide data, products and services through three major functions:

- Remote sensing of spectral radiation which can be converted into meteorological measurements such as cloud top temperature, cloud cover, cloud motion vectors, surface temperature, vertical profiles of atmospheric temperature, humidity and atmospheric constituents and other various radiation measurements;
- Collection of data from *in situ* sensors on remote fixed or mobile platforms located on the Earth's surface or in the atmosphere; and

- Direct broadcast to provide cloud-cover images and other meteorological information to users through a user-operated direct readout station.

As regards meteorological satellites, geostationary and sun synchronous polar orbits have been mostly used so far.

A geostationary satellite, located at 36000 km above the equator, circles around the Earth above the equator with the same speed of the Earth rotation, so that it is seen at a stationary position from Earth and it enables continuous weather surveillance in almost real time.

The polar orbiting satellite circles the Earth over the north and south poles at low altitude (from 600 to 1600 km) and in a short period. It passes over the same point on the Earth only twice a day, so that global observations can be collected only every twelve hours, but it can observe the polar regions, which the geostationary satellite cannot.

The current space-based Global Observing System (GOS) is based upon both types of meteorological satellites (Fig. 2-1). The constellation of the various geostationary satellites operates in an equatorial belt and provides a continuous view of the weather from roughly 70° N to 70° S. A second constellation comprises the polar-orbiting satellites operated by the Russian Federation, the USA, the People's Republic of China and Europe.

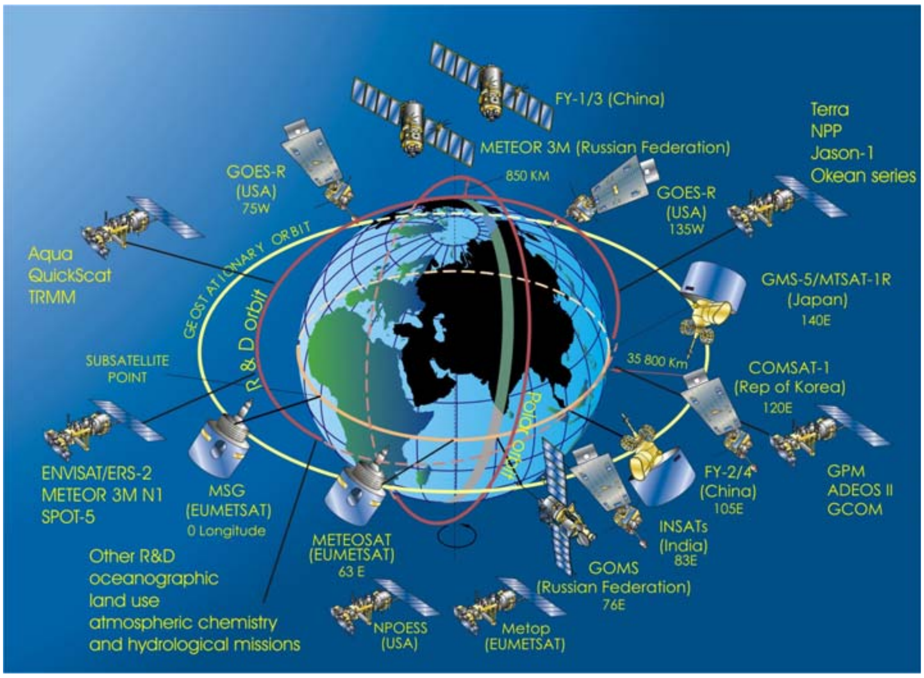

Figure 2-1 *The present satellite constellation of the Global Observing System.*

The ability of geostationary satellites to provide a continuous view of weather systems make them invaluable in following the motion, development, and decay of such phenomena. Even short-term events such as severe thunderstorms, with a life-time of only a few hours, can be successfully recognized in their early stages and appropriate warnings of the time and area of their maximum impact can be expeditiously provided to the general public. For this reason, its warning capability has been the primary justification for the geostationary spacecraft. Since 71 % of the Earth's surface is water and even the land areas have many regions which are sparsely inhabited, the polar-orbiting satellite system provides the data needed to compensate the deficiencies in conventional observing networks. Flying in a near-polar orbit, the spacecraft acquires data from all parts of the globe during a series of successive revolutions. For these reasons the polar-orbiting satellites are principally used to obtain daily global cloud cover and accurate quantitative measurements of surface temperature and of the vertical variation of temperature and water vapour in the atmosphere. There is a distinct advantage in receiving global data acquired by a single set of observing sensors. Together, the polar-orbiting and geostationary satellites constitute a truly global meteorological satellite network (NOAA/NESDIS Regional and Mesoscale Meteorology Branch RAMMB website: *http://rammb.cira.colostate.edu/*).

The following sections contain a brief overview of the satellites and of the instruments whose data have been used and analyzed in this work.

2.2 Meteosat First Generation

Meteosat First Generation is a series of geostationary satellites that have provided images of the full Earth disc and data for weather forecasts in a continuous and reliable stream for a quarter of a century. EUMETSAT, the European Organisation for the Exploitation of Meteorological Satellites, is responsible for the overall management and operation of this satellite system and provides the formal interface with the user community (EUMETSAT website: *http://www.eumetsat.int/Home/index.htm/*).

The first Meteosat, Meteosat-1, was launched in 1977, and the last of the first generation, Meteosat-7, 20 years later, in 1977. Each Meteosat First Generation satellite was expected to remain in orbit in an operational condition for at least five years. The policy was to keep two operational satellites in orbit and to launch a new satellite close to the date at which the older of the two came to the end of its fuel. The actual launch date took into account a number of other factors, such as the condition of both in-orbit satellites and the availability of launch partners. Table 2.1 documents the operational history of Meteosat First Generation.

Meteosat is a spin-stabilised satellite in geostationary orbit at an altitude of 35800 km. The operational satellite is located over the Gulf of Guinea, at the crossing of the Equator and the Greenwich meridian (0° North, 0° East). An operational stand-by satellite is located nearby close to

9° W. It should also be noted that an Indian Ocean Data Coverage (IODC) Service is provided by a Meteosat (currently Meteosat-7) from 63° E.

In 2002, the first Meteosat Second Generation (MSG, a significantly enhanced follow-on system to the previous generation of Meteosat) Meteosat-8 was launched, followed in 2005 by the second satellite, Meteosat-9.

Table 2-1 *Operational history of Meteosat First Generation.*

Satellite	**Period**
Meteosat-1	1977-October 1979
Meteosat-2	1981-1991
Meteosat-3	1988-1995
Meteosat-4	1989-1995
Meteosat-5	1991-2007
Meteosat-6	1993-2006
Meteosat-7	1997-2013

2.3 Payload

The main payload of Meteosat is a high resolution radiometer, the Visible and InfraRed Imager (MVIRI). It provides the basic data in the form of radiances from the visible (VIS) and IR parts of the electromagnetic spectrum. The satellite scans the full earth disc within a 30 minute period. In particular, the MVIRI acquires radiance data from the full earth disc during a 25-minute period, followed by a five-minute retrace and stabilisation interval. Scanning in the east-west direction is achieved through the rotation of the entire satellite, sweeping out a line of data during each spin. Scanning from south to north is achieved by stepping the direction of the telescope the equivalent of one line further north after each revolution of the satellite.

Each image covers a substantial portion of the Earth, centred at the sub-satellite point, which is over the equator and 0° longitude. The distorted perspective introduced by the Earth’s curvature makes quantitative use of the data less satisfactory at large distances from the sub-satellite point, but quantitative products are generated routinely for distances of at least 60° great circle arc.

The radiometer operates in three spectral bands, chosen in accordance with Meteosat's primary task of mapping the distribution of clouds and water vapour.

The VIS band (0.45 to 1.0 μm) is used for imaging during daylight. This band corresponds to peak solar irradiance; furthermore the atmospheric gases are fairly transparent to incoming and outgoing (reflected) solar radiation in this band.

The Water Vapour (WV) absorption band (5.7 to 7.1 μm) is used in determining the amount of water vapour in the upper troposphere. It takes advantage of the strong absorption of emitted terrestrial radiation by atmospheric water vapour. In this spectral region, the atmosphere is very opaque if water vapour is present, but transparent if the air is very dry.

The Thermal IR band (10.5 to 12.5 μm is used for imaging day and night, and also for determining the temperature of cloud tops and of the ocean's surface. This band corresponds to peak re-emission of radiation from the Earth's surface and atmosphere, according to their temperature. As with the VIS band, the atmospheric gases are fairly transparent in this region.

The spatial resolution at nadir is of 5 km for the IR and WV bands and of 2.5 km for the VIS one.

The optical system of MVIRI consist of a scanning Ritchey-Chretien telescope with a primary aperture of 400 mm diameter (140 mm secondary aperture) and focal lengths of 3650 mm for VIS and 535 mm for WV and IR ranges. A series of mirrors is used to collect the incoming radiation and to focus it onto the corresponding detectors (silicon photodiodes for VIS, HgCdTe detectors for IR and WV).

The original data (counts) of the radiometer have to be converted into radiances and then, for the IR band, into brightness temperatures.

The relation used to convert counts into radiances is:

$$R = \alpha \times (C_{nt} - C_O) \qquad (2\text{-}1)$$

where R is the radiance, α is the calibration coefficient, C_{nt} is the count of the sensible element and C_O the count measured when the telescope is directed towards space (cold space view).

The MVIRI calibration is provided by two black bodies located on opposite sides of the main optical path, one at 290 K and the other at 340 K. Each data file transmitted to the users contains the calibration coefficient.

The radiance (measured in W m^{-2} sr^{-1}) being emitted by a blackbody for a particular wavelength is dependent from its temperature (K) and is given by Planck's Law:

$$R_\lambda(T) = \frac{2hc^2}{\lambda^5\left(e^{\frac{hc}{\lambda kT}} - 1\right)} \qquad (2\text{-}2)$$

where R is the radiance, h the Planck's constant, c the speed of light and k the Boltzmann's constant.

Appropriate temperature/radiance conversion tables are provided by EUMETSAT and have to be applied to convert radiances into brightness temperatures. There are different tables for each spacecrafts. To facilitate the process, an accurate exponential fit of the above mentioned tables can be used. For this work, regression coefficients for the relationship between radiance (W m^{-2} sr^{-1}) and brightness temperature (T_b, in K) for the IR channels of Meteosat-5 through Meteosat-7 have been computed. The analytic form of the relationship is:

$$R(T) = e^{\left(A + \frac{B}{T}\right)} \qquad (2\text{-}3)$$

where R is the radiance (W m^{-2} sr^{-1}), T the brightness temperature (K), and A and B regression coefficients (A > 0 dimensionless, B < 0 in K) that depend from the radiometer and from the band considered. For the IR channel this equation fits experimental data measured at a temperature of 90 K. The rms error of the brightness temperature is less than 0.2 K in the temperature range 200 – 330 K.

3. The analysis method

3.1 Correspondence between brightness temperature and precipitation

In the thermal IR band (10.5 to 12.5 µm) the atmosphere is relatively (but not completely) transparent as atmospheric gases do not efficiently absorb the radiation coming from the surface of the Earth. Therefore, the radiation emitted by the surface can be transmitted upwards (Fig. 3-1).

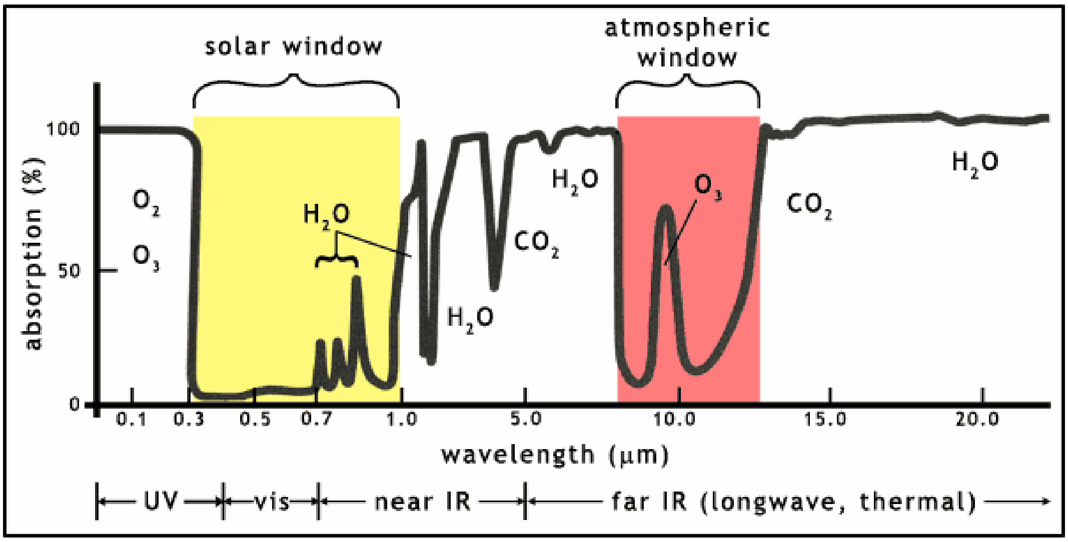

Figure 3-1 *Earth's atmosphere percentage absorption*

The interaction of the clouds with radiation in this spectral range is different. In fact, because of their chemical composition and optical properties, clouds absorb nearly all of the IR incident radiation, behaving essentially as blackbodies.

At a particular wavelength, the radiation emitted by clouds depends on their temperature and thus on their height. Moreover, the outermost cloud layers absorb the radiation emitted by the inner cloud layers, so that the radiation emitted from the clouds comes essentially from the external layer. Therefore, the measure of the satellite sensor in the thermal IR is the measure of the radiance (then converted into T_b) coming from cloud top and/or the side of the cloud, depending on the viewing geometry.

Precipitation estimations based on IR data are necessarily indirect as the radiation does not penetrate through the cloud, so that IR-based techniques estimate precipitation falling from the cloud base dwelling on radiation coming from the top and/or the side of the clouds. A cloud's brightness temperature may be related to the rain falling from it, but the raindrops themselves are not directly sensed.

Because of the indirect nature of the relationship between satellite-measured IR radiance and precipitation, IR-based techniques are not universally applicable. Furthermore, other factors influence the relation between cloud top brightness temperature and precipitation, as cloud type, cloud evolution stage, temporal resolution of the estimation and latitude, so that a precipitation estimation technique should be applied within its applicability context. The reader is encouraged to see Kidder and Vonder Haar (1995) for a more detailed description of precipitation-estimation techniques.

The most important properties of convective clouds useful for this study and stemming from research on precipitation estimation techniques are:

- There is a high correlation between a cloud's area (as measured in VIS or IR wavelengths) and the total volume of rain per unit time falling from it (Lovejoy and Austin, 1979).
- There is little correlation between the visible brightness or IR temperature of a point and the rain rate beneath that point (Lovejoy and Austin, 1979; Weiss and Smith, 1987).

The first property has been confirmed by means of radar data. Doneaud *et al*. (1984) and Lopez *et al*. (1983) have shown that the volume of rain that falls from a convective cloud through its lifetime is insensitive to the details of precipitation structure; only the raining area is important.

The second property is a result of the fact that there is no universal relationship between rain and what is observable on the outside surface of the cloud, which is what visible and IR instruments sense.

In view of these considerations, the first aim of the present study is to produce a 10 years climatology of warm season precipitation systems over Europe and the Mediterranean using Meteosat IR brightness temperature. Cold cloud persistence, span and duration of weather systems were determined to derive the zonal propagation speed and daily cycles.

3.2 Data and methods

3.2.1 Data selection and analysis domain

To obtain a climatology of warm season precipitating cloud episodes in Europe and the Mediterranean and to compare the results with similar studies in different geographical areas (i.e., Carbone *et al.,* 2002 and Wang *et al.,* 2004, 2005), the data source needs to cover the entire region and have acceptable spatial and temporal resolutions.

Given that a suitable dataset of rainfall rates from ground radar networks covering the area of study was not available, the data used for our purpose are the Meteosat First Generation Infrared (IR) T_b provided by EUMETSAT. Low Meteosat IR T_bs were employed to identify cold cloud tops which serve as a proxy for rainfall area identification.

In the present study, a threshold technique is used to identify the cold cloud systems that are more likely to be precipitating from IR data, as done by Wang *et al.* (2004) and Levizzani *et al.* (2006), while in Carbone *et al.* (2002) radar reflectivity were used to identify all areas connected with precipitation.

It's worth noting that compared to radar reflectivity, the IR T_b is usually less correlated with rainfall amount and does not always indicate active deep convection. Nevertheless, IR thresholding techniques have long been used to identify clouds and to estimate precipitation (e.g., Arkin and Xie 1994; Griffith *et al.,* 1978) and therefore can serve as a proxy for rainfall although the precise relationship between T_bs and rainrate is unknown.

The domain of analysis was selected considering the prevailing low-level flow, the continental boundaries, and tracks of precipitating systems. The latitudinal and longitudinal range of the domain are 30-54° N and 15° W-40° E, respectively (Fig. 3-2). The northernmost latitude limit is fixed by the stretching of Meteosat image pixels, which determines an increasing degradation of the spatial resolution when moving away from the equator.

Figure 3-2 *Domain of analysis: 30°- 54° N; 15 ° W- 40° E.*

3.2.2 Hovmöller diagrams

The Hovmöller diagrams are time-distance plots commonly used for the diagnosis of coherent signals in climate science and recently applied as a tool at the mesoscale to study the life cycle of precipitation systems (e.g., Carbone *et al.*, 1998; Knupp *et al.*, 1998; Wilson *et al.*, 2001).

In general, a Hovmöller diagram maps a scalar quantity to the time-distance space. The scalar variable is averaged along the spatial dimension (or dimensions) orthogonal to the spatial dimension plotted in the diagram.

The analysis methodology applied for this study is based on Hovmöller diagrams as already used over other geographic areas (North America - Carbone *et al.,* 2002; East Asia - Wang *et al.,* 2004; Australia – Keenan and Carbone, 2008; the Bay of Bengal – Liu *et al.*, 2008).

The method aims at reducing the dimensions of the dataset from three to two permitting to evidence the coherency, the propagations and the decay of the systems.

In particular, the original brightness temperature data are arranged in a three dimensional space: longitude, latitude and time. A clear graphical representation is obtained averaging along the longitude or the latitude dimension. Most of our diagrams exhibit longitude as the distance dimension, since the zonal component is the dominant propagation direction of cloud systems over the European domain.

The domain is divided into 1100 vertical strips of 0.05° (~ 4 km) spanning from 30 to 54°N in the North-South direction.

The procedure adopted in this work for drawing Hovmöller diagrams presents some differences with respect to the one adopted by Carbone *et al.* (2002) and Wang *et al.* (2004).

Carbone *et al.* (2002) took the average of the rainfall rate values, obtained from radar reflectivity data, within each strips of the latitude/longitude grid. Similarly, Wang *et al.* (2004) took the average of brightness temperatures of all pixels that fall inside each strip of the latitude/longitude grid with temperatures below 273.15 K, in order to consider the effect of background temperature, and then applied a threshold value of 241 K to identify likely precipitating systems in the Hovmöller diagrams.

For the present study, the results of a preliminary sensitivity analysis on the Hovmöller diagrams indicated that a cloud-top T_b threshold of 241 K effectively identifies the convective systems that span over Europe and the Mediterranean region against the warmer background. Thus, the data points in the Hovmöller diagrams don't represent the mean of all brightness temperature values falling within each strip of the latitude/longitude grid, but the average takes into account only the T_b lower or equal to the threshold value. This procedure allows us to better identify convective systems using a different threshold temperature from that applied by Levizzani *et al.* (2006) over the same domain of analysis.

After various sensitivity analyses, a cloud-top brightness temperature threshold value of 241 K has been identified as appropriate to the convective systems over the area under consideration.

The quantitative analysis of warm season European precipitating systems, is based on the application of a two-dimensional (2D) autocorrelation function to the T_b data in the Hovmöller longitude-time space. The function is rectangular in one dimension and weighted by a negative cosine in the other (Fig. 3-3), since a lower cloud-top temperature corresponds to stronger rainfall/convection. This function lends itself to quantify coherence, longevity, zonal distance (hereinafter referred to as "span") and propagation speed of the events. The 2D function was stepped through all grid points in the Hovmöller space and was rotated until the correlation coefficient maximized. Sequences of contiguous "fits" define the coherent span, duration, and propagation characteristics for each cloud streak. The cloud top temperature threshold to initiate a fit is 241 K, and a correlation coefficient of 0.35 is required for the fit to become part of the statistics. Sequences of contiguous fits in the Hovmöller space defined the coherent cloud patterns (i.e., cloud streaks), and the span, duration, and averaged propagation speed of cloud streaks were obtained using their end points.

For the purpose of the propagation and of span/duration statistics, the rectangular pulse of the function is ~ 4° long and the time dimension selected is 3 h, comparable to the size of individual MCSs .

Note that the span and duration statistics derived from satellite IR T_bs with this method are highly dependent upon the T_b threshold used, but the appropriate choice of the threshold can be brought into good agreement with those based upon radar data (Tuttle *et al.*, 2008). Upon comparing radar- and satellite-derived speed statistics over the United States these authors found that the propagation-speed statistics of satellite events are on average ~ 4 m s^{-1} faster than radar events and are relatively insensitive to threshold T_b.

To gain a better graphical representation of cloud streaks, the Hovmöller diagrams are plotted using a threshold T_b = 251 K, a value higher than the threshold value applied to the 2D autocorrelation function to find the cloud streaks.

A set of averaged Hovmöller diagrams has been created to examine the phase-locked behaviour of cold cloud signals at diurnal and higher frequency. Every cold cloud top with T_b lower than 241 K constitutes an "event" at a given longitude-time coordinate. The cumulative event frequency is then averaged for monthly and seasonal periods permitting to investigate the regional, intraseasonal, and interseasonal variations.

Finally, the periodicity of cloud patterns was studied applying the discrete Fourier transforms (DFT) to different portions of the domain and obtaining the power spectra of time series of averaged cloud-top T_b in the longitude-time Hovmöller space, at period both longer and shorter than 1 day.

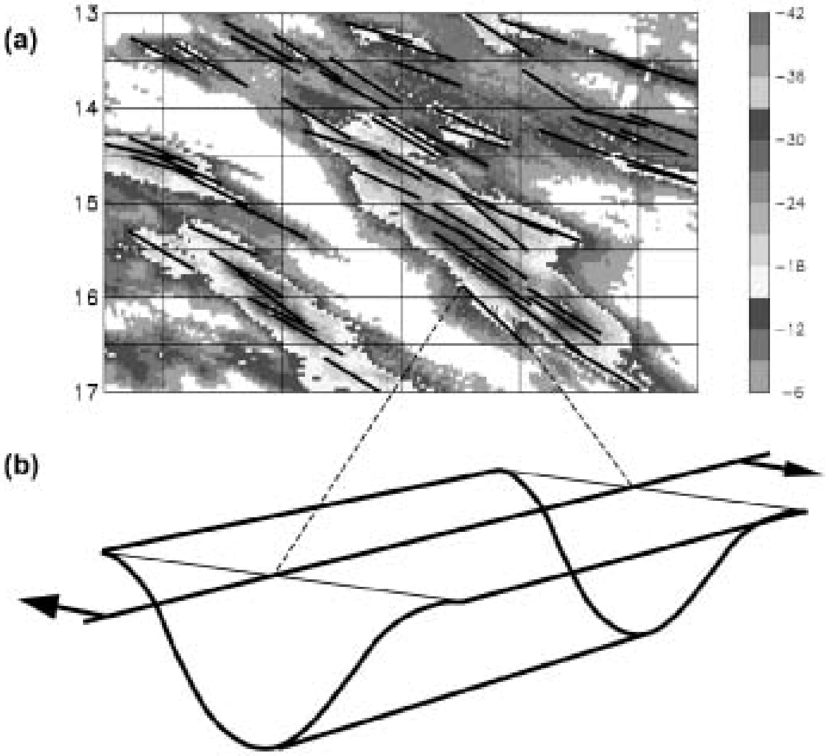

Figure 3-3 *(a) Example of autocorrelation fits superimposed on an Hovmöller diagram, and (b) schematic illustration of negative cosine-rectangular weighting function (Wang et al., 2004).*

3.2.3 Hovmöller diagrams interpretation

In the Hovmöller diagrams the reduction of the dimensions realized through the averaging process causes the information regarding the position and the kind of phenomena generating the streaks to be lost. In the time-longitude diagram, a streak is identified when the pixels have a mean lower than the threshold value, in the instant or in the time interval considered, and along contiguous longitudinal bands. This condition can be satisfied when the geographical area is subject to:

(i.) The passage of synoptic systems, as cyclones, anticyclones, and fronts.
(ii.) The propagation of a convective system.

The (i) condition is realized through spatial dimensions of about a thousand km, and temporal dimension of 3-4 days, typical of synoptic systems. The effect of this kind of systems is not significant in our domain of analysis during the warm season. The higher latitudinal position of the Polar Front in this season cause the synoptic systems to deviate toward higher northern latitudes and not to be significantly present in our domain, in particular regarding the more southern part. In addition, the cloud top temperatures of these systems are in general 20-30 K higher than those of convective clouds. Therefore we can say that the application of a threshold values of 241 K to cloud top temperatures and the method of averaging only the values that correspond to the coldest system in the longitudinal bands, cause synoptic systems to give only a minimum contribution to the streak signal.

We have to make some considerations about the condition (ii). The development of single cell thunderstorms requires local forcing of convection to be initiated on specific areas. The typical duration of these thunderstorms (less than 1 h) is consistent with Meteosat time resolution (0.5 h): the detection of a single cell thunderstorm depends on the cloud top temperature that characterises the system in its evolution life stage, when the satellite scans it.

The typical spatial dimension of single cell thunderstorm is consistent with satellite spatial resolution, too. Therefore the detection of these weather systems depends also on their position. The signal coming from a single cell thunderstorm will be reduced when it is collocated within the boundary of contiguous pixels, because the detected brightness temperature is a mean of the thunderstorm brightness temperature and the background temperature. In view of these considerations, we can conclude that the streaks represented in the Hovmöller diagrams correspond to propagating convective systems, nearly totally.

It’s worth noting that relevant convective systems have a latitudinal development when initiated from a frontal system, while their development is longitudinal in case of thermal forcing. These observations can give some information about the geographical positions of the convective systems in the Hovmöller diagram. In general to clarify convective systems positions in the domain, the analysis of cold cloud top persistence has been considered.

4. Analysis of warm season convective cloud systems over Europe and the Mediterranean

4.1 Study domain characteristics and data

The domain of study extends from 30° to 54° N and 15° W to 40° E incorporating a major part of Europe, the Mediterranean and Northern Africa costal area.

The latitudinal upper limit of the analysis domain was selected considering the stretching of Meteosat pixels and the fact that, even if the Scandinavian Peninsula belongs to Europe, it is not relevant with respect to the study of warm season convective episodes. To reach a better knowledge of convective system propagation characteristics, the eastern part of the analysis domain was extended beyond the European borders. Also in order to evaluate the propagation of the convective systems the eastern part of the analysis domain was extended beyond the European borders.

As shown in Fig. 4-1, the main topographic feature of the domain is the presence of several mountain ranges, the Alps, the Pyrenees, the Balkans, the Carpathians, the Atlas and the Anatolia Plateau.

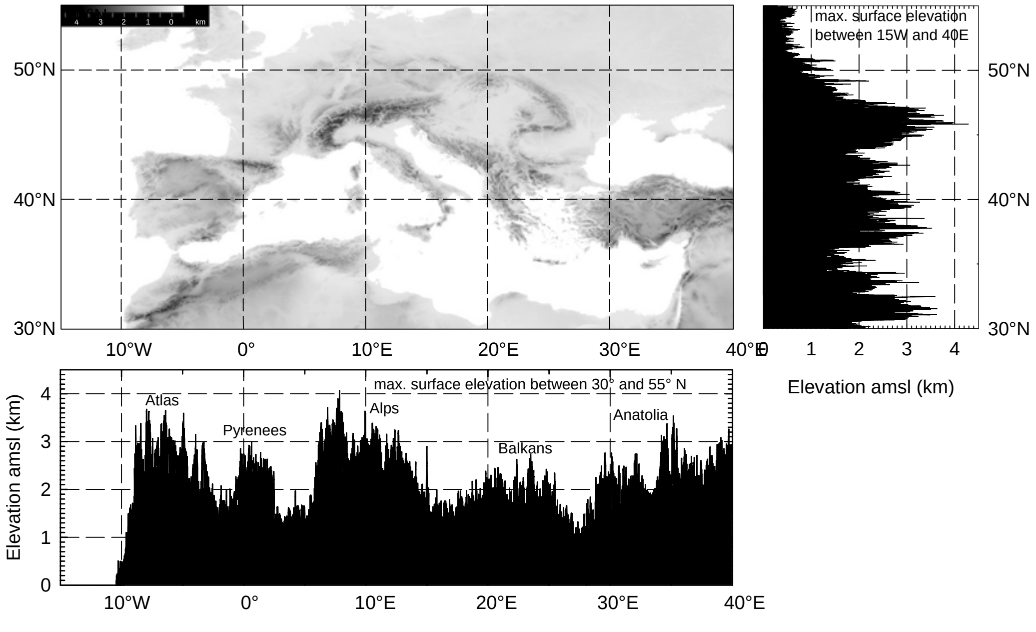

Figure 4-1 *Orography of the selected area of analysis with the major mountain chains.*

The climatology of warm season precipitation is derived using Meteosat IR data. In particular, radiances from the MVIRI IR spectral band (10.5 – 12.5 μm) were extracted from the archive of EUMETSAT for the 1996 – 2005 warm season period, May to August, and T_bs were computed using the instrument's calibration. The IR images have a spatial resolution of 5 km × 5 km at the sub-satellite point (0°, 0°) and are available at 30 min intervals; the resolution at Southern European latitudes degrades down to 7 km × 8 km. These resolutions are both lower than those of the radar data utilized by Carbone *et al.* (2002) (2 km × 2 km, 15 min), but were considered sufficient for the identification of cold cloud systems. Moreover, they are similar to the resolutions of the IR data used by Wang *et al.* (2004) (5 km × 5 km, 1 h).

The analysis method is based on Howmöller diagrams and a threshold technique is applied to identify the cold cloud systems that are most likely to be precipitating.

Note that, because of the indirect relation between cloud top brightness temperature and rainfall amount, not all cases in our analysis necessarily represent systems with rainfall reaching the ground throughout their duration, but cirrus and anvil emanating from convective clouds could have affected it. Even if this kind of cirrus contamination is certainly present in the analysis, Wang *et al.* (2004) reported a comparison of the structure of data in the thermal IR and the water vapour channels that demonstrates that it does not represent a real problem. Surface temperature variations in cloud free areas is another issue to be considered and the chosen threshold cloud top temperature takes care of this aspect too.

4.2 Examples of coherent cloud patterns

In this section, the summer 2002 is examined in detail to gain an idea of the cloud systems propagating over the area and of the correspondence of the various types of cloud streaks and the meteorological systems they synthetically describe.

Hovmöller strips of 0.05° longitude were drawn through our analysis domain, causing the meridional information to be lost, but preserving the zonal component of the flow. Within these diagrams, organized convective systems appear in effect as longitude-time streaks.

A few examples of longitude-time Hovmöller plot of the IR brightness temperature for the warm seasons of 1997 and 2005 are also presented to show the characteristics of the coherent clouds patterns.

The two warm seasons were chosen in order to evaluate the variety of European warm season cold clouds events, as the 1997 was considered a relatively "wet" year, while 2005 was relatively "dry".

The analysis focuses on the characteristics of the organized cloud streaks and their intraseasonal variation over the period from May to August.

A qualitative comparison with previous studies (Carbone *et al.,* 2002 and Wang *et al.,* 2004) has been realised, too.

The feature of the global atmospheric circulation that influences the weather and the climate of Europe and Mediterranean during the warm season is the subtropical anticyclone over the North Atlantic Ocean basin, commonly referred as "Azores high" (Davis *et al.*, 1997). The present study doesn't aim to give full account of all the aspects of the variability and the effects of the North Atlantic Subtropical Anticyclone on European and Mediterranean weather and climate during the period from May to August, rather we focus on some general aspects.

The Azores High is a semi-permanent anticyclonic region located over the Atlantic Ocean around 30° N in winter. The poleward movement of the system in summer has an impact upon the climate of Europe. In summer the pressure centre shifts towards 35° N and a ridge might build up across France, northern Germany and even the south-eastern United Kingdom, a situation associated to the typical mid to late summer heat waves arrival. Changes in the position and strength of the anticyclone can be rather abrupt, manifesting themselves with semi-monthly periods. In general, early May marks the beginning of rapid anticyclonic expansion, strengthening, and northward migration that continues through late July. The weakening of the Azores high begins in early August and continues through the winter. The summer position of the anticyclone, that can extend north-eastward toward western Europe, causes the cyclonic storm systems to track well to the north of the high between 45° and 50° N and move towards the British Isles. During the summer season, the southern part of the anticyclone can be joined with the subtropical African anticyclone, that, to alternate periods, reaches Southern Europe. This situation is characterised by stable weather conditions over central-southern Europe with some thunderstorms caused by thermal forcing, while the northern and western boundaries of the anticyclone are interested by the passage of Atlantic systems.

4.2.1 Cloud streaks and intraseasonal variations: The year 2002

Coherent cloud patterns during the warm season are shown in Fig. where the longitude-time Hovmöller diagrams for the May-August period of 2002 are presented together with examples of typical cloud systems depicting the meteorology in the area in various months.

Figure 3-2 shows the monthly Hovmöller diagram for the period 1-31 May 2002. First, note that almost all cloud patterns are sloped from the upper left to the lower right of the diagram thus indicating a clear coherent eastward propagation as is to be expected over Europe where the circulation is dominated by westerly wind systems. Four snapshots of typical IR images during the month are illustrated in Fig. 4.2.

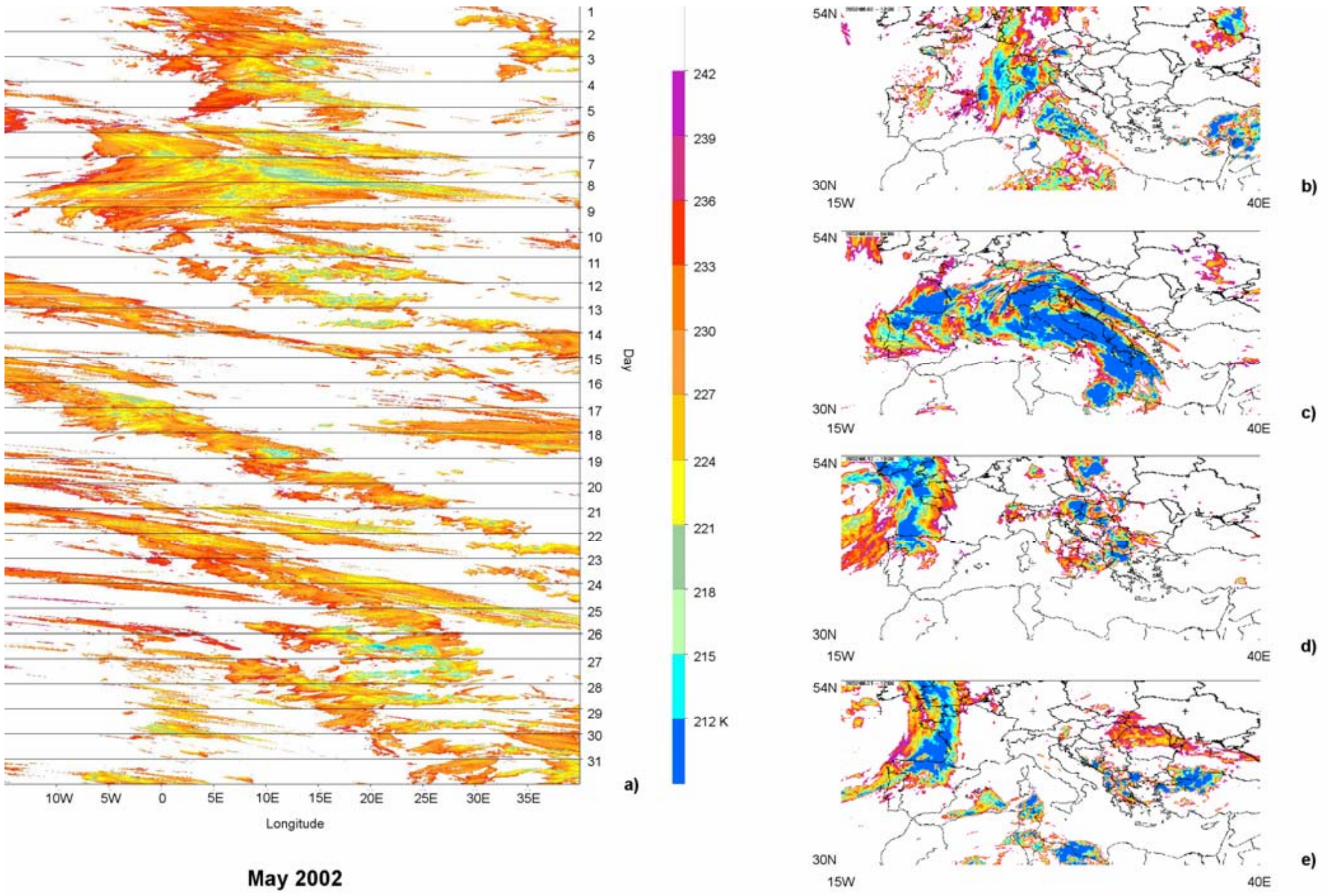

Figure 4-2 *May 2002. a) Longitude-time Hovmöller diagram of cloud top T_b (in K). Note that all data pairs characterized by a T_b > 242 K fall in the top category in white as they are not retained for the quantitative analysis. b) 2 May 1330 UTC, IR T_b of cloud tops > 242 K. c) 8 May 0400 UTC. d) 12 May 1830 UTC. e) 21 May 1200 UTC.*

The first few days of the month are still characterized by a spring circulation driven by Atlantic fronts that bring large convective systems embedded in the frontal stratiform clouds (Fig. 4-2b, 2 May 1330 UTC). The situation on 8 May 0400 UTC (Fig. 4-2c) depicts an evolution in the circulation with large frontal systems travelling from the African continent towards Europe; the convective cloud systems are continuously fed by warm moist air with a large cyclone standing in the middle of the Mediterranean. When the cyclonic activity fades away the area starts to be dominated by local summer convective phenomena driven by solar heating all over the continent, which propagate eastward downwind of the main mountain chains (Fig. 4-2d, 12 May 1830 UTC); at the same time fronts continue to break in over Western Europe from the Atlantic. The summer anticyclone then establishes itself over Central Europe and the Mediterranean with front travelling higher up over northern Europe (not shown). The last part of the month is dominated by a temporary disruption of the anticyclone with frontal activity and widespread convection over the continent as seen in Fig. 4-2e for 21 May1200 UTC.

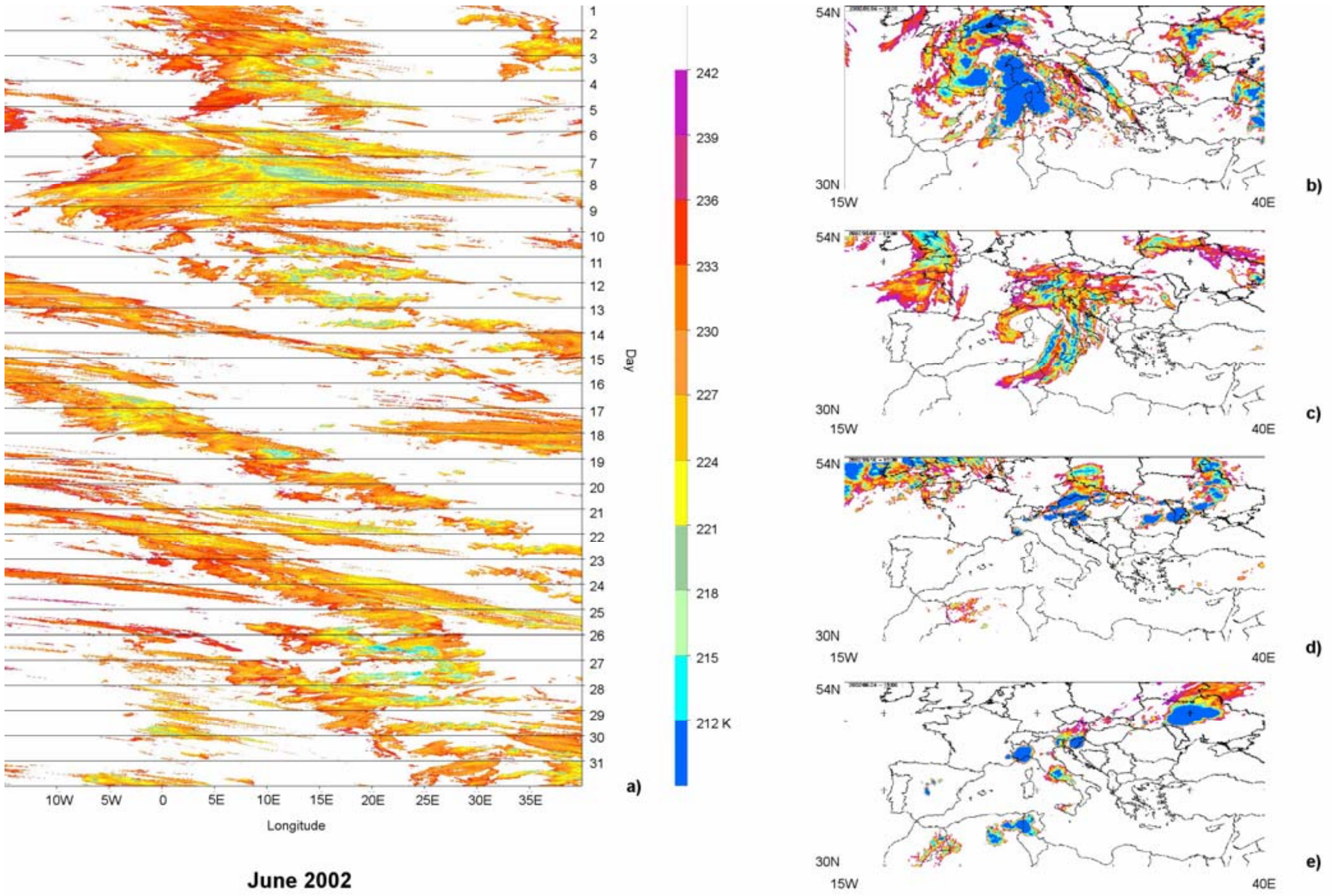

Figure 4-3 *Same as in Fig. 4.2 but for June 2002. a) Longitude-time Hovmöller diagram. b) 4 June 1830 UTC. c) 9 June 0100 UTC. d) 16 June 1530 UTC. e) 24 June 1500 UTC.*

Figure 4-3 describes the propagation of cloud systems for the period 1-30 June, 2002. The first three days of the month are characterized by a weak activity in the western sector with cloud systems travelling north of the Alps and convection developing over Turkey and Eastern Europe, but scarcely propagating. On June 4 (see Fig. 4-3b, 1830 UTC) a large low pressure system develops over Western Europe and extends all over the continent and the Mediterranean till June 6. This opens up the area to the influence of a successive system from North Africa (not shown). The successive strong cyclone originates from an Atlantic disturbance on June 8 and produces large cloud systems, which propagate eastward over the Mediterranean (Fig. 4-3c, 9 June 0100 UTC), while other systems continue to propagate over Eastern Europe. A period of relative scarce activity then follows with more local cloud systems or confined at high latitudes, as is typical of summer conditions in the area. Around the middle of the month several convective cloud systems develop over Central and Eastern Europe influenced by the Carpathians (Fig. 4-3d, 16 June 1530 UTC). Towards the last part of the month (Fig. 4-3e, 24 June 1500 UTC) other large convective systems develop over the Alps, the Apennines and the Balkans and shift eastward.

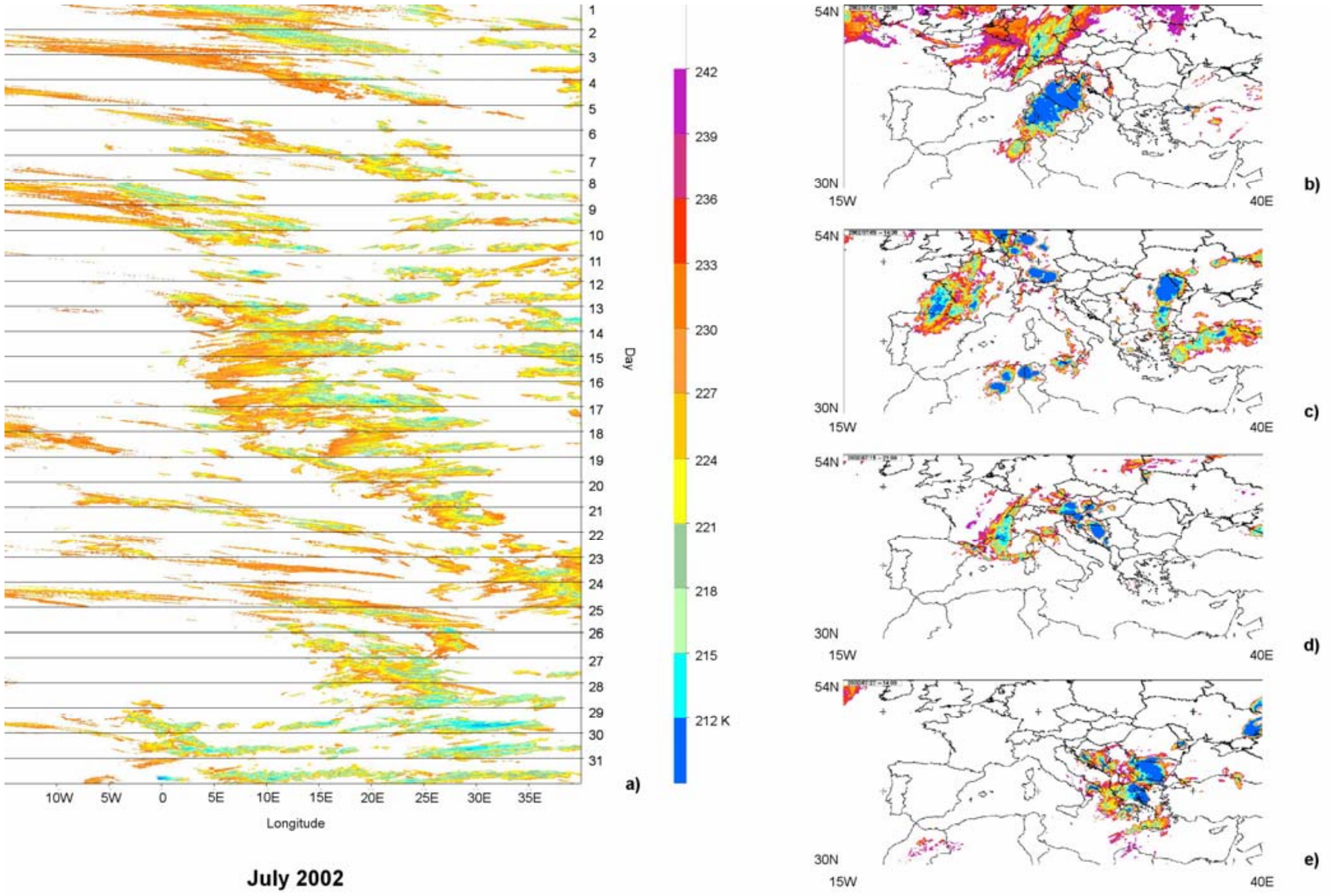

Figure 4-4 *Same as in Fig. 4.2 but for July 2002. a) Longitude-time Hovmöller diagram. b) 2 July 0500 UTC. c) 9 July 1430 UTC. d) 15 July 2100 UTC. e) 24 June 1500 UTC.*

The successive 1-31 July 2002 period is shown in Fig. 4-4. July starts with a frontal system that travels high in the area and a mesoscale convective system that occupies the Central Mediterranean moving eastward on July 2 (Fig. 4-4b, 2 July 0500 UTC). The high latitude cloud systems continue to move eastward till a frontal system breaks in on 8 July determining a widespread instability over Western Europe with storms distributed from North Africa to France and Germany; at the same time several convective systems develop over Eastern Europe and Turkey (Fig. 4-4c, 9 July 1430

UTC). The central part of the month is characterized by an intense convective activity over Eastern Europe from the Balkans to the Ukrainian plains with a daily modulation and at various intensity degrees. A low pressure system develops over Central Mediterranean on 14 July, which drives the circulation with intense convection in the lees of the Alps and the Balkans (Fig. 4-4d, 15 July 2100 UTC). The Eastern European convection continues for several days afterwards with heavy storms over Romania, Bulgaria, the Black Sea and Ukraine; at the same time fast moving systems travel over northern Europe. A depression over the Balkans and the Greek peninsula characterizes the last portion of the month with several convective systems developing in the area for several days (Fig. 4-4e, 27 July 1400 UTC).

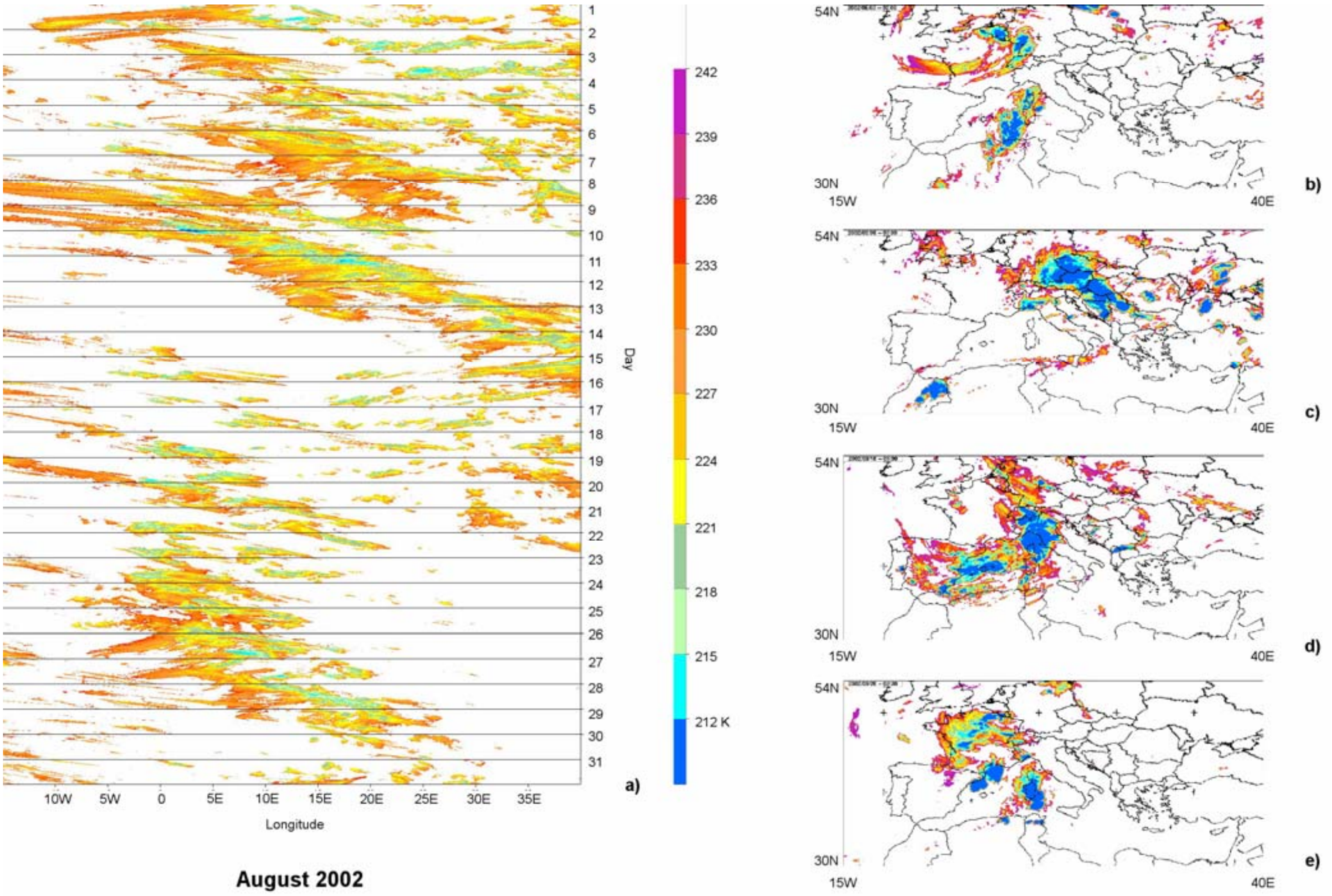

Figure 4-5 *Same as in Fig. 4.2 but for August 2002. a) Longitude-time Hovmöller diagram. b) 3 August 0200 UTC. c) 6 August 0300 UTC. d) 10 August 0500 UTC. e) 26 August 0330 UTC.*

Figure 4-5 shows the Hovmöller diagram and four snapshots of the 1-31 August 2002 period. The first decade of the month is marked by fast moving fronts over France and Central Europe followed by a depression centred over France and a series of convective systems moving from North Africa towards the Central Mediterranean (Fig. 4-5b, 3 August 0200 UTC). In the following days several convective systems pass over Central Europe travelling fast towards the east, some of them very large (Fig. 4-5c, 6 August 0300 UTC). The situation then continues to be dominated by a westerly flow with successive fronts and a large frontal system develops moving across the continent and the Mediterranean (Fig. 4-5d, 10 August 0500 UTC), eventually transforming into a large cyclonic system in transit to Eastern Europe. Short-living convective systems characterize the meteorology of the next days and a system of African origin takes over the scene in the last part of the month (Fig. 4-5e, 0330 UTC).

4.2.2 Cloud streaks and intraseasonal variations: The years 1997 and 2005

Coherent cloud patterns during the warm season are shown in Fig. 4-6 to 4-13.

Figure 4-6 presents the monthly Hovmöller plots for May 1997. First, note that clouds patterns were spreads across all the longitudinal domain. Almost all clouds patterns are sloped from the upper left to the lower right of the diagram thus indicating a clear coherent eastward propagation as is to be expected over Europe where the circulation is dominated by westerly wind systems. Sloping streaks of that kind usually correspond to some form of organized convection, such as a squall line or an MCS.

Similar patterns were also observed by Carbone *et al.* (2002), Wang *et al.* (2004) and recently by Keenan and Carbone (2008) in the respective domains of analysis.

The most significant eastward propagating systems, such as the events on 9-11, 13-15 and 21-23 May, were originated in the range of longitude from 10° W to 0°, where the Atlas and the Atlantic coasts are located. Some episodes had their source region in the westernmost part of the domain, indicating cloud systems coming from the Atlantic Ocean, such as those happened on 1-3, 6-7 and 18-19 May.

Another interesting aspect to note is the presence of westward propagating episodes. They were originated in the 10° - 3° W longitudinal band mainly during the second half of May and were probably associated with easterlies or to local circulations.

During the last week of May, three significant eastward propagating cloud patterns (i.e., 24-26, 26-28 and 28-29 May) were originated in the longitudinal band where the Balkans are located.

Finally, from the 10th of May, non propagating horizontal structures are observed across a broad longitudinal band (~20° to 40° E). These structure are associated with a diurnal maximum of ordinary convection. It’s worth noting the daily convective episodes around 30° E (Anatolia Plateau) during the period 11-20 May.

In general, cloud patterns in June 1997 (Fig. 4-7) present similar features as the May episodes. Propagation of Atlantic systems characterized mainly the first part of June, but became less evident during the second part. Noteworthy, as regards eastward cloud patterns, is that their source regions were west of 5° W in the first ten days of June, and in the band 5° W to 0° from the 15th of June. The important role of mountain range systems (the Alps and the Pyrenees) as source regions for the convective episodes is evident, as noted by Levizzani *et al.* (2006) and Morel and Senesi (2002).

Non propagating horizontal structures were diffused in the eastern part of the domain from 9 to 16 June and from 25 to 30 June, clearly caused by ordinary convection driven by diurnal heating. In June, westward propagating convective episode were still present in the domain, such as on 4-5 and on 28-29, but they were less significant with respect to those in May.

July 1997 (Fig. 4-8) represents the typical midsummer condition. This period was characterised by a widespread less organized convective activity. Non propagating convection can occur almost anywhere, dominated by diurnal forcing. During this period, cloud patterns propagated both eastward (e.g., 14-16 July) and westward (e.g., 20-22 July). The regions where cloud systems were more frequent were the Pyrenees, the Alps and the Balkans.

The conditions of August 1997 (Fig. 4-9) concerning the diffuse presence of non propagating convective activity were similar to those in July and indicate the dominant role of solar heating and orography. During the last week of August, eastward propagating cloud patterns started to be more evident in the westward part of the domain. Also some westward propagating cloud systems were present in the domain, such as from 4 to 8 August. In the eastern part of the domain, the wider and longer lasting systems were localized in the 25° - 35° E longitudinal band (e.g., 10-14 and 24-28).

Figures from 4-10 to 4-13 present the Hovmöller diagrams of the 2005 warm season, a relatively dry year. With respect to the months of May and June 1997, May and June 2005 were characterized by less organized and less wide coherent eastward propagating systems.

From 22 May the most frequent cloud patterns were those associated with non propagating horizontal structures. Thus, the typical summer regime, characterized by ordinary convection associated with thermal forcing, started in advance in the 2005 with respect to the wetter 1997. Diurnally forced cloud patterns of May 2005, such as those from 24 to 31, were originated mainly in the longitudinal band from 20° to 40° E, while in June 2005 the longitudinal band centred around 5°W was an active source region for these kind of events.

In July 2005 cloud patterns appeared less organised and more intermittent, with few longer lasting and more extensive events (e.g., 18-20 and 22-24 July).

The same situation happened during August 2005. The three most significant episodes were originated around 0° and propagated eastward but with low velocity, as can be noted from their slope.

In conclusion, we remark the importance of orography. The regions where cloud episodes were more frequently originated during the warm season, were the mountain range systems that are spread all over the domain. This is true both for wet and dry years.

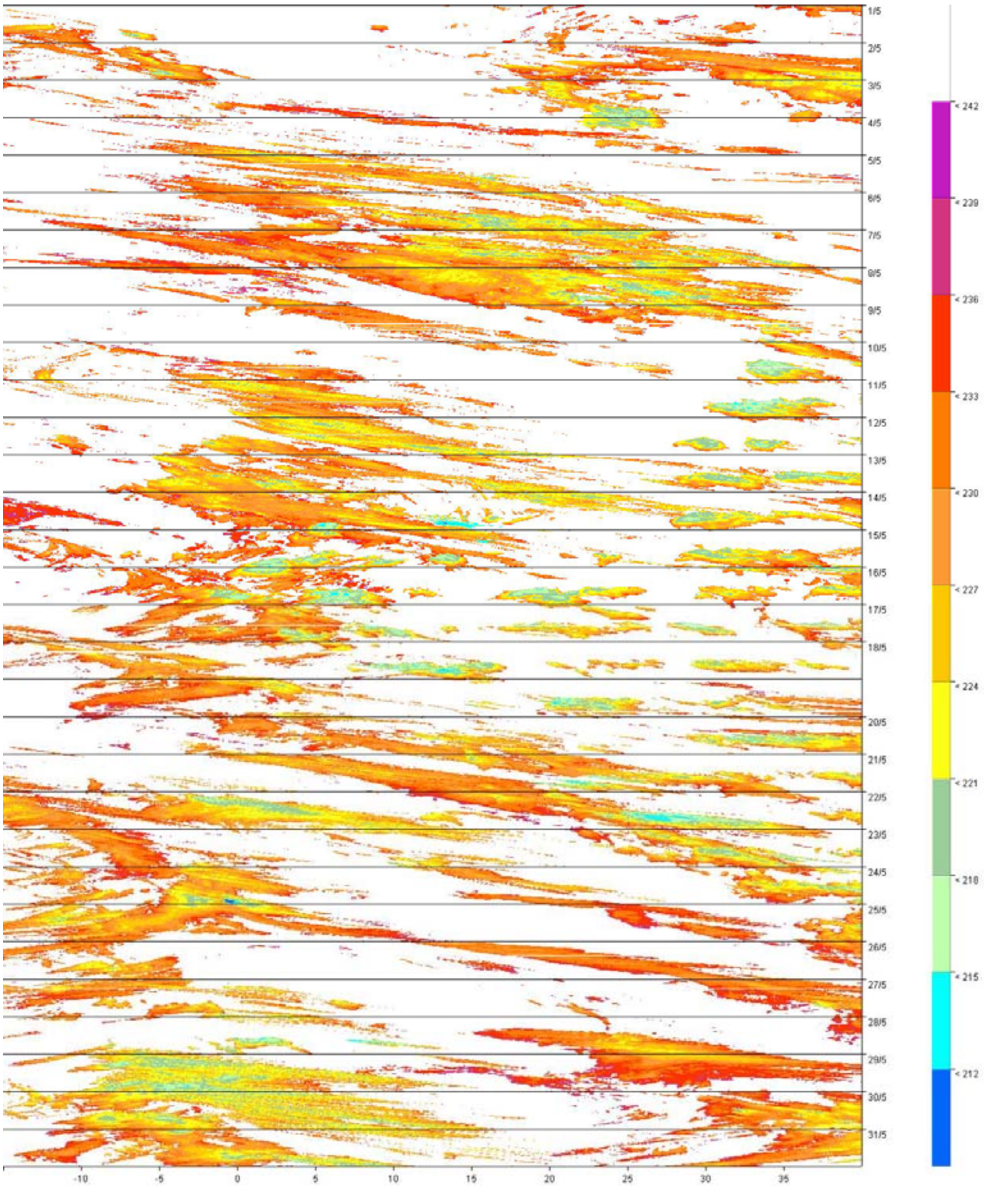

Figure 4-6 *Hovmöller (longitude-time; time in UTC) diagram for May 1997.*

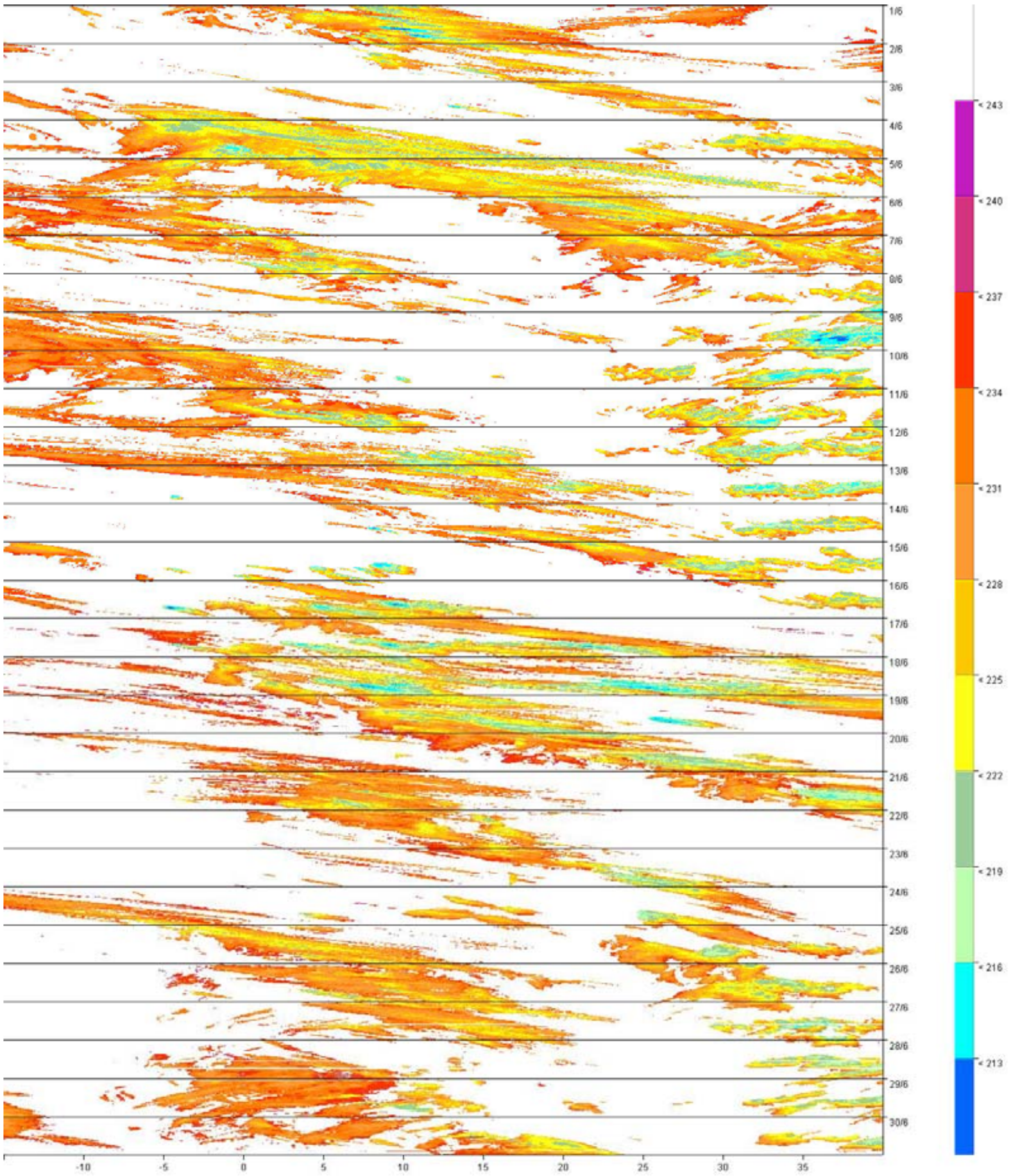

Figure 4-7 *Same as in Fig. 4-6 but for June 1997.*

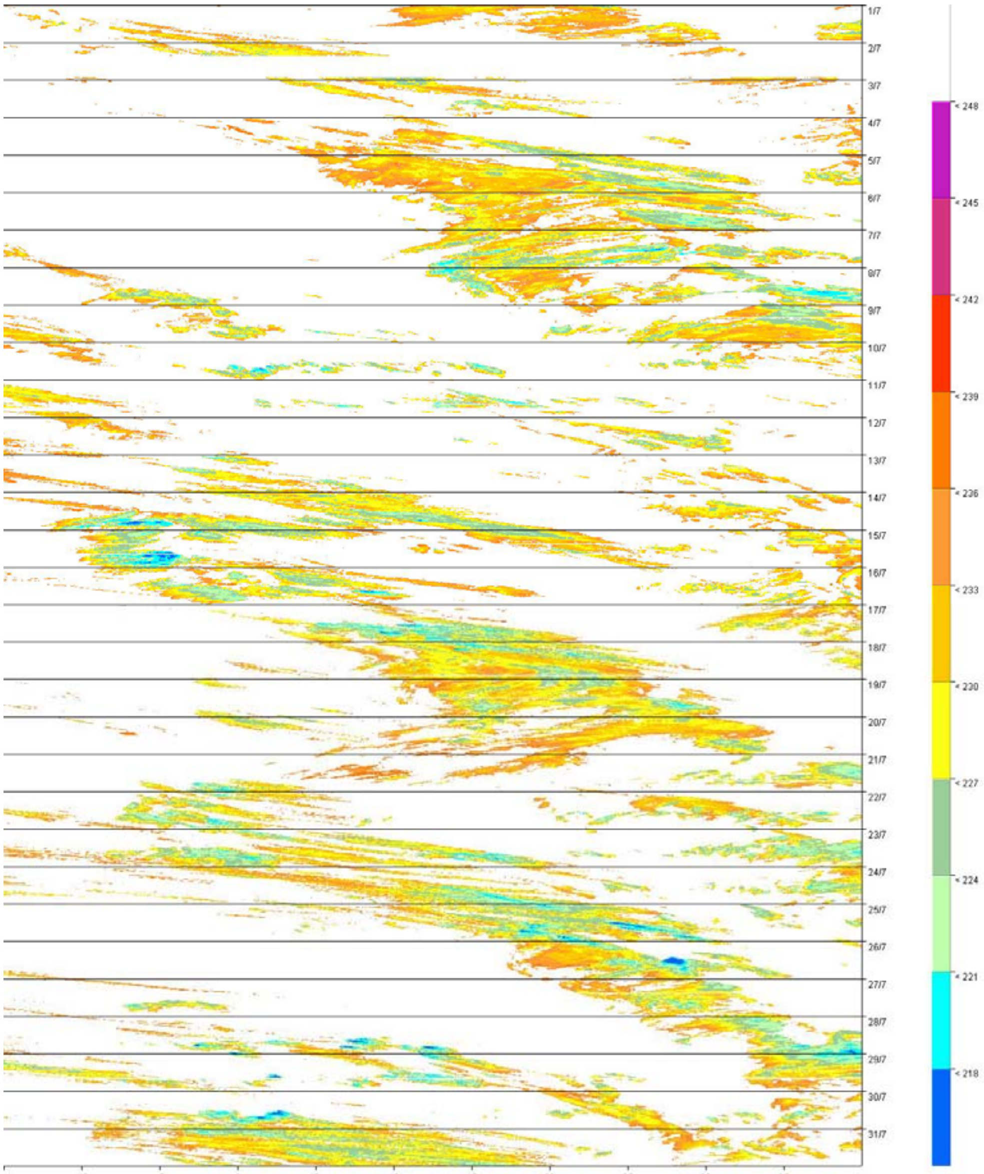

Figure 4-8 *Same as in Fig. 4-6 but for July 1997.*

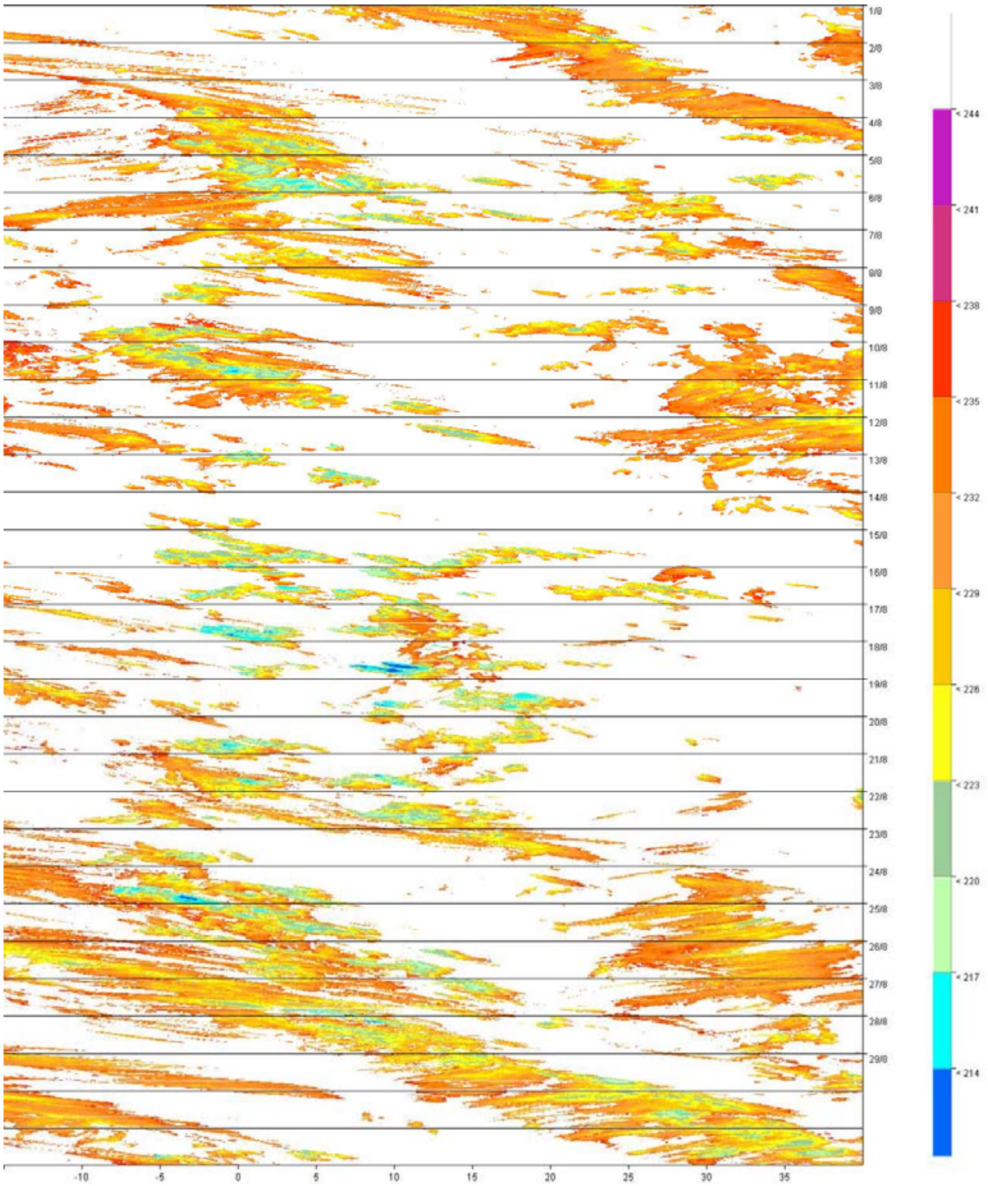

Figure 4-9 *Same as in Fig. 4-6 but for August 1997.*

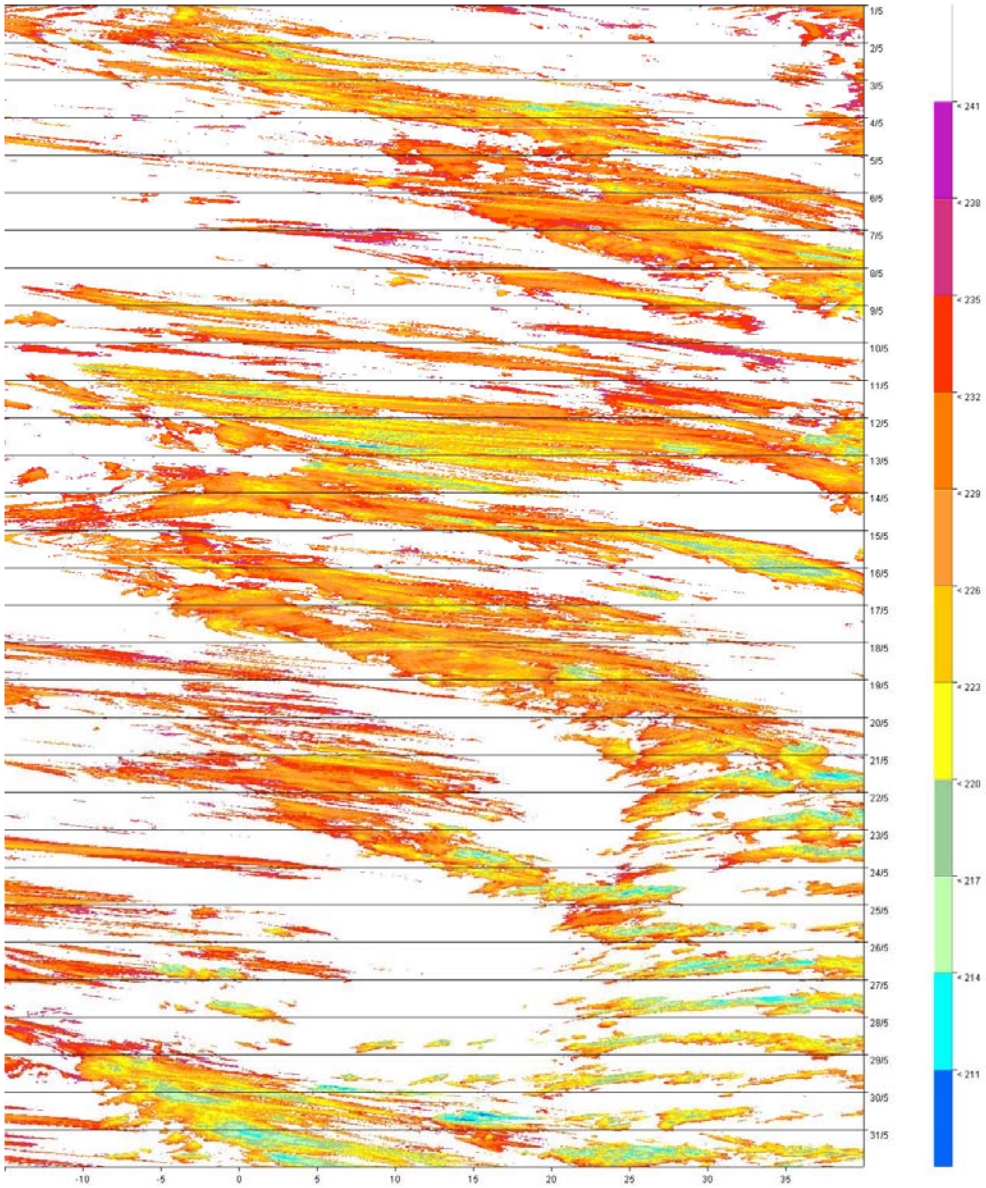

Figure 4-10 *Same as in Fig. 4-6 but for May 2005.*

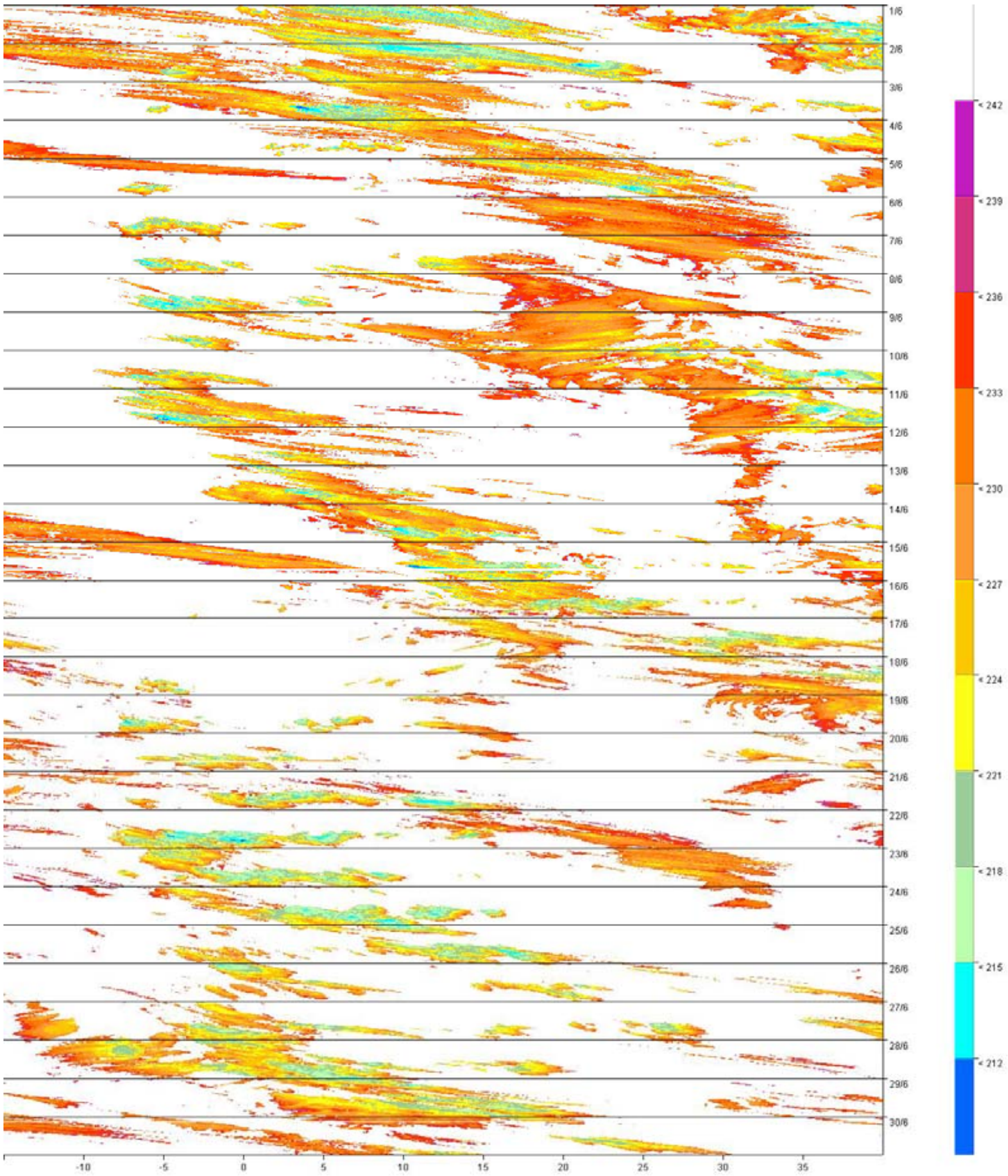

Figure 4-11 *Same as in Fig. 4-6 but for June 2005.*

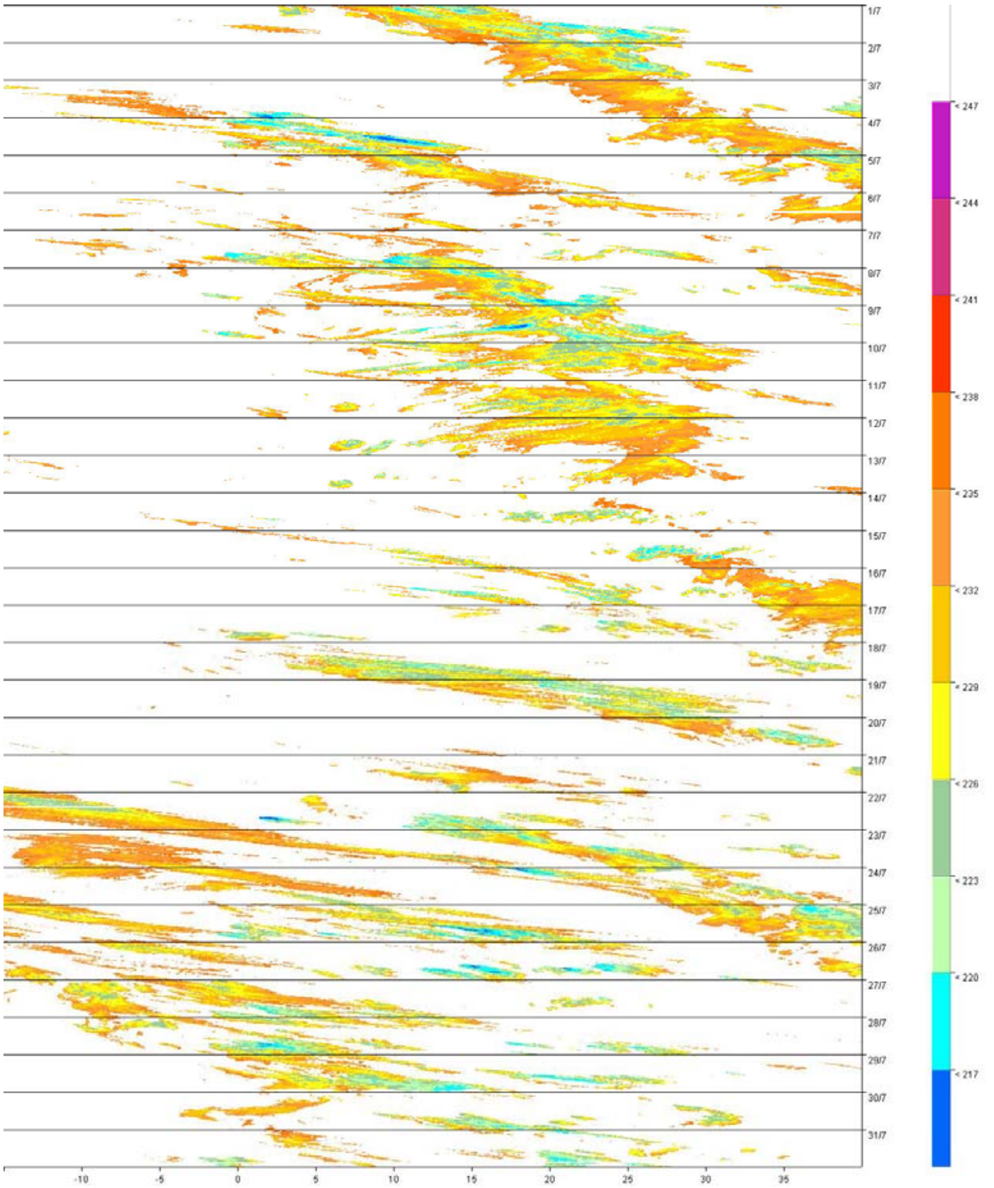

Figure 4-12 *Same as in Fig. 4-6 but for July 2005.*

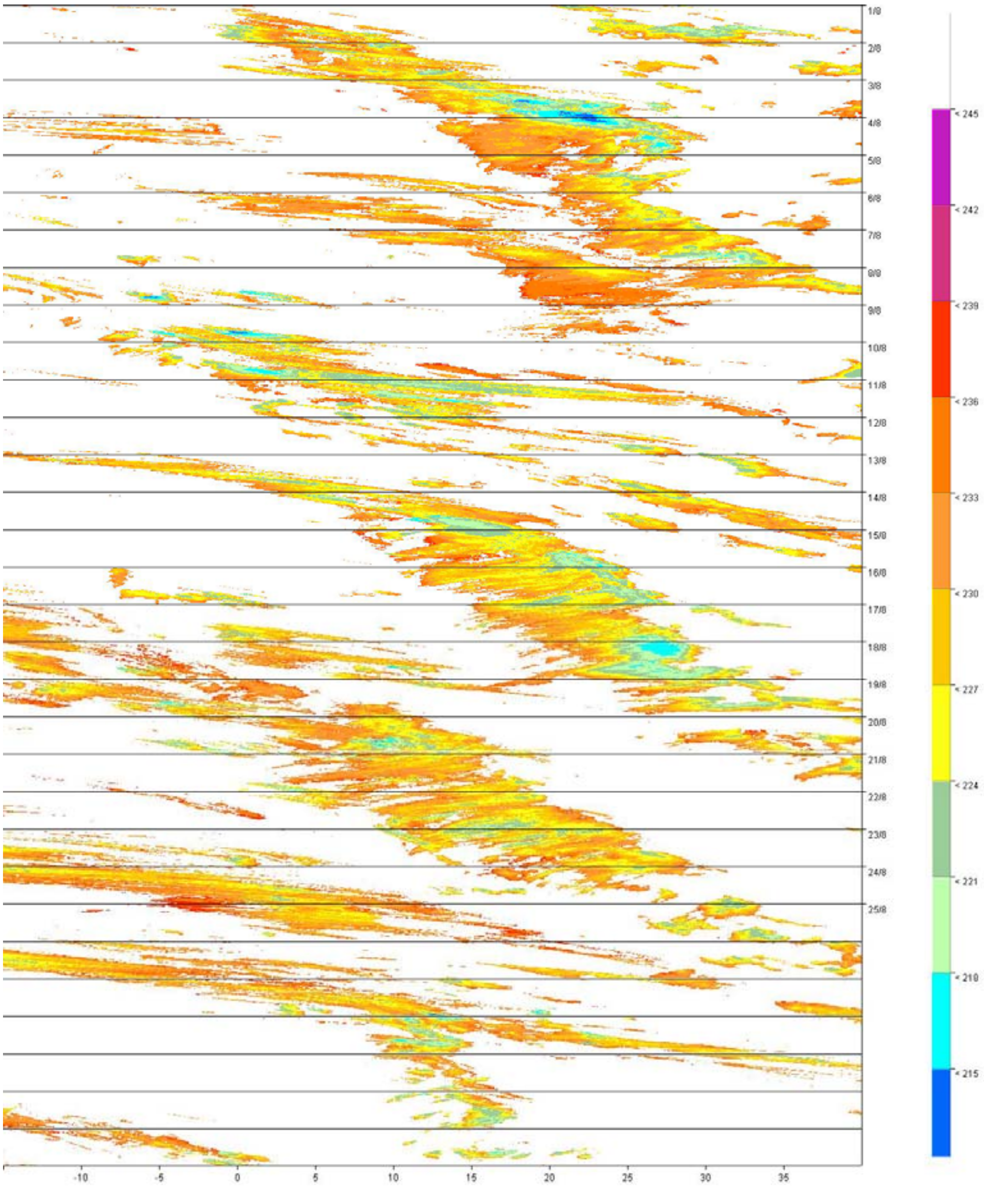

Figure 4-13 *Same as in Fig. 4-6 but for August 2005.*

4.2.3 Analysis of latitude-time diagrams

From our analysis it is evident that cloud patterns propagated not only in the zonal, but also in the meridional direction, even if this kind of propagation is somewhat less marked .

To produce latitude-time plots an analogous method used for the longitude-time diagrams was adopted.

Figure 4-14 and 4-15 present examples of such plots for the years 1997 and 2005.

The plots show that there existed preferred latitudinal bands for cold cloud development and in some periods of the warm season there were some latitudinal bands not interested by convective systems development.

In general, except for May and the first days of June, the southern latitudinal band of the domain, from 30° to 35° N were almost free from significant cloud systems. During July the most active latitudinal band is North of 40°.

The meridional propagation of the clouds systems is slight and directed toward the North during all warm season months, as indicated by the slope of the streaks.

Note that these examples are among those displaying the maximum of meridional propagation; the other months of the ten-year period show even less or no propagation at all thus indicating the zonal character of the motion as is to be expected in the area. The inspection of movie loops for the entire period under scrutiny reveals that the propagation is in fact zonal with the westerlies as the clear driving factor. This in principle explains the motion of the system along latitudinal bands with little or no meridional components.

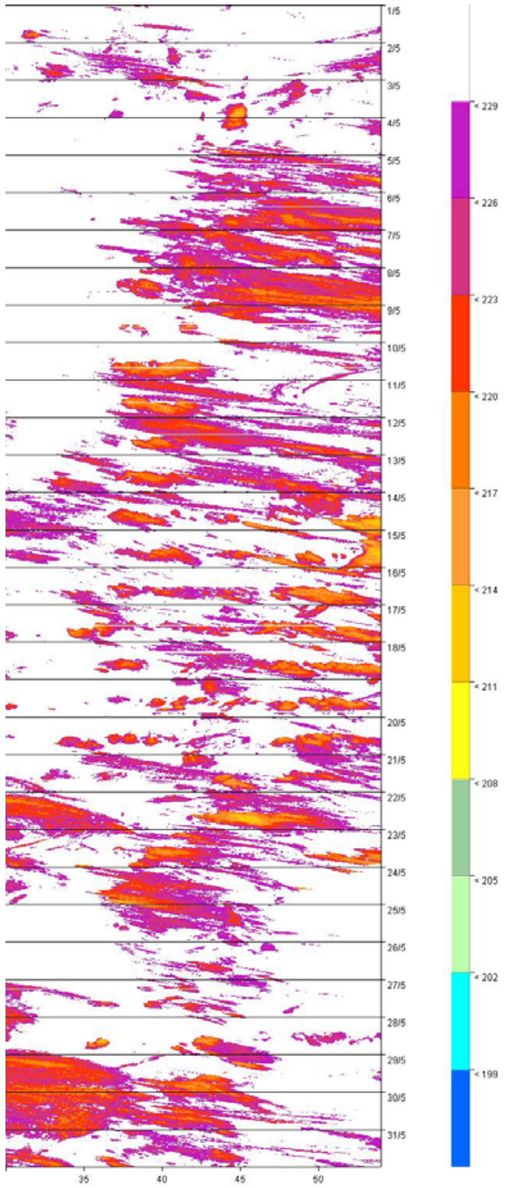

Figure 4-14 *Latitude-time (UTC) Hovmöller diagram for May 1997.*

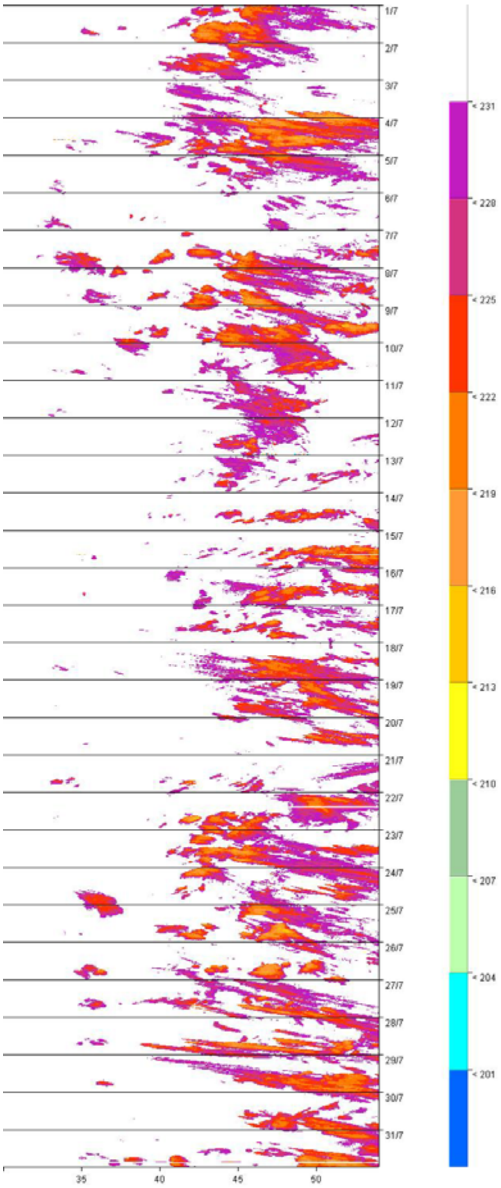

Figure 4-15 *Same as in Fig. 4-14 but for July 2005.*

5. Zonal cold cloud streaks statistics

The coherence and phase speed characteristics of the cold cloud episodes over Europe and the Mediterranean are quantified using the two-dimensional autocorrelation function described in Chapter 2.

The discussion is limited to eastward-moving “events”; an event corresponds to a cold cloud streak as identified by the box autocorrelation function applied to the Hovmöller diagram. A total number of 20152 events occurred during the 1230 warm season days analyzed. Of all events, about 37.2% had a duration of at least 3 h, on average 750 cloud streaks per warm season.

Table 5-1 reports the number of total events, of those lasting more than 3 h, and of those spanning more than 1000 km and lasting more than 20 h. The corresponding median phase speeds are also shown.

To gain others information for helping quantitative precipitation forecasts, in Table 5-2 are presented the mean values of zonal span, duration, and phase speed of episodes lasting more than 3 h and of those spanning more than 1000 km and lasting more than 20 h for each year of the period of analysis. For the 10-years period of study, the mean zonal span, duration and phase speed of convective cloud streaks lasting more than 3 h were 397.5 km, 7.9 h, and 13.4 m s^{-1}, respectively; the same values for events spanning more than 1000 km and lasting more than 20 h were 1621.2 km, 27.6 h, and 16.6 m s^{-1}, respectively.

As it appears from the analysis of all Hovmöller diagrams for the entire period the cold cloud episodes have a continuous character while some of them show an intermittent behaviour, which is most likely attributable to regeneration of convection downstream of the main cloud systems.

Listed in Table 5-3 are the cold cloud streaks zonal span (km) and duration (h) corresponding to several recurrence frequencies for each warm season from 1996 to 2005.

The recurrence frequency is defined as the average time interval for events with at least the specified size, in this case span or duration, to occur again. In order to clarify the concept of recurrence frequency, we report an example. During the 4-month warm season of the 2001, on average 123 events (one per day) exceeded a span of 680.6 km, and similarly, 123 events (perhaps different) lasted for at least 13 h. When the period of recurrence is increased to about one per week, on average 17 streaks start to exceed 1553.9 km and 24 h. Likewise, four events (one per month) reached the size of 2328.8 km, or the duration of 32 h during the same warm season. It’s worth noting that in each season, several events could reach a span greater than 1800 km and last more than 28 h.

We remark that cloud episodes frequently have a scale considerably longer than the typical life span of individual convective systems.

Cold cloud streaks spatial and temporal dimensions emerged from this recurrence frequencies analysis are similar to those obtained by Carbone *et al.* (2002) and Wang *et al.* (2004). The direct comparison of the respective geographical areas of analysis results is reported in Table 5-4. Comparing the mean values of zonal span and duration of the warm season precipitating systems, we can suggest that European systems have shorter dimensions with respect to those in United States domain. In general the values of span obtained in this study are lower than those obtained by Carbone *et al.* (2002), while are more similar to those reported by Wang *et al.* (2004). The same is valid for the durations of the cloud systems.

Note that the differences between our results and those obtained by Carbone *et al.* (2002) may be due to the different dataset adopted for the analysis (radar-data vs satellite-data). A further consideration will be done for cold cloud phase speeds.

The analogy of these findings indicates that the underlining dynamics that governed these episodes on different continents were likely similar.

The phase speeds of cold cloud streaks was then analyzed These properties are explored for the opportunity they offer to better understand the dynamic organization of the summer season cloud systems.

Table 5-5 lists two sets of phase speed estimates, stratified according to recurrence frequency. The top row within each recurrence frequency is the cutoff span/duration ratio computed directly from Table 5-4 values, while the bottom row contains the exceedance speed, defined as the span/duration ratio that is equalled or exceeded with a particular frequency.

Table 5-1 *Number of total events, events lasting ≥ 3 h and events spanning ≥ 1000 km and lasting ≥ 20 h. The corresponding median phase speeds (m* s^{-1}*) are also reported.*

	1996	1997	1998	1999	2000	2001	2002	2003	2004	2005	Mean
Number of events	1910	2225	1940	1972	1962	1957	2016	2047	2173	1950	2015
Number of events ≥ 3h	713	825.0	669.0	743.0	722.0	721.0	764.0	792.0	805.0	744.0	750
Number of events ≥ 1000 km ≥ 20 h	24	33.0	22.0	31.0	22.0	31.0	32.0	20.0	27.0	40.0	28
Median speed all	9.1	9.1	9.1	9.6	9.1	9.1	9.1	9.1	9.1	9.1	9.2
Median speed ≥ 3h	12.5	11.8	12.9	13.3	12.6	12.7	12.0	12.4	12.5	12.6	12.5
Median speed ≥ 1000 km ≥ 20 h	14.3	15.9	17.6	16.2	16.7	16.7	16.6	14.3	17.1	15.4	16.1

Table 5-2 *Mean zonal span (km), duration (h), and phase speed (m s^{-1}) for events lasting ≥ 3 h and events spanning ≥ 1000 km and lasting ≥ 20 h.*

	1996	1997	1998	1999	2000	2001	2002	2003	2004	2005
mean span ≥ 3 h	381.1	386.7	407.3	416.7	392.7	408.8	390.7	368.1	399.8	426.6
mean span ≥1000 km ≥ 20 h	1436.4	1640.0	1885.4	1589.7	1712.9	1571.2	1536.2	1422.2	1856.4	1592.9
mean duration ≥ 3 h	7.8	8.0	7.7	7.8	7.7	7.9	7.9	7.5	8.0	8.4
mean duration ≥ 1000 km ≥ 20 h	26.5	28.7	29.6	25.6	28.5	26.6	25.5	27.8	29.9	27.7
mean speed ≥ 3 h	13.4	12.7	14.0	14.3	13.4	13.6	13.2	13.3	13.2	13.4
mean speed ≥ 1000 km ≥ 20 h	15.4	16.1	18.0	17.5	17.2	16.6	16.9	14.4	17.4	16.1

Table 5-3 *Zonal span (km), and duration (h) for different recurrence frequency of cold cloud systems lasting ≥3 h in each warm season from 1996-2005.*

Recurrence frequency	1996	1997	1998	1999	2000	2001	2002	2003	2004	2005	Mean
	Zonal span (km) *Duration (h)*										
1 per day	586.3	647.8	602.7	664.2	606.8	680.6	676.5	602.7	664.2	729.8	646.2
	11.5	13.0	11.0	12.0	11.5	12.0	13.0	11.5	13.0	12.5	12.1
1 per 2 days	815.9	975.8	938.9	1004.5	861.0	1000.4	959.4	873.3	922.5	1029.1	938.1
	16.0	17.5	14.5	16.5	15.5	16.5	16.5	15.0	16.0	18.0	16.2
2 per week	1152.1	1316.1	1168.5	1283.3	1225.9	1295.6	1197.2	1123.4	1234.1	1320.2	1231.6
	20.0	20.5	17.0	19.5	18.5	19.5	20.5	18.0	20.0	22.5	19.6
1 per week	1373.5	1541.6	1586.7	1615.4	1574.4	1578.5	1553.9	1373.5	1836.8	1730.2	1576.5
	24.5	26.0	26.0	23.5	22.0	25.0	24.0	23.5	28.0	28.0	25.1
2 per month	1660.5	1799.9	2062.3	2050.0	1927.0	1832.7	1795.8	1693.3	2107.4	1968.0	1889.7
	28.5	32.5	32.0	29.0	30.0	28.0	30.0	28.0	34.5	33.0	30.6
1 per month	1877.8	2390.3	2308.3	2173.0	2164.8	2173.0	2328.0	1836.8	2337.0	2455.9	2204.5
	32.0	41.0	37.0	30.5	33.5	32.0	32.0	32.0	37.0	36.5	34.4

Table 5-4 *Mean values of cloud streaks zonal span (km) and duration (h) at different recurrence frequency thresholds for events identified in May-August 1996-2005. The last two columns give corresponding values obtained by Carbone et al. (2002) for the continental United States, and by Wang et al. (2004) for East Asia.*

Recurrence frequency	Mean	Carbone *et al.* (2002)	Wang *et al.* (2004)
	Zonal span (km) *Duration (h)*		
1 per day	646.2	838.0	620.0
	12.1	18.5	11.6
1 per 2 days	938.1	1250.0	1008.8
	16.2	24.5	17.5
2 per week	1231.6	1588.0	1327.7
	19.6	30.5	22.0
1 per week	1576.5	2000.0	1706.8
	25.1	40.3	26.6
2 per month	1889.7	2325.0	2178.8
	30.6	49.0	34.3
1 per month	2204.6	2500.0	2664.0
	34.4	55.5	39.1

Table 5-5 *Values in m s^{-1} of cutoff span/duration ratio ,and exceedance speed for different recurrence frequency of cold cloud systems lasting ≥ 3 h in each warm season from 1996-2005.*

Recurrence speeds	1996	1997	1998	1999	2000	2001	2002	2003	2004	2005	Mean
(number of samples)	(1910)	(2225)	(1940)	(1972)	(1962)	(1957)	(2016)	(2047)	(2173)	(1950)	(2015)
	Span/duration (ms^{-1}) *Exceedance speed (ms^{-1})*										
1 per day	14.2	13.8	15.2	15.4	14.7	15.8	14.5	14.6	14.2	16.2	14.8
	18.8	18.5	19.7	20.0	18.9	19.6	19.2	19.0	18.9	18.8	19.1
1 per 2 days	14.29	15.5	18.0	16.9	15.4	16.8	16.2	16.2	16.0	15.9	16.1
	22.0	21.80	23.8	23.9	23.0	23.0	22.8	22.4	22.8	21.9	22.7
2 per week	16.0	17.8	19.1	18.3	18.4	18.4	16.2	17.3	17.1	16.3	17.5
	24.9	23.6	26.0	27.3	26.1	25.4	25.7	24.5	24.9	24.8	25.3
1 per week	15.6	16.5	17.1	19.1	19.9	17.5	18.0	16.2	18.2	17.2	17.5
	28.3	27.7	30.4	31.0	28.9	28.8	29.1	28.3	27.3	27.2	28.7
2 per month	16.2	15.4	17.9	19.6	17.8	18.2	16.6	16.8	17.0	16.6	17.2
	32.4	29.4	34.5	37.5	30.4	31.9	32.9	31.7	28.9	29.4	31.9
1 per month	16.3	16.2	17.3	19.8	17.9	18.9	20.2	15.9	17.5	18.7	17.9
	34.5	30.6	36.4	40.1	34.0	32.8	34.0	36.0	31.7	32.3	34.3

Table 5-6 *Mean values of cloud streaks zonal phase speeds at different recurrence frequency thresholds for events identified in May-August 1996-2005. The last two columns give corresponding values obtained by Carbone et al. (2002) for the continental United States, and by Wang et al. (2004) for East Asia. Values in top rows are computed directly from span and duration, and those in bottom rows are "exceedance phase speed", defined as the threshold exceeded only by the fastest streaks at specified recurrence frequency.*

Recurrence frequency	Mean *Span/duration (m s^{-1})* *Exceedance speed (m s^{-1})*	Carbone *et al.* (2002)	Wang *et al.* (2004)
1 per day	14.8	12.6	14.9
	19.1	23.9	17.3
1 per 2 days	16.1	14.3	16.0
	22.7	26.6	21.0
2 per week	17.5	14.5	16.8
	25.3	28.7	24.4
1 per week	17.5	13.8	17.8
	28.7	30.8	28.2
2 per month	17.2	13.3	17.7
	31.9	33.8	33.3
1 per month	17.9	13.3	19.0
	34.3	37.7	37.9

Table 5-5 tells us that the events of each recurrence frequency category had very similar values of cutoff span/duration, all between about 14 m s^{-1} and 20 m s^{-1}, while the respective exceedance phase speeds were significantly larger and spanned over a greater range of values, from 18.5 m s^{-1} to 40 m s^{-1}.

Table 5-6 shows the respective phase speeds mean values and compares them to the findings valid for United States and East Asia domains. We note that the cutoff span/duration values and the respective exceedance phase speeds of the European clouds systems were in general higher than those of the United States systems, and of the same order of magnitude than those of the East Asia systems.

It must be considered that a comparison between satellite-derived phase speed with the radar-derived one cannot be done without considering the different observation instruments, which are based on different observing principles and, most important of all, they see different parts of the clouds, the T_b at cloud top from satellite and the precipitation from radar. Tuttle et al. (2008) have found that the mean satellite-radar difference in the zonal propagation speed at the 241 K threshold chosen for this study ranges between 3.7 and 4 m s^{-1}. If this difference is applied to the reported 16.1 m s^{-1} median phase speed, the resulting speed attains a value comparable with the radar-derived one over North America.

Figure 5-1 illustrates the scatter plot of zonal span versus duration of all cloud streaks during the period May to August 1996-2005. The distribution of the scatter plot is quite similar to those of Carbone *et al.* (2002) and Wang *et al.* (2004), and indicates that the vast majority of cold cloud systems had zonal propagation speed within the range between 7 and 30 m s^{-1}. The median zonal phase speed for events with span ≥ 1000 km and duration ≥ 20 h was 16.1 m s^{-1}, represented by the solid line.

The cumulative probability histograms of cold cloud streak zonal span and duration are shown in Fig. 5-2 for the 10 years analysed, May through August. Both histograms exhibit a continuum of events with decreasing frequency.

The distribution of large cloud streaks during the overall study period is shown in Fig. 5-3. Large cloud streaks are divided into three categories: streaks larger in span and longer in duration than 500 km and 10 h, 1000 km and 17 h, and 1500 km and 25 h, respectively. The longitudinal domain was divided into 2.5° bands and the longitude corresponding to the starting point of each streak is considered while counting the number of streaks of each category. Figure 5-3 shows that the peaks of the number of larger events are located in the Atlantic Ocean and around the longitudinal bands corresponding to mountain ranges as the Pyrenees, the Alps and the Balkans.

To further identify key statistical properties of the streaks that could give useful information for the improvement of the ability to predict them, the total number of streaks larger and longer than a particular span or duration for each warm season was analyzed.

With reference to the span, the categories of analyzed streaks were the total number of streaks larger than 500 km, 1000 km, and 1500 km; while as regards to the duration the values of 10 h, 17 h, and 25 h were used as limits for the categories. In Fig. 5-4 and 5-5 are reported the histograms stemming from this analysis. Note that, apart from some seasons, the total number of streaks for each category does not differ too much from year to year, but it seems to maintain a narrow range of values for both span and duration.

Finally, Fig. 5-6 presents the duration and span exceedance frequency of the convective cloud streaks, together with the recurrence interval in days.

Note that the distribution of exceedance frequency is nearly exponential, as it is represented by a straight line on the log-linear plots. Only the first classes of both duration and span distributions deviate slightly from this trend.

This trend is expected in the case that the location (in time and space) of the convection are reasonably random, let alone their initiating condition connected with the general circulation patterns.

Distributions like those presented in Fig. 5-6, which evaluate the statistical properties of cold cloud episodes, can serve as benchmarks for forecast models of quantitative precipitations and are helpful for answering climatological questions, such as, what is the probability of occurrence of convective episodes of a particular span or duration.

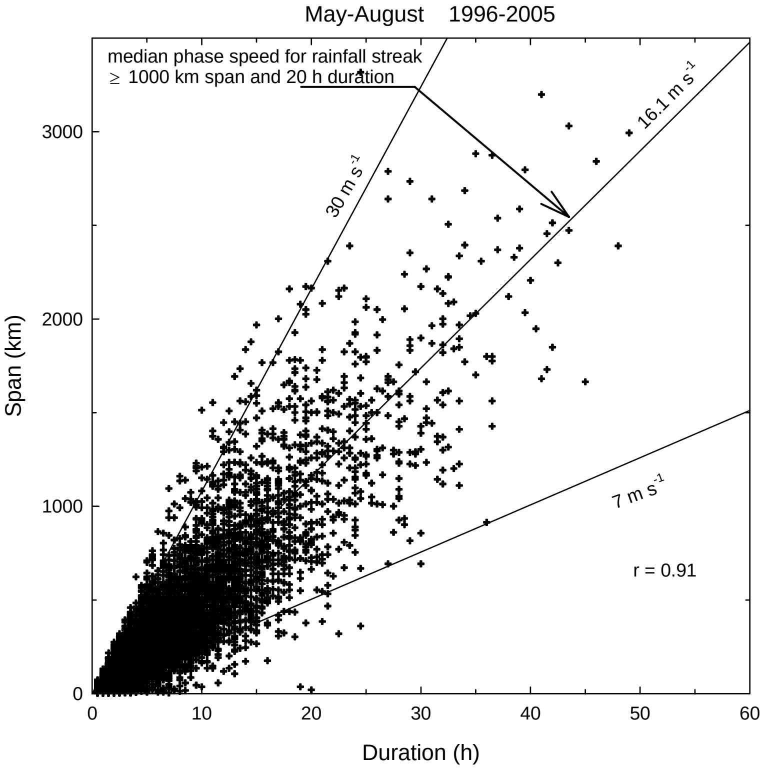

Figure 5-1 *Zonal span-duration of all cold cloud systems streaks May-August 1996-2005. The external lines represent the phase speeds of 7 and 30 m s^{-1}, respectively, which encompass most streaks extending more than 1000 km and lasting more than 20 h. The central line refers to the median phase speed for such systems.*

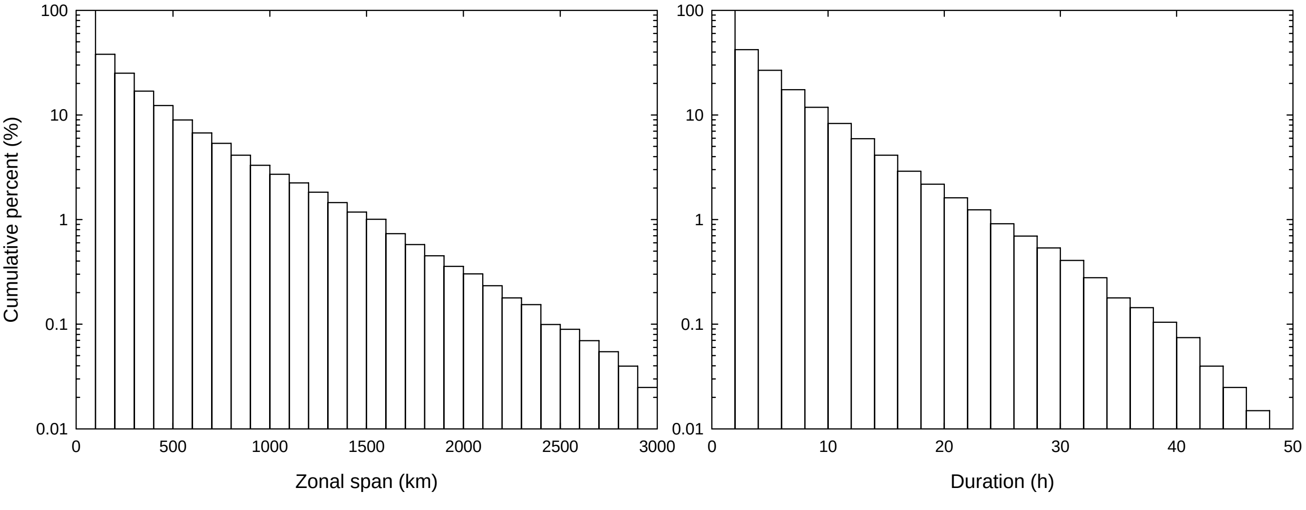

Figure 5-2 *Cumulative probability histograms for zonal span and duration for cold cloud streaks. The period of record is May through August for the years 1996 through 2005.*

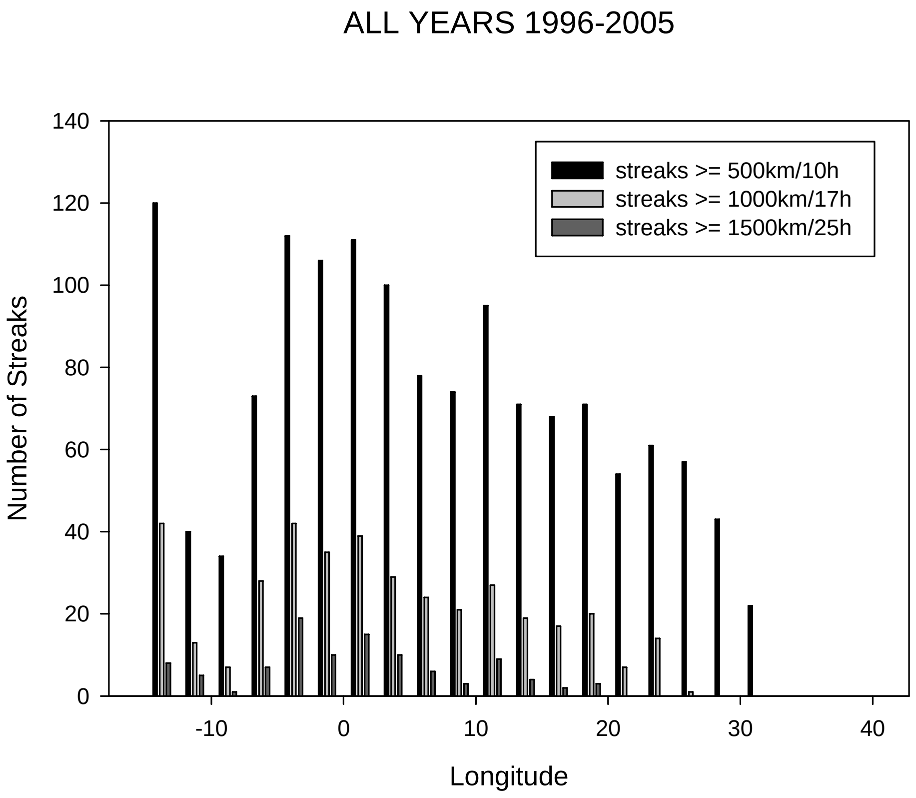

Figure 5-3 *Number of streaks large in span and longer in duration than 500 km and 10 h, 1000 km and 17 h, and 1500 km and 25 h centred inside each 2.5° longitude band. Number of cases in each category is indicated.*

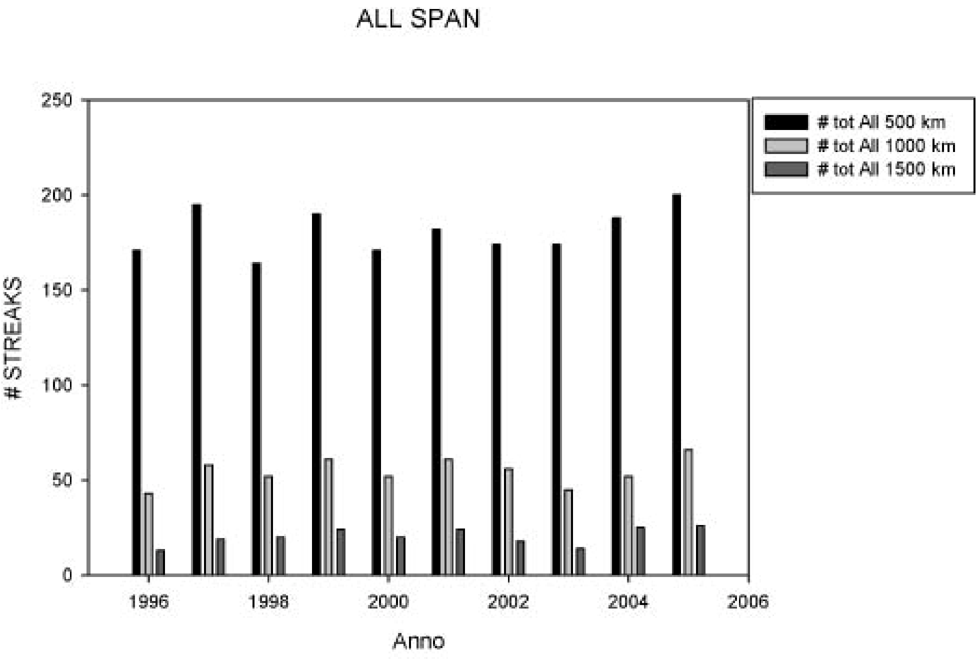

Figure 5-4 *Number of streaks larger than 500 km, 100 km, and 1500 km. Number of cases in each category for each year is indicated.*

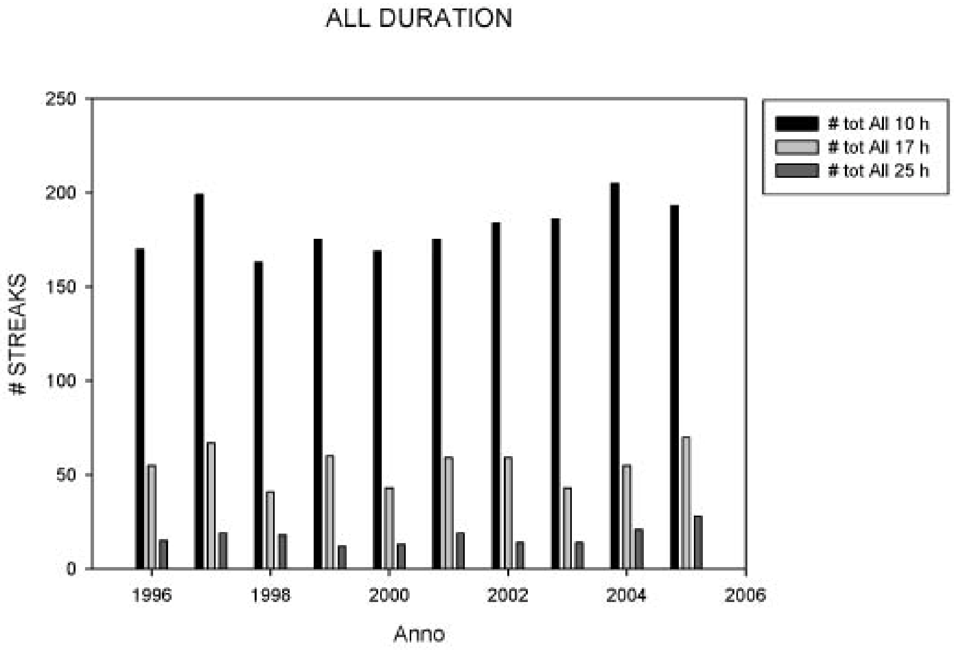

Figure 5-5 *Number of streaks longer in duration than 10 h, 17 h, and 25 h. Number of cases in each category for each year is indicated.*

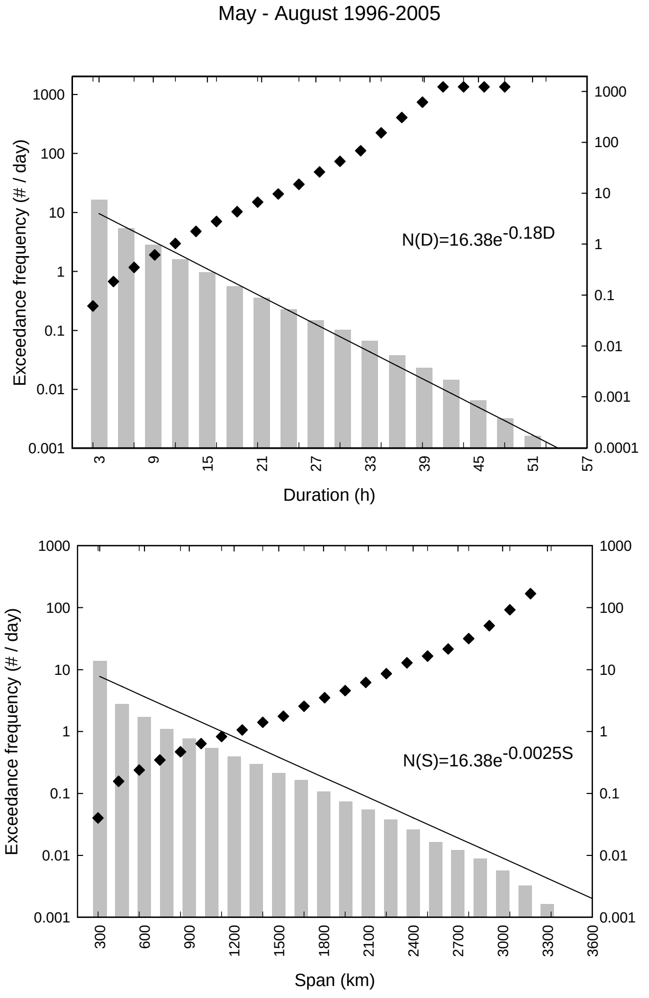

Figure 5-6 *Exceedence frequency (vertical bas, number per day), and recurrence interval (black dots), for duration (top) and span (bottom) of cold cloud episodes during May-August, 1996-2005.*

5.1 Intraseasonal variability of cloud streaks

In order to evaluate the aspects of intraseasonal variability of convective activity over Europe and the Mediterranean, a statistical analysis of cloud streaks developed during the 10 months of May, June, July and August, respectively, was conducted. Table 5-7 reports the number of events lasting more than 3 h and of those spanning more than 1000 km and lasting more than 20 h; the corresponding median and mean spans, durations and phase speeds are also shown.

Table 5-7 *Number of events, median and mean zonal span (km), duration (h), and phase speed (m s^{-1}) of cloud streaks lasting ≥ 3 h, and those spanning ≥ 1000 km and lasting ≥ 20 h in each month from may to August 1996-2005.*

	1996	1997	1998	1999
Number of events ≥ 3 h	2174	1843	1708	1773
Number of events ≥1000 km ≥ 20 h	77	84	59	62
Median span ≥ 3 h	282.9	278.8	262.4	266.5
Mean span ≥ 3 h	409.1	410.1	386.6	380.7
Median span ≥1000 km ≥ 20 h	1562.1	1553.9	1443.2	1371.5
Mean span ≥1000 km ≥ 20 h	1657.3	1676.5	1645.1	1478.9
Median duration ≥ 3 h	6.0	6.0	5.8	6.0
Mean duration ≥ 3 h	7.9	8.1	7.7	7.8
Median duration ≥1000 km ≥ 20 h	25.0	25.0	26.0	27.3
Mean duration ≥1000 km ≥ 20 h	27.1	27.1	29.1	27.3
Median speed ≥ 3 h	12.8	12.6	12.2	12.3
Mean speed ≥ 3 h	13.8	13.4	13.2	13.2
Median speed ≥1000 km ≥ 20 h	16.8	16.9	15.5	14.3
Mean speed ≥1000 km ≥ 20 h	17.4	17.3	15.4	14.0

The number of eastward-moving events from May to August for both categories of events was roughly comparable (Table 5-7, first and second rows), with a greater number of episodes happened during the first two months of the warm season. Events lasting more than 3 h had an average zonal span larger in May and June, and it decreased in August. Events spanning more than 1000 km and lasting more than 20 h showed an August minimum of the mean span more evident compared the other months values. This can be explained considering a more dominant role of thermal effects in driving July and August convection with respect to May and June.

Data concerning duration and phase speed of both categories of events are in general of the same order of magnitude during the four months (Table 5-7, rows 8th, 10th, 112th and 14th), with averaged phase speeds that decreased monotonically from May to August.

Monthly scatter plots of zonal span and duration are presented from Fig. 4-7 to 4-10. Each monthly scatter plot shows that the vast majority of cold cloud events had zonal propagation speed enclosed between 7 to 30 m s^{-1}, as emerged also from the scatter plot containing all the data (Fig. 5-1). The scatter plot of May 1996-2005 presents a more disperse distribution of streaks, while the other monthly scatter plots present a lower number of events falling out of the lines that indicate the two limit propagation speeds. Finally, note that events spanning more than 1000 km, and lasting more than 20 h reached their lowest median phase speed in May, i.e. 14.3 m s^{-1}.

Aspects of intraseasonal variability of convective activity can be further examined presenting threshold values of zonal span, duration, and phase speeds at various recurrence frequencies.

In Tables 5-8 and 5-9 are reported the mean values of the monthly values of the streaks characteristics for each recurrence frequency. For example, during the 31 day period of record of each month of May considered in this analysis, the mean zonal span value of 737.6 km was equalled or exceeded about 31 times, or once per day.

Considering the threshold values of zonal span for each period of recurrence, it’s worth noting that they are lower in July and August with respect to May and June. In particular, taking into account the overall warm season, events that happened once per month were on average narrower in August. When the period of recurrence was increased to about once per week, streaks started to reach a span of 1500 km and a duration of 25 h.

The mean values of phase speed, obtained as span duration ratios, spanned from 14 m s^{-1} to 20 m s^{-1} during all warm season months and at each recurrence frequency. In general, the mean speed values of May were higher with respect to the other months. The same is valid for exceedance speed cutoff values, i.e. streaks happened during May were on average the fastest of the warm season.

Table 5-8 *Zonal span (km), and duration (h) for different recurrence frequency of cold cloud systems lasting ≥ 3 h in each month from May to August 1996-2005.*

Recurrence frequency	May	June	July	August
		Zonal span (km)		
		Duration (h)		
1 per day	737.6	685.9	588.8	615.0
	13.1	12.7	11.4	11.9
1 per 2 days	1110.7	1000.4	928.2	894.2
	17.3	17.0	15.4	16.0
2 per week	1394.8	1348.9	1192.7	1136.9
	21.3	21.8	20.2	20.5
1 per week	1691.3	1662.6	1555.5	1471.1
	25.8	27.5	26.2	25.6
2 per month	2054.1	2039.8	1858.5	1746.0
	29.5	30.4	32.5	29.4
1 per month	2424.3	2492.8	2393.2	1982.8
	38.4	37.9	39.8	34.5

Table 5-9 *Values in m s^{-1}of cut off span/duration ratio, and exceedance speed for different recurrence frequency of cold cloud systems lasting ≥ 3 h in each month from May to August 1996-2005.*

Recurrence frequency	May	June	July	August
Span/duration (ms^{-1})				
Exceedance speed (ms^{-1})				
1 per day	15.7	15.0	14.4	14.4
	20.8	19.9	18.3	18.6
1 per 2 days	17.8	16.3	16.8	15.6
	24.5	22.7	21.9	22.3
2 per week	18.3	17.1	16.4	15.5
	27.5	25.7	24.4	25.0
1 per week	18.5	17.0	16.4	16.2
	31.4	28.9	28.0	27.3
2 per month	19.7	18.9	16.0	16.8
	34.0	32.1	31.4	29.9
1 per month	17.8	18.8	16.7	16.0
	36.9	34.1	34.6	32.1

In Fig. 5-11 to 5-14 the seasonal distributions of large clouds streaks following the same streak classification of Fig. 5-3 are shown. Larger events are generated almost uniformly along the longitudinal domain during May 1996-2005. During the others 10 month periods, longitudinal bands associated with mountain ranges emerged as streaks source regions. It's interesting to note the two net peaks of the number of streaks larger than 500 km and longer than 10 h, located around 15° W and 0°.

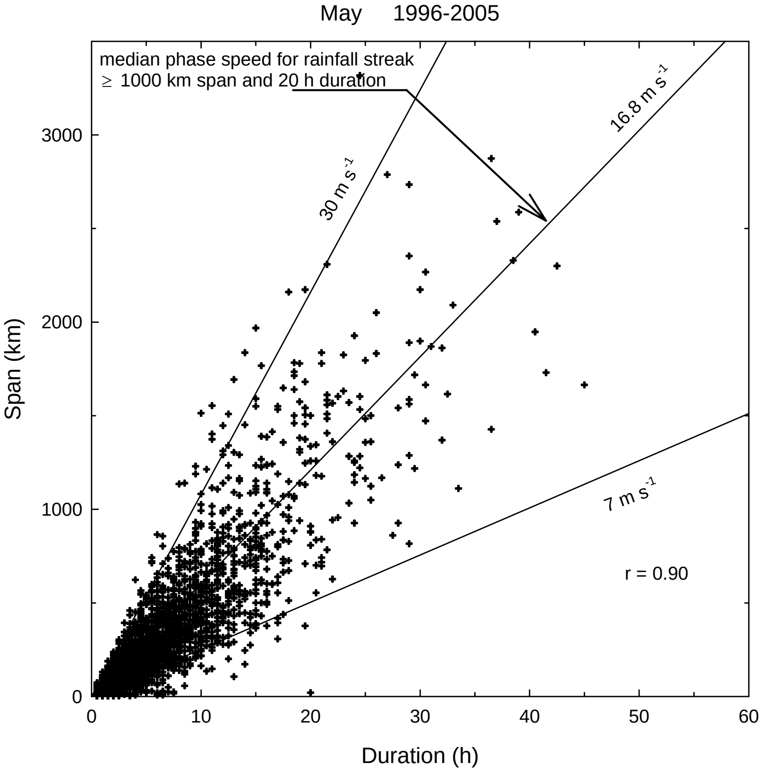

Figure 5-7 *Zonal span-duration of all cold cloud systems streaks May 1996-2005. The external lines represent the phase speeds of 7 and 30 m s^{-1}, respectively, which encompass most streaks extending more than 1000 km and lasting more than 20 h. The central line refers to the median phase speed for such systems.*

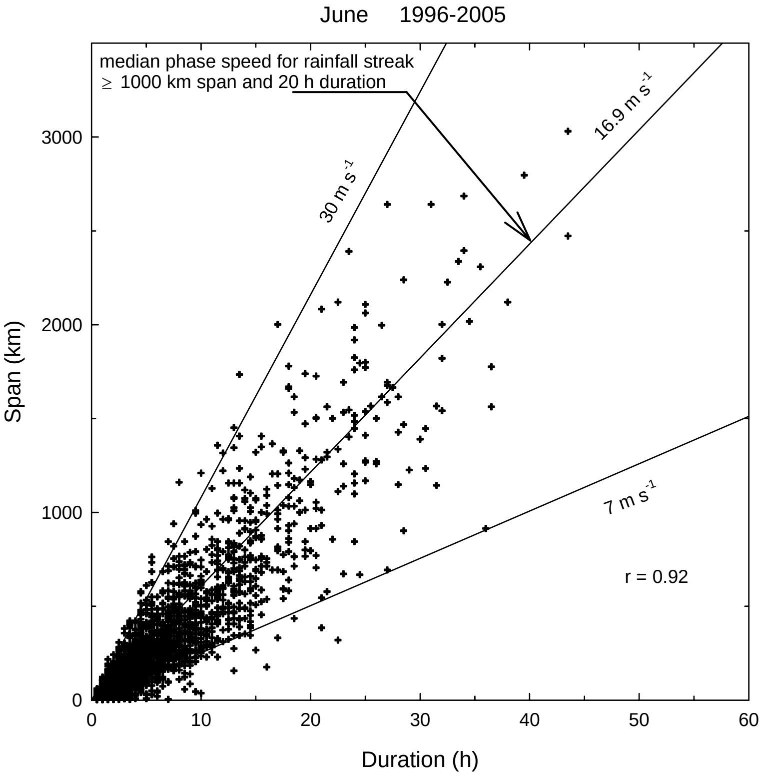

Figure 5-8 *Zonal span-duration of all cold cloud systems streaks June 1996-2005. The external lines represent the phase speeds of 7 and 30 m s-1, respectively, which encompass most streaks extending more than 1000 km and lasting more than 20 h. The central line refers to the median phase speed for such systems.*

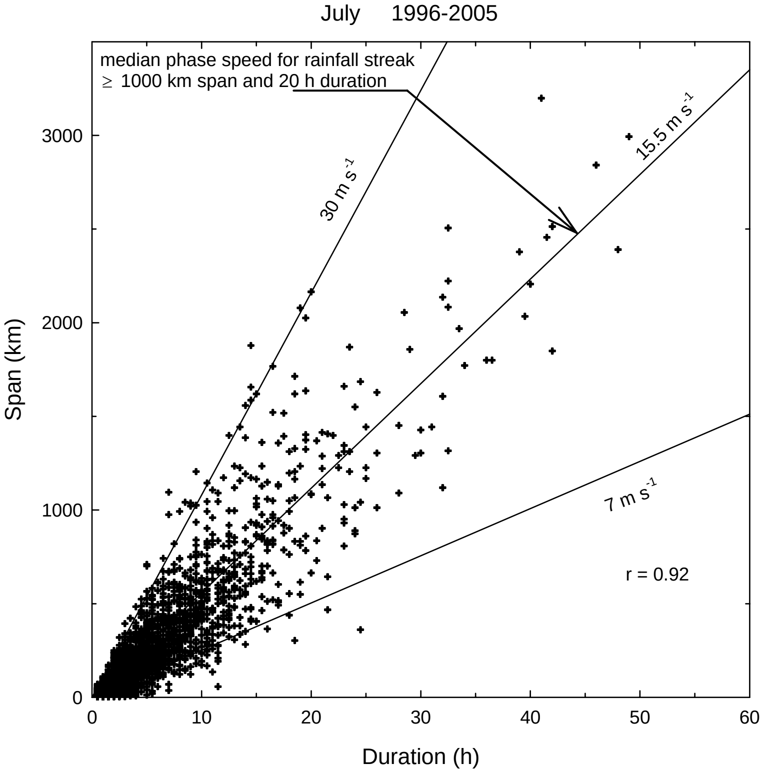

Figure 5-9 *Zonal span-duration of all cold cloud systems streaks July 1996-2005. The external lines represent the phase speeds of 7 and 30 m s-1, respectively, which encompass most streaks extending more than 1000 km and lasting more than 20 h. The central line refers to the median phase speed for such systems.*

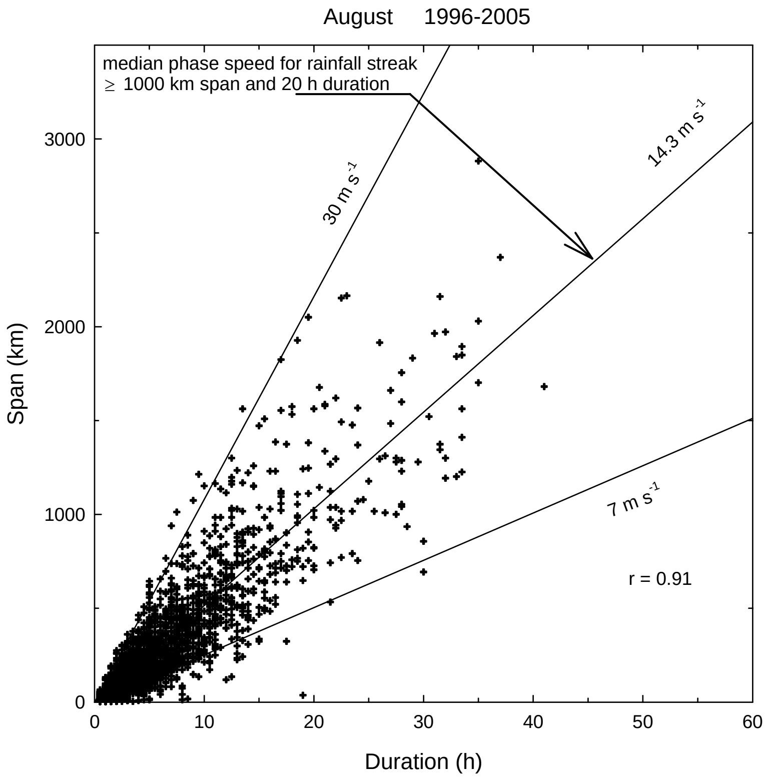

Figure 5-10 *Zonal span-duration of all cold cloud systems streaks August 1996-2005. The external lines represent the phase speeds of 7 and 30 m s-1, respectively, which encompass most streaks extending more than 1000 km and lasting more than 20 h. The central line refers to the median phase speed for such systems.*

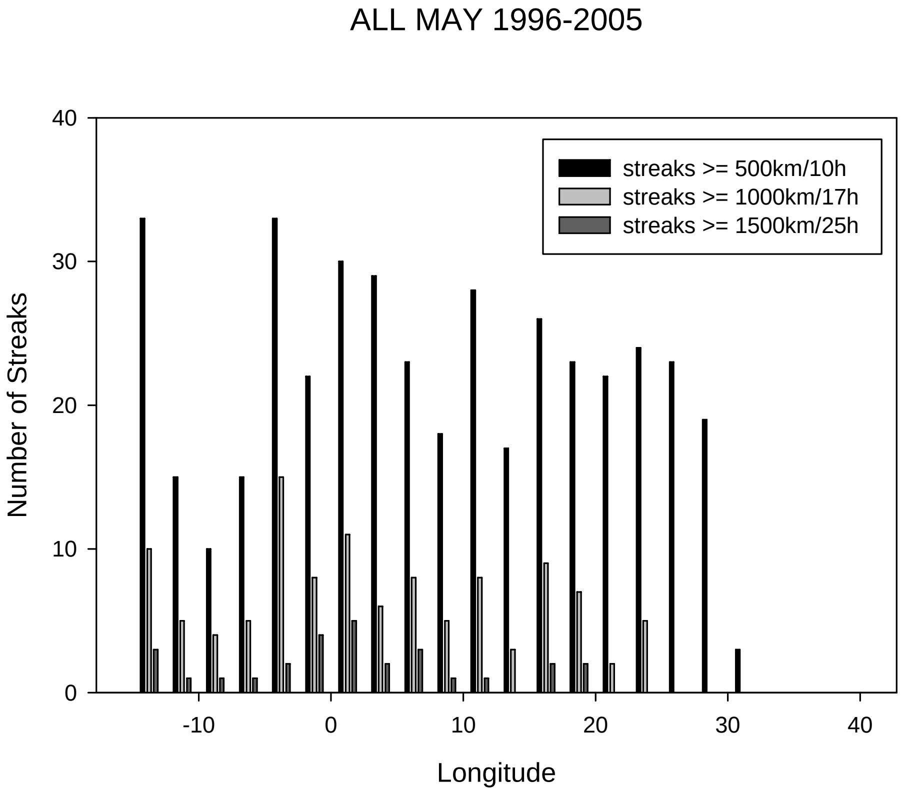

Figure 5-11 *Number of streaks larger in span and longer in duration than 500 km and 10 h, 1000 km and 17 h, and 1500 km and 25 h centred inside each 2.5° longitude band. The number of cases in each category during May 1996-2005 is indicated.*

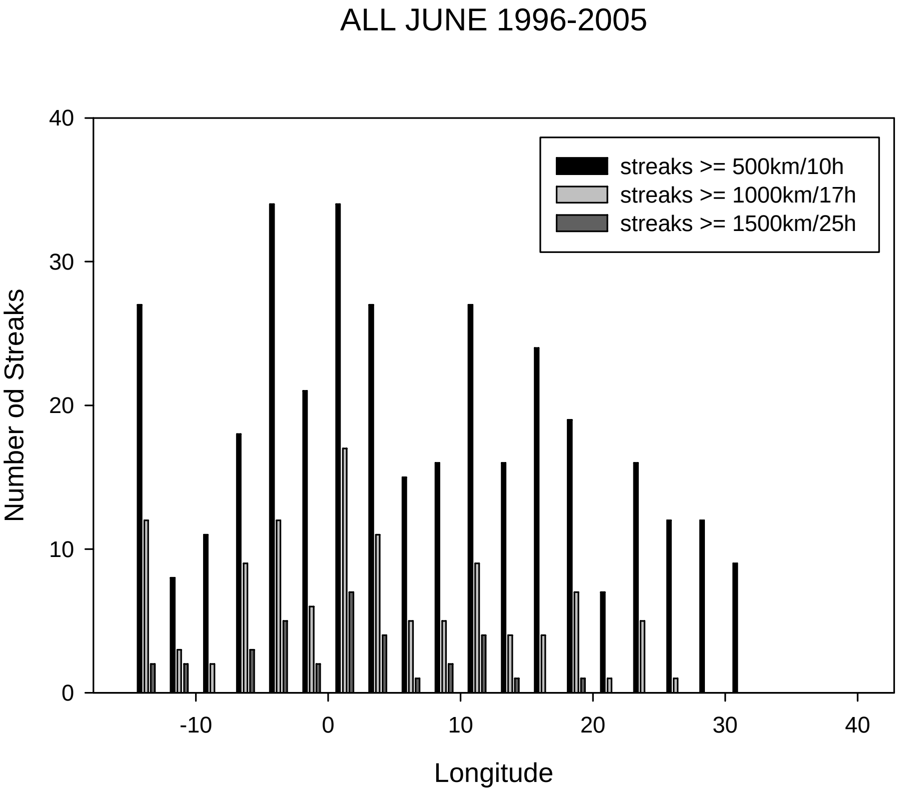

Figure 5-12 *Number of streaks larger in span and longer in duration than 500 km and 10 h, 1000 km and 17 h, and 1500 km and 25 h centred inside each 2.5° longitude band. The number of cases in each category during June 1996-2005 is indicated.*

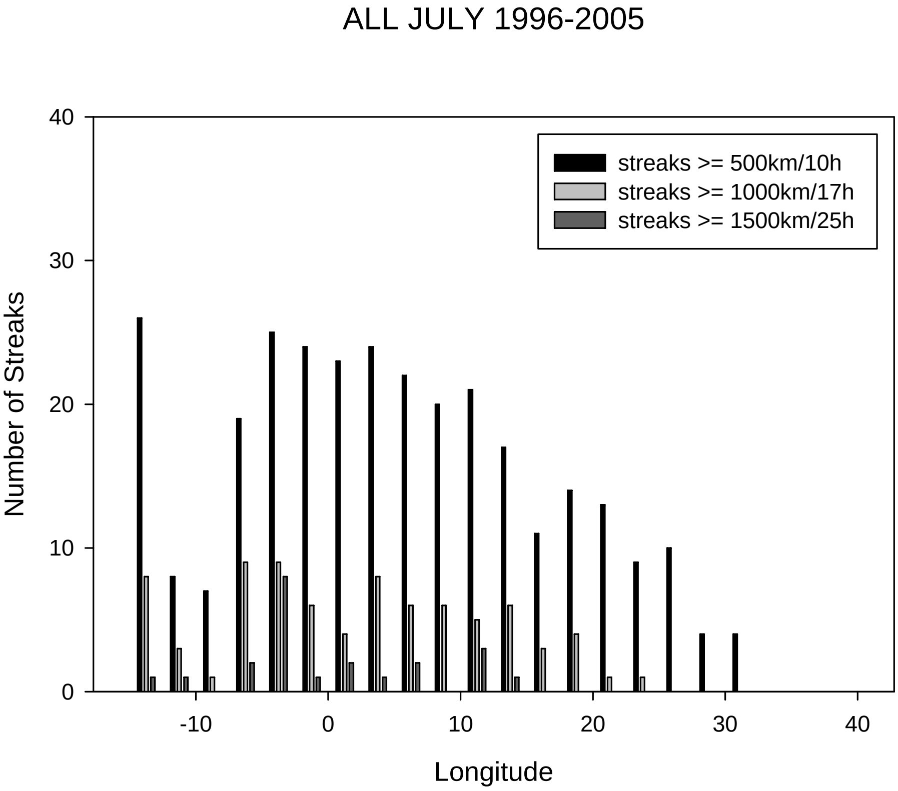

Figure 5-13 *Number of streaks larger in span and longer in duration than 500 km and 10 h, 1000 km and 17 h, and 1500 km and 25 h centred inside each 2.5° longitude band. The number of cases in each category during July 1996-2005 is indicated.*

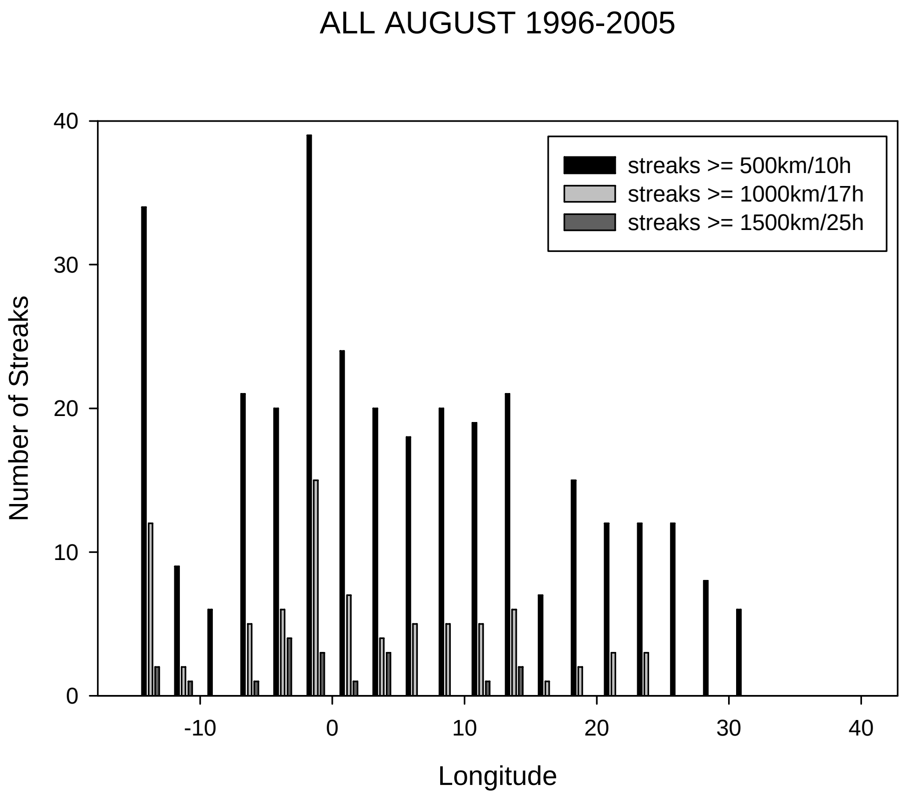

Figure 5-14 *Number of streaks larger in span and longer in duration than 500 km and 10 h, 1000 km and 17 h, and 1500 km and 25 h centred inside each 2.5° longitude band. The number of cases in each category during August 1996-2005 is indicated.*

5.2 Longitudinal distribution of streaks identified by the recurrence frequency analysis

The analysis of the distribution along the longitudinal domain of the streaks that tend to reoccur with a particular frequency could be a useful tool to identify the developing areas of these convective systems.

The definition of exceedance value of span, duration or speed previously given in this chapter implies that only the larger in span, longer in life or faster streaks, that developed during each warm season or during each month of the warm season, are now taken into account. For example, the analysis of the longitudinal distribution of the events belonging to the "two per month" recurrence frequency category for a particular warm season, consists in the identification of the longitude of the starting points of the eight larger in span, longer in life or faster streaks.

The histograms of Fig. 5-15, 5-16 and 5-17 represent the mean numbers of events of the 10 warm seasons, for each recurrence frequency category, centred inside each 2.5° longitudinal band.

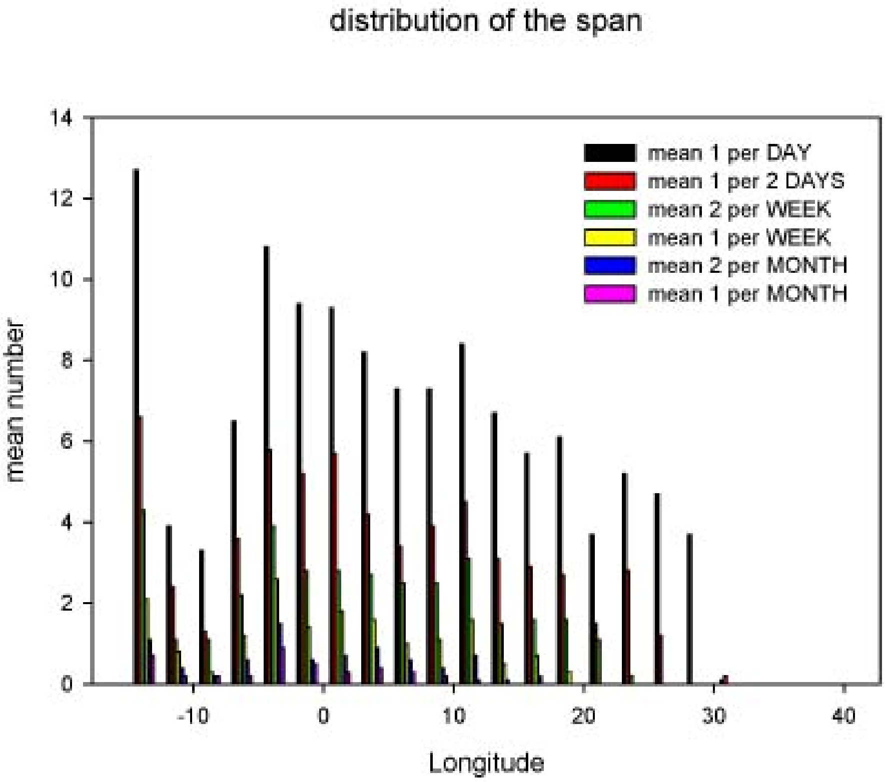

Figure 5-15 *Number of streaks belonging to the span recurrence frequencies and centred inside each 2.5° longitude band. The numbers of each category are the mean numbers of the 1996-2005 warm seasons.*

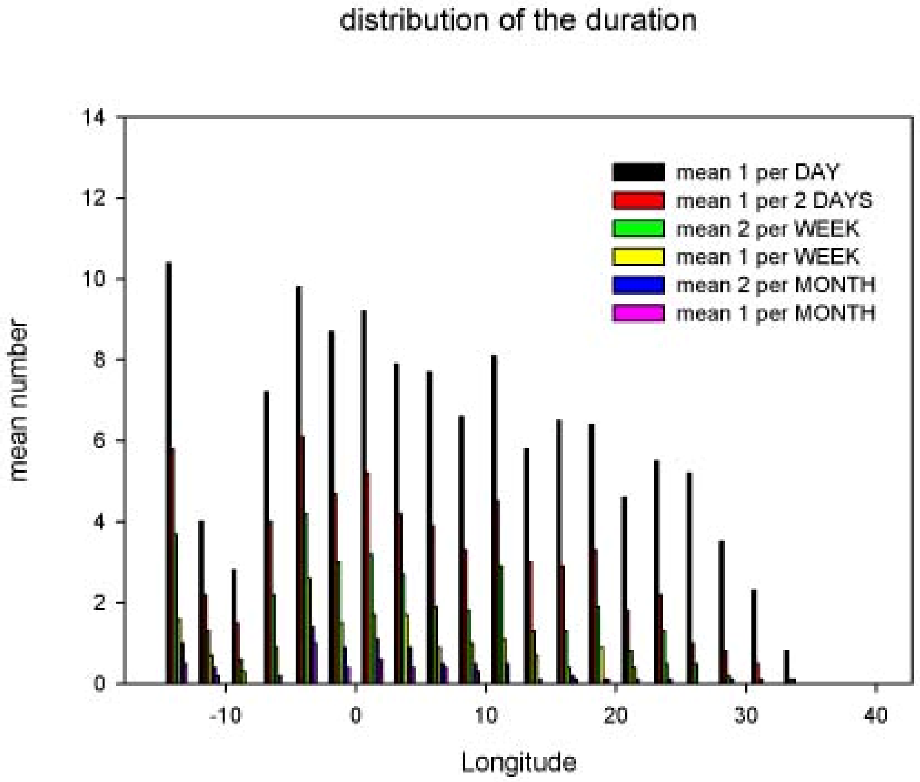

Figure 5-16 *Number of streaks belonging to the duration recurrence frequencies and centred inside each 2.5° longitude band. The numbers of each category are the mean numbers of the 1996-2005 warm seasons.*

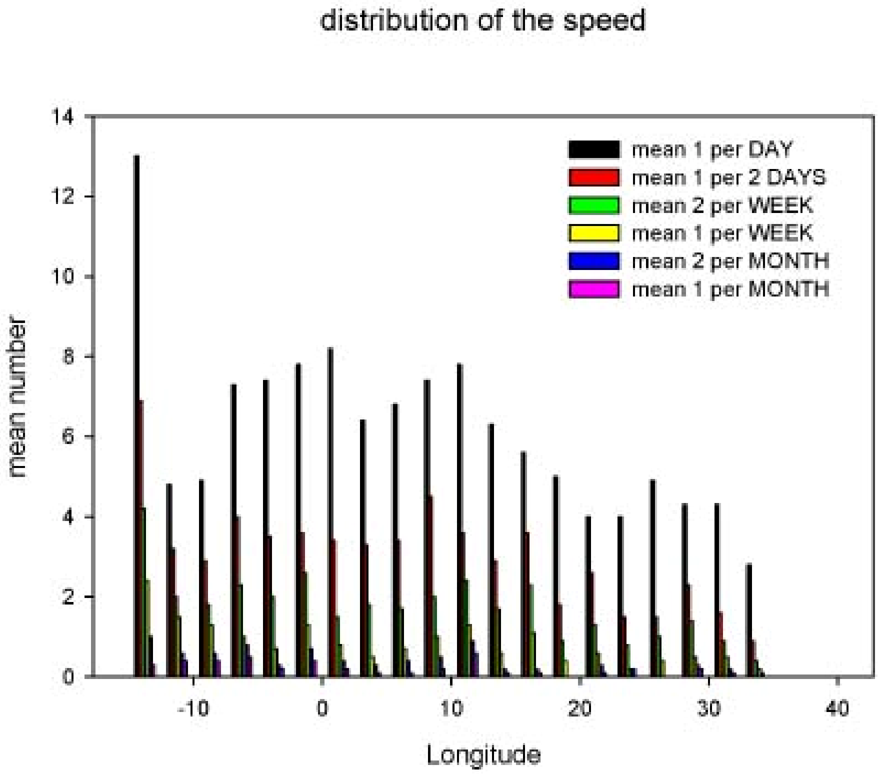

Figure 5-17 *Number of streaks belonging to the speed recurrence frequencies and centred inside each 2.5° longitude band. The numbers of each category are the mean numbers of the 1996-2005 warm seasons.*

Span and duration histograms present similar distributions, characterized by a peak over the Atlantic Ocean, and a decreasing number of events originated from 15° W to the end of the analysis domain. Others peaks are observed in correspondence to the Atlantic Coasts and near the mountain chains, as the Pyrenees and the Alps. The speed distribution shows an higher number of fast streaks arriving from the Atlantic Ocean, besides other lower peaks localized near the mountain chains. Apart from the western peak, the 10 year mean speed distribution seems to be more uniform.

The intraseasonal variation of the distribution of the larger, longer, and faster streaks have also been studied. Figures 5-18 to 5-29 show the mean number of events centred inside each 2.5° longitude band, developed during the 10 months of May, June, July, and August.

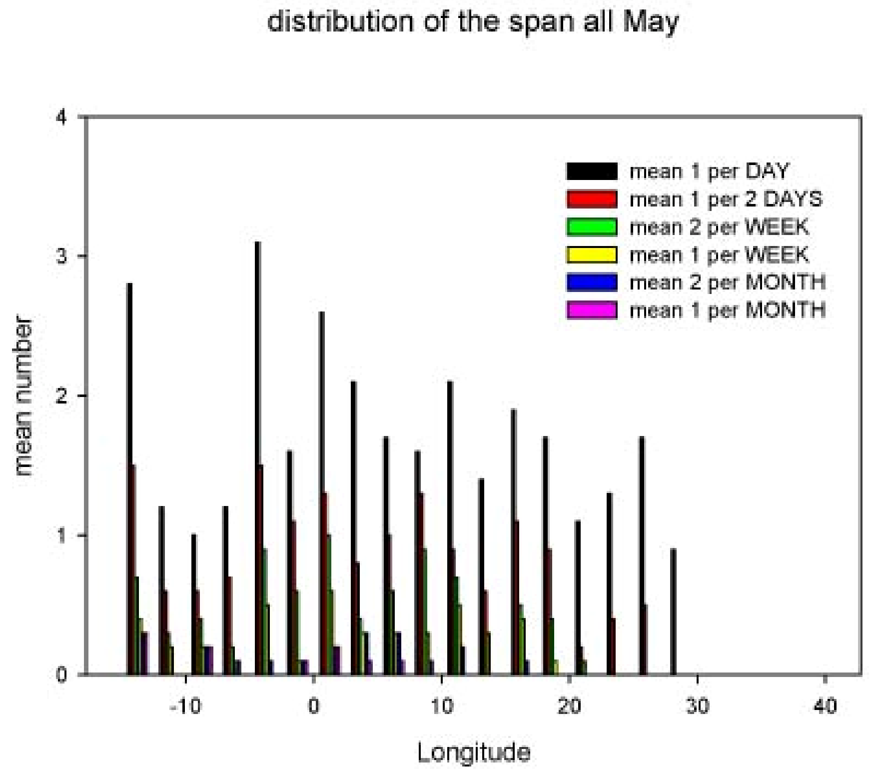

Figure 5-18 *Number of streaks belonging to the span recurrence frequencies and centred inside each 2.5° longitude band. The numbers of each category are the mean numbers of the 1996-2005 months of May.*

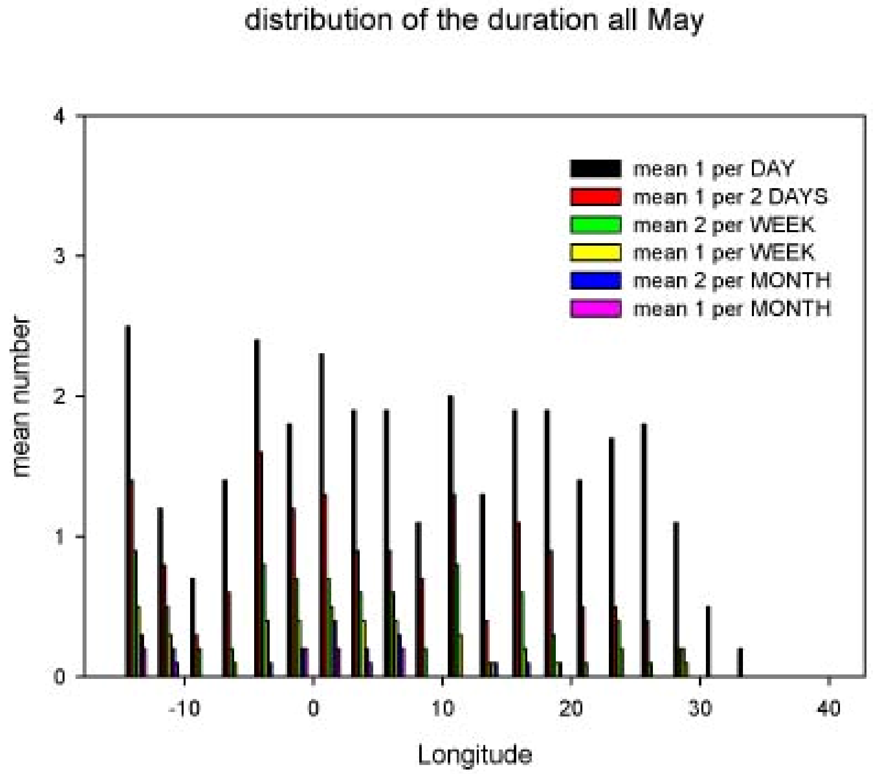

Figure 5-19 *Number of streaks belonging to the duration recurrence frequencies and centred inside each 2.5° longitude band. The numbers of each category are the mean numbers of the 1996-2005 months of May.*

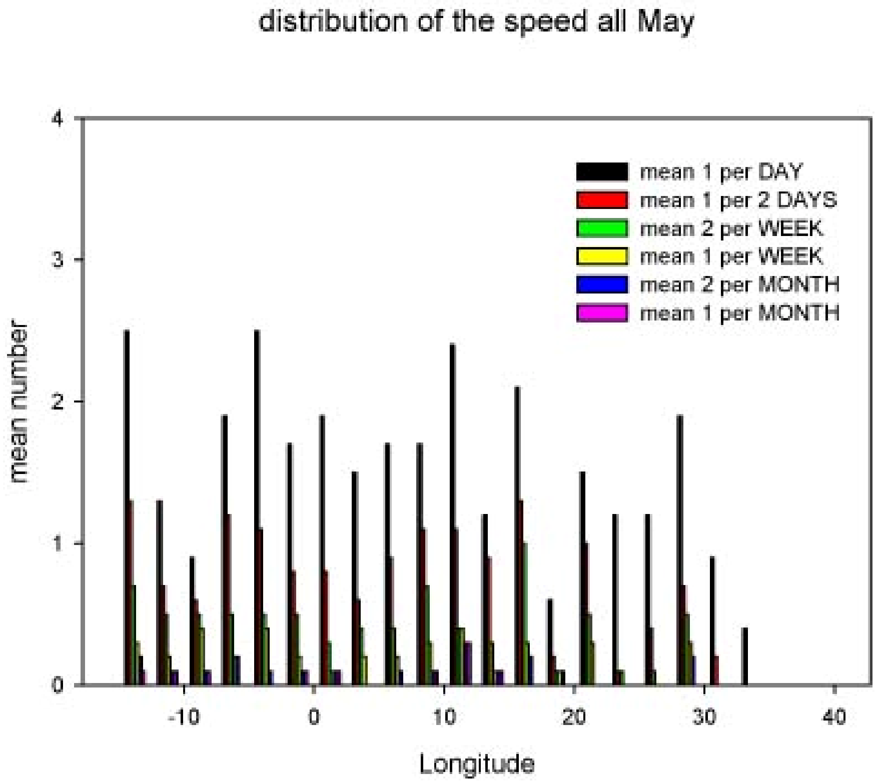

Figure 5-20 *Number of streaks belonging to the speed recurrence frequencies and centred inside each 2.5° longitude band. The numbers of each category are the mean numbers of the 1996-2005 months of May.*

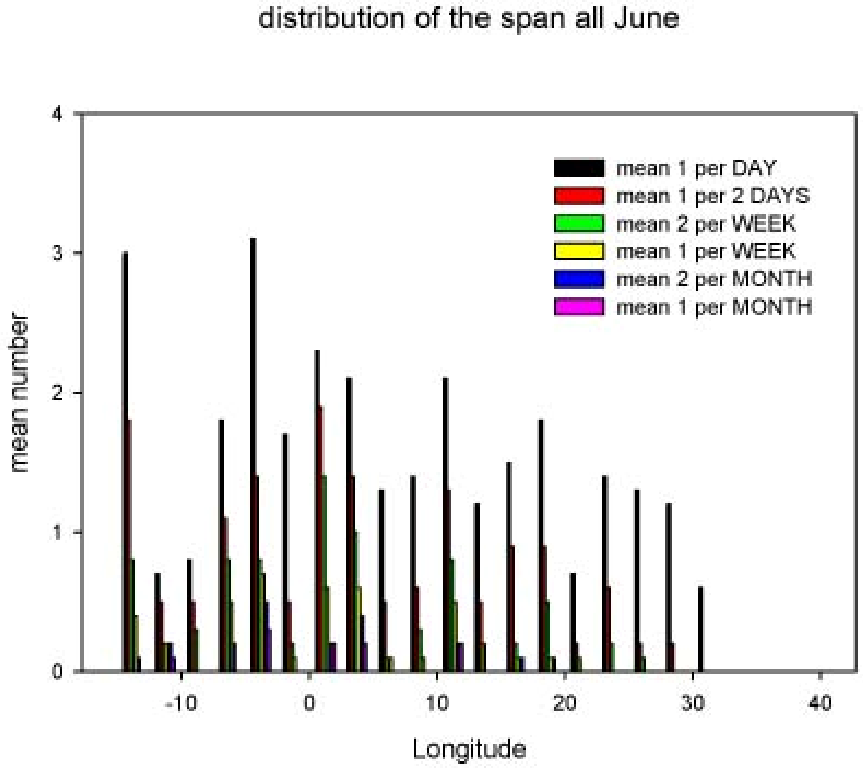

Figure 5-21 *Number of streaks belonging to the span recurrence frequencies and centred inside each 2.5° longitude band. The numbers of each category are the mean numbers of the 1996-2005 months of June.*

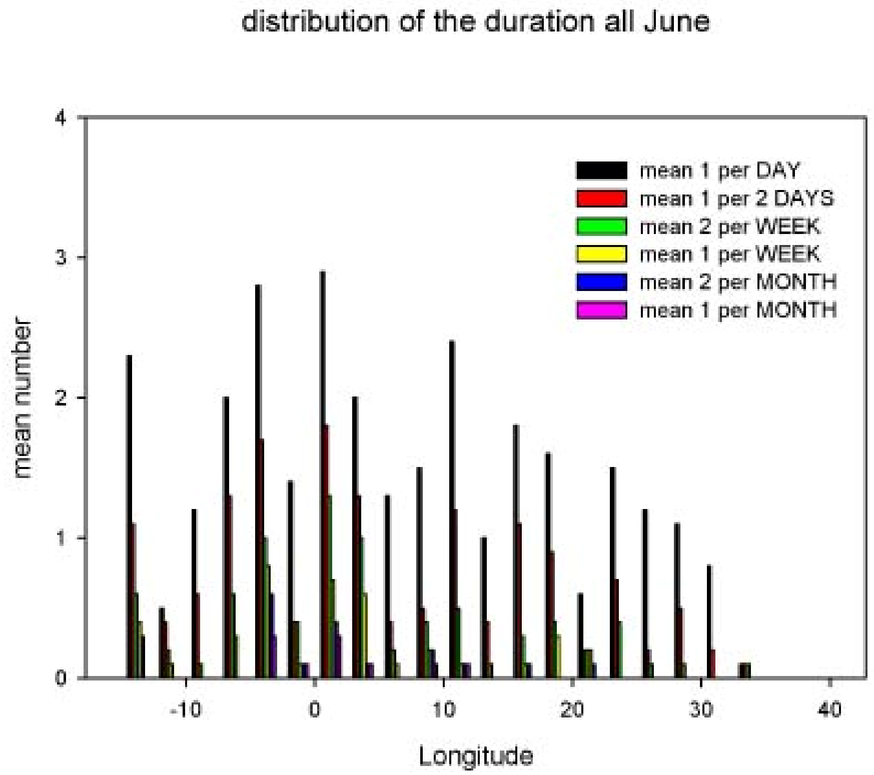

Figure 5-22 *Number of streaks belonging to the duration recurrence frequencies and centred inside each 2.5° longitude band. The numbers of each category are the mean numbers of the 1996-2005 months of June.*

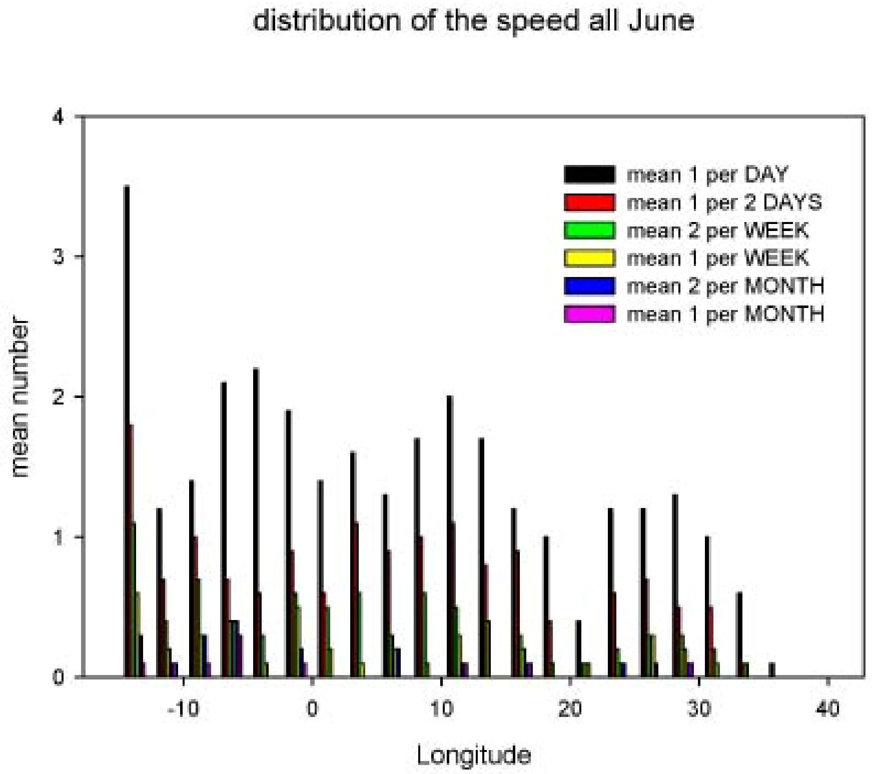

Figure 5-23 *Number of streaks belonging to the speed recurrence frequencies and centred inside each 2.5° longitude band. The numbers of each category are the mean numbers of the 1996-2005 months of June.*

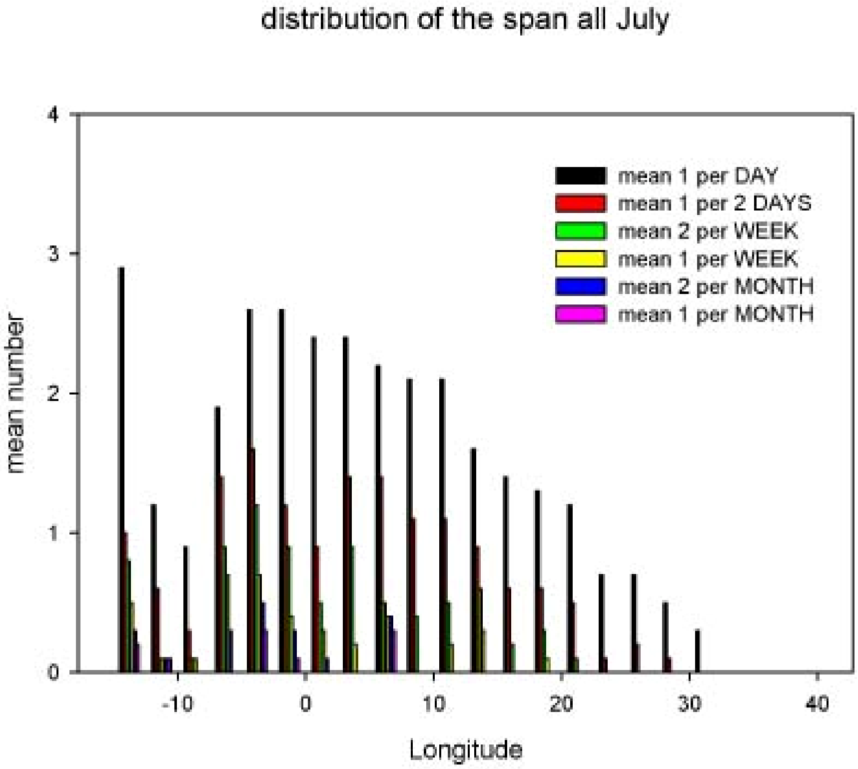

Figure 5-24 *Number of streaks belonging to the span recurrence frequencies and centred inside each 2.5° longitude band. The numbers of each category are the mean numbers of the 1996-2005 months of July.*

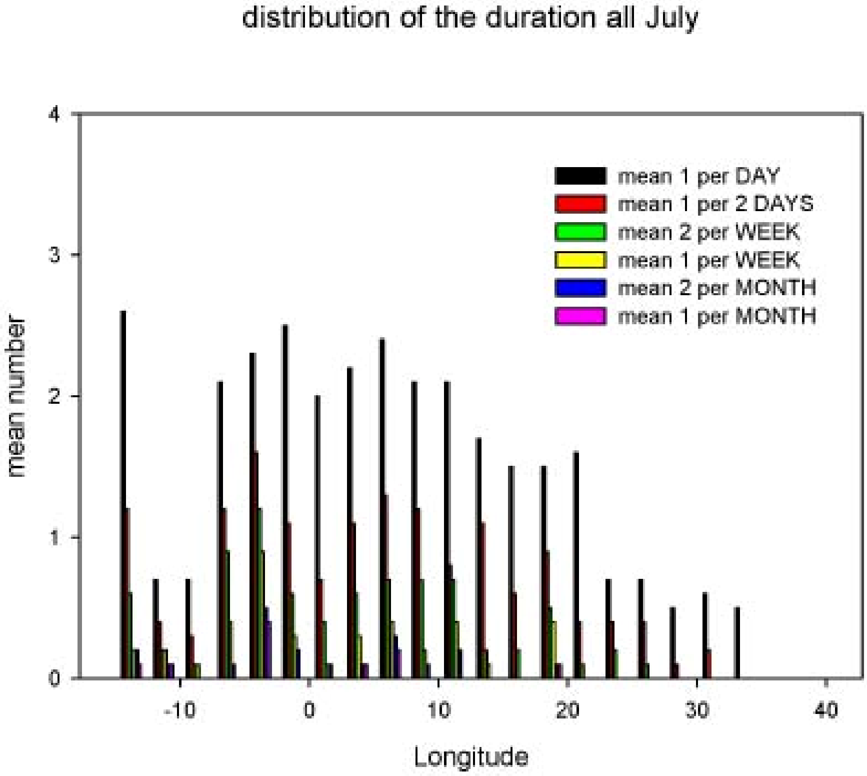

Figure 5-25 *Number of streaks belonging to the duration recurrence frequencies and centred inside each 2.5° longitude band. The numbers of each category are the mean numbers of the 1996-2005 months of July.*

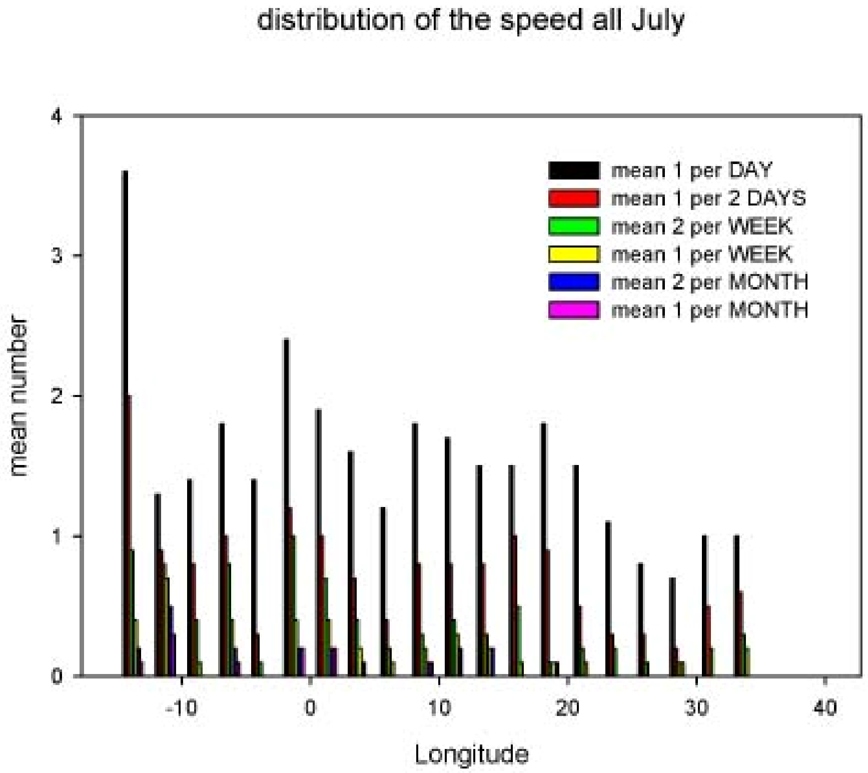

Figure 5-26 *Number of streaks belonging to the speed recurrence frequencies and centred inside each 2.5° longitude band. The numbers of each category are the mean numbers of the 1996-2005 months of July.*

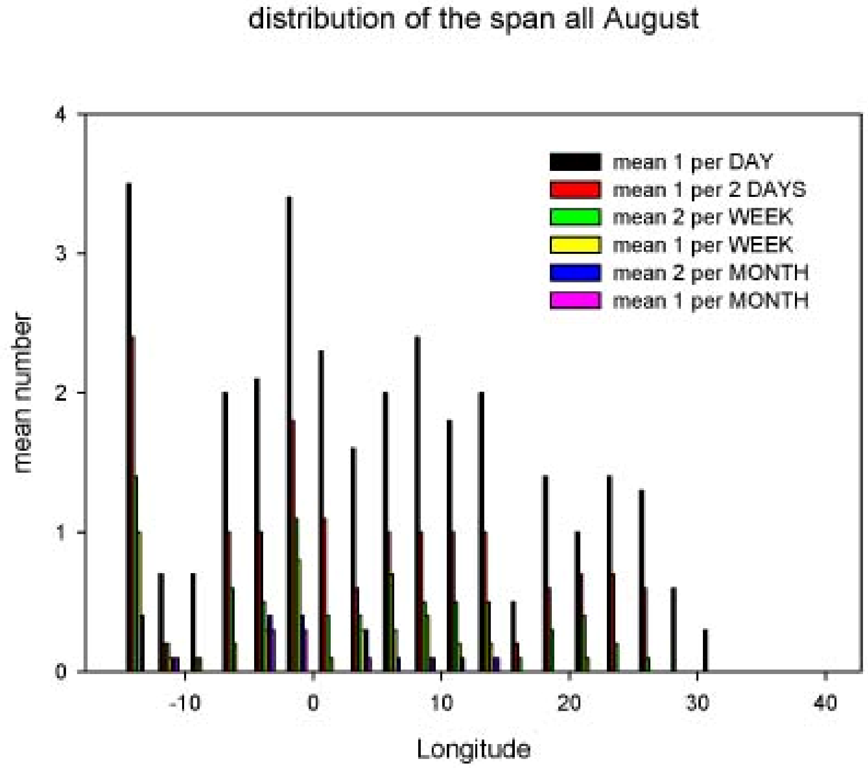

Figure 5-27 *Number of streaks belonging to the span recurrence frequencies and centred inside each 2.5° longitude band. The numbers of each category are the mean numbers of the 1996-2005 months of August.*

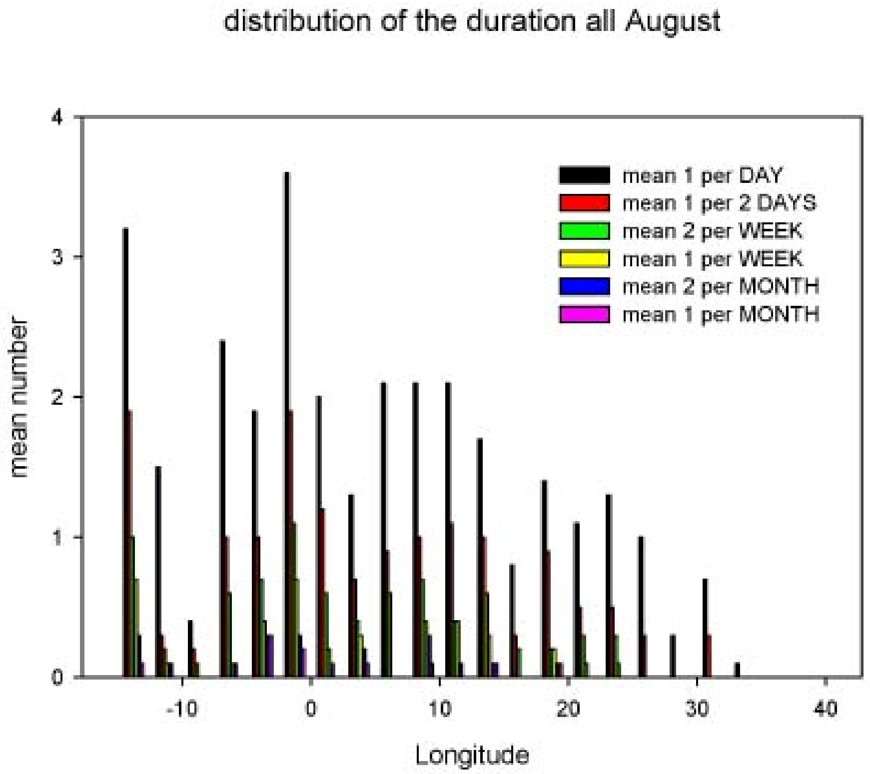

Figure 5-28 *Number of streaks belonging to the duration recurrence frequencies and centred inside each 2.5° longitude band. The numbers of each category are the mean numbers of the 1996-2005 months of August.*

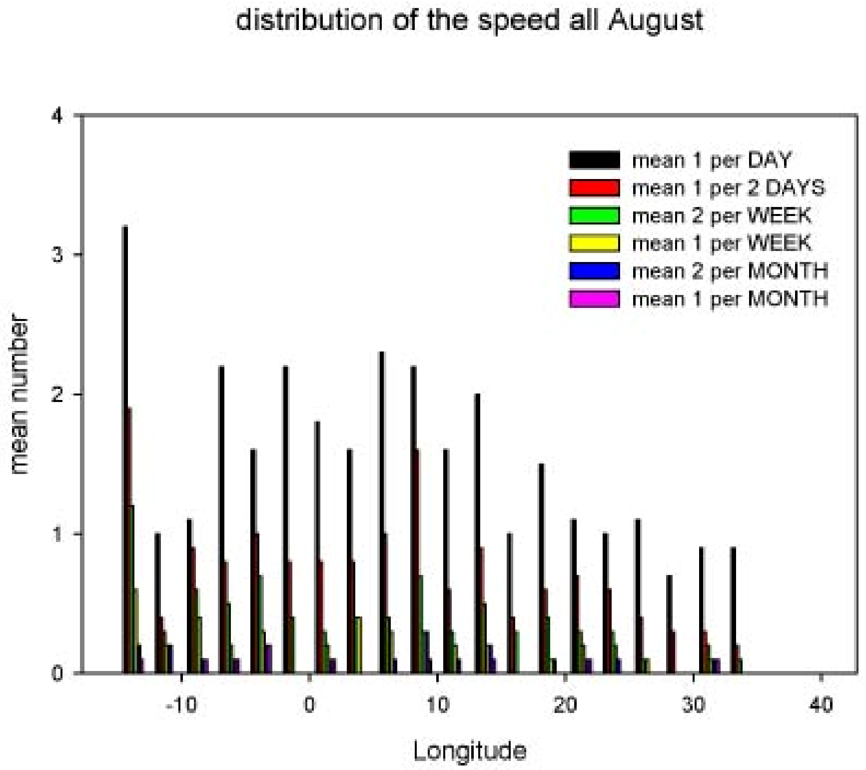

Figure 5-29 *Number of streaks belonging to the speed recurrence frequencies and centred inside each 2.5° longitude band. The numbers of each category are the mean numbers of the 1996-2005 months of August.*

The 10 months mean number of streaks with a larger span is higher over the Atlantic Ocean, the Atlantic Coasts, the Pyrenees, the Alps, and the Balkans, when the month of May, June or August are taken into account, while the distribution of July is characterized by a decreasing mean number of streaks trend from 5° W to 30° E.

The distributions of longer streaks present peaks near the Atlantic Coasts, the Pyrenees, and the Alps in May and June. The mean distribution obtained from the 10 months of July is more uniform from 5° W to 20° E, while the mean activity of August is more intense over the Atlantic Ocean. These two monthly mean distributions both present a relevant peak over the Atlantic Ocean, and a suppression of activity starting from 30° E to the eastern end of the domain.

The monthly mean distribution of faster streaks has the highest peak over the Atlantic Ocean in June, July, and August. A more uniform distribution is observed along the other longitudinal bands. The mean distribution of May is characterized by a higher number of peaks placed near the mountain chains.

The distribution of the “one per month” and “two per month” recurrence frequency categories are plotted separately from the other categories. This analysis in effect considers only the four or eight, respectively, larger, longer or faster streaks that developed during each season. In the case of the monthly analysis, the two categories of recurrence frequency are composed by one or two streaks respectively.

Figures 5-30 to 5-32 reports the histograms that represent the mean number of streaks developed during the 10 analysed warm season, belonging to these two recurrence frequencies. Longitudinal bands of 2.5° are considered as usual.

It is interesting to note that the distributions of span and duration present streaks only between 15° W and 25° E, while faster streaks developed also beyond this longitudinal band. Furthermore, streaks with larger span and longer life tend to be originated on average near the Atlantic Coasts, the Pyrenees, and the Atlantic Ocean, while the speed distribution presents a significant peak over the Alps, besides the one over the Atlantic Ocean.

The histogram analysis carried out considering “one per month” and “two per month” recurrence frequencies has been done also for monthly categories, in order to evaluate intraseasonal variations (see Fig. 5-32 to 5-43).

The development of longer streaks is more frequent over the Pyrenees in May and June. The Atlantic Coasts are more active in June and July, while in August the peaks of the distribution are localized near the Atlantic Ocean, the Atlantic Coasts, and the Alps.

The span distribution shows peaks over the Atlantic Coasts from July to August. The development of larger streaks shows up in a narrower and western longitudinal band in July, with respect to the others months. Finally, faster streaks tended to be originated near the Alps in May and August, over the Atlantic Ocean and near the Atlantic Coasts in June and July.

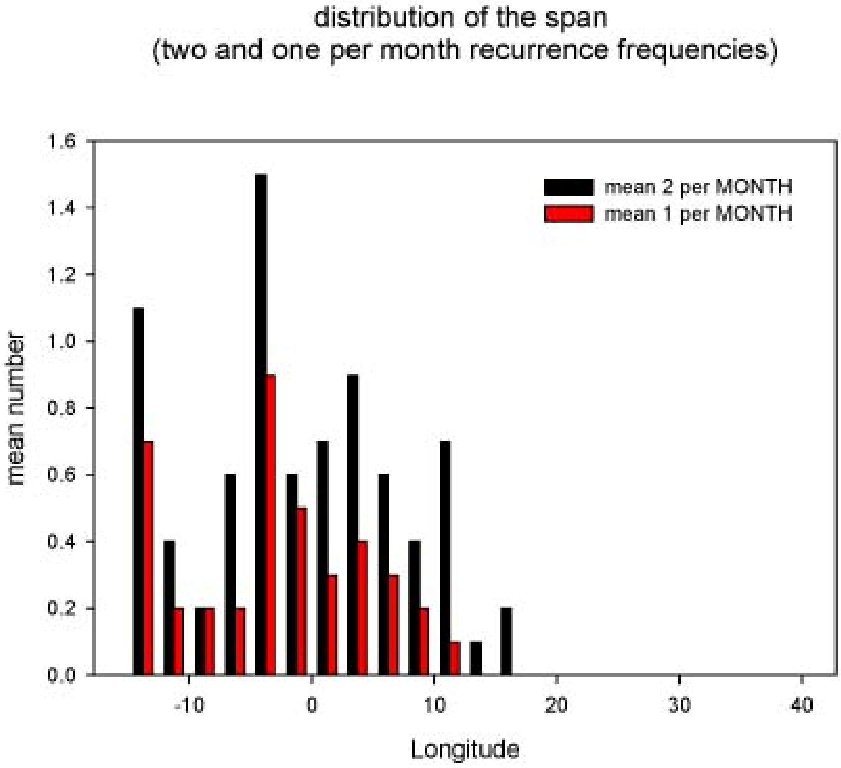

Figure 5-30 *Number of streaks belonging to the one per month and two per month span recurrence frequencies and centred inside each 2.5° longitude band. The numbers of each category are the mean numbers of the 1996-2005 warm seasons.*

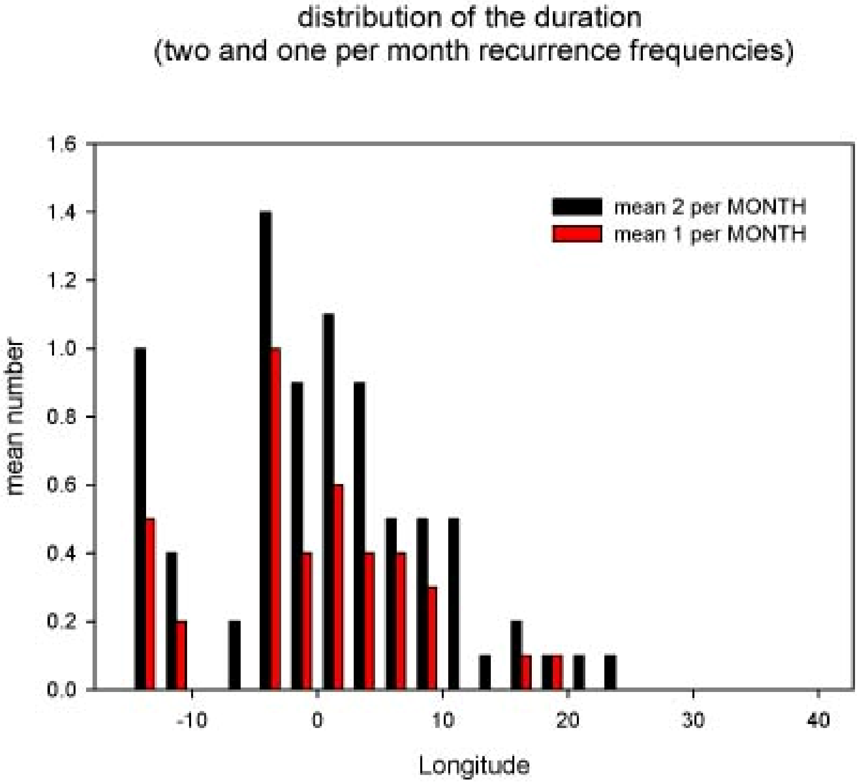

Figure 5-31 *Number of streaks belonging to the one per month and two per month duration recurrence frequencies and centred inside each 2.5° longitude band. The numbers of each category are the mean numbers of the 1996-2005 warm seasons.*

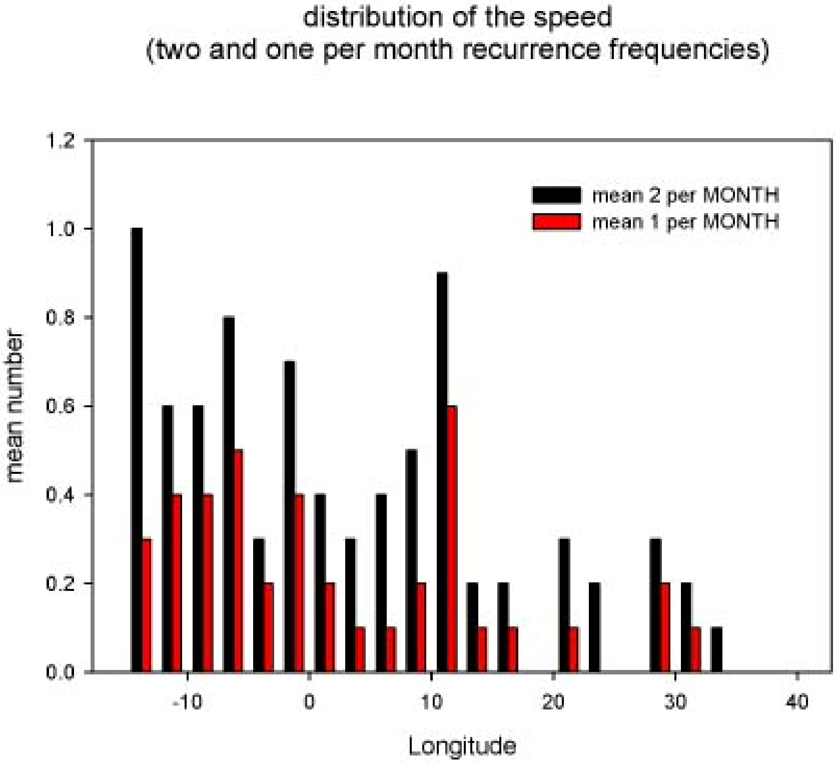

Figure 5-32 *Number of streaks belonging to the one per month and two per month speed recurrence frequencies and centred inside each 2.5° longitude band. The numbers of each category are the mean numbers of the 1996-2005 warm seasons.*

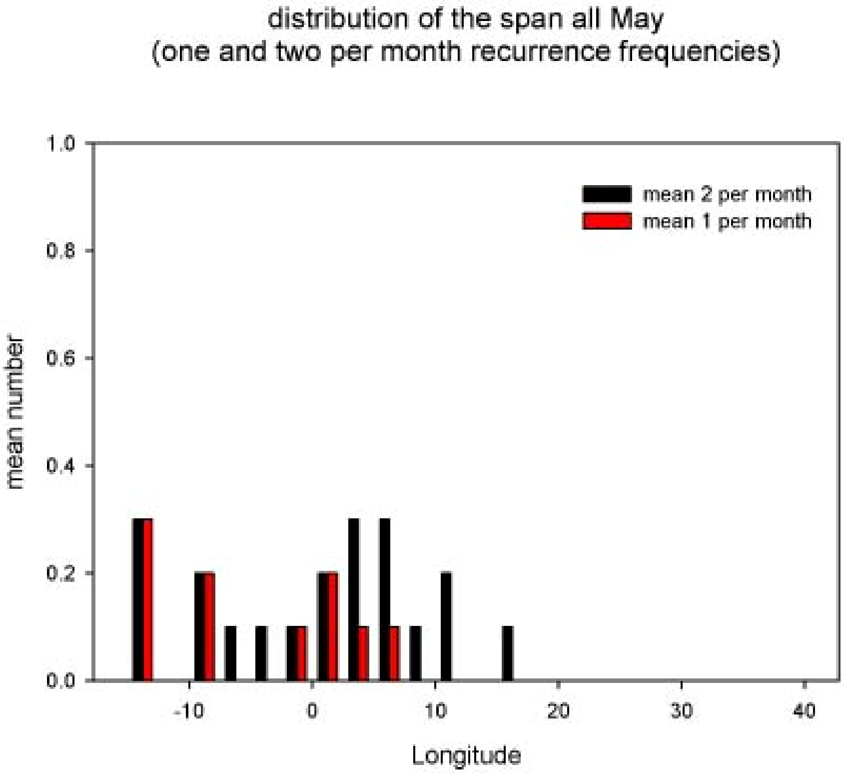

Figure 5-33 *Number of streaks belonging to the one per month and two per month span recurrence frequencies and centred inside each 2.5° longitude band. The numbers of each category are the mean numbers of the 1996-2005 months of May.*

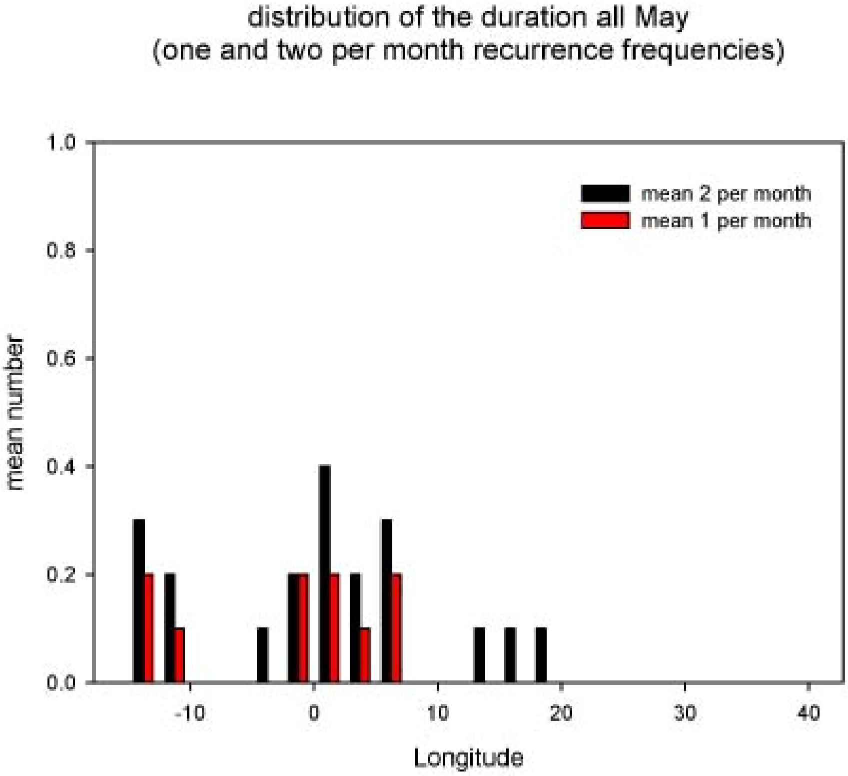

Figure 5-34 *Number of streaks belonging to the one per month and two per month duration recurrence frequencies and centred inside each 2.5° longitude band. The numbers of each category are the mean numbers of the 1996-2005 months of May.*

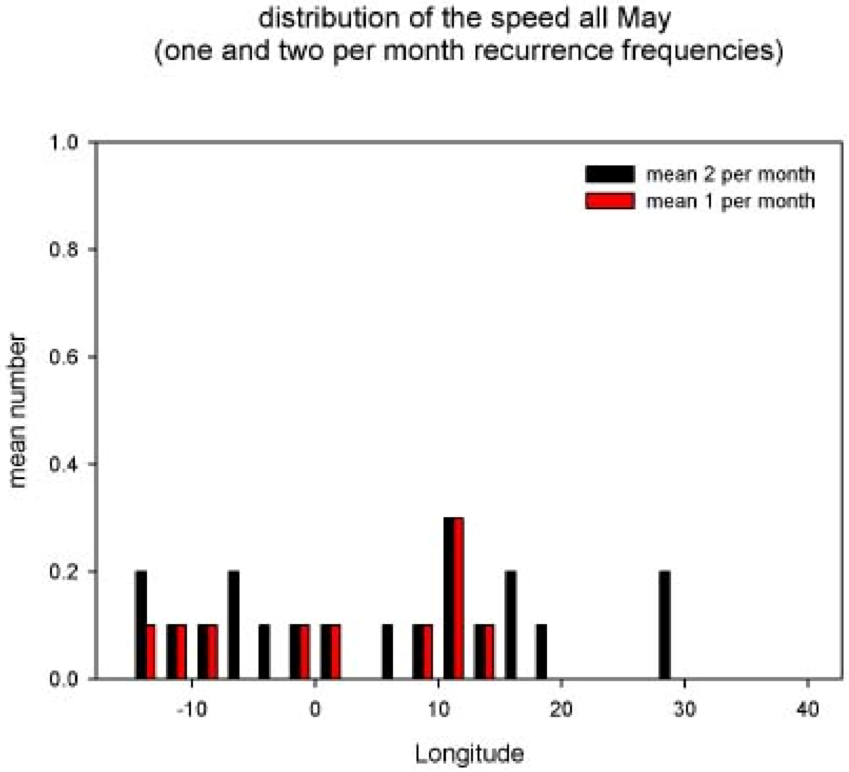

Figure 5-35 *Number of streaks belonging to the one per month and two per month speed recurrence frequencies and centred inside each 2.5° longitude band. The numbers of each category are the mean numbers of the 1996-2005 months of May.*

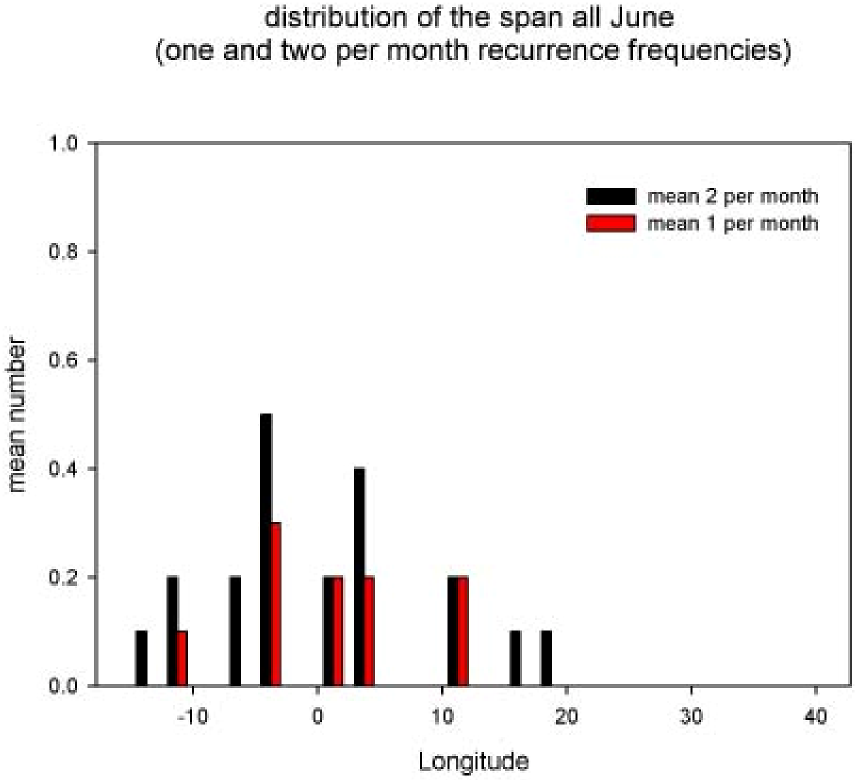

Figure 5-36 *Number of streaks belonging to the one per month and two per month span recurrence frequencies and centred inside each 2.5° longitude band. The numbers of each category are the mean numbers of the 1996-2005 months of June.*

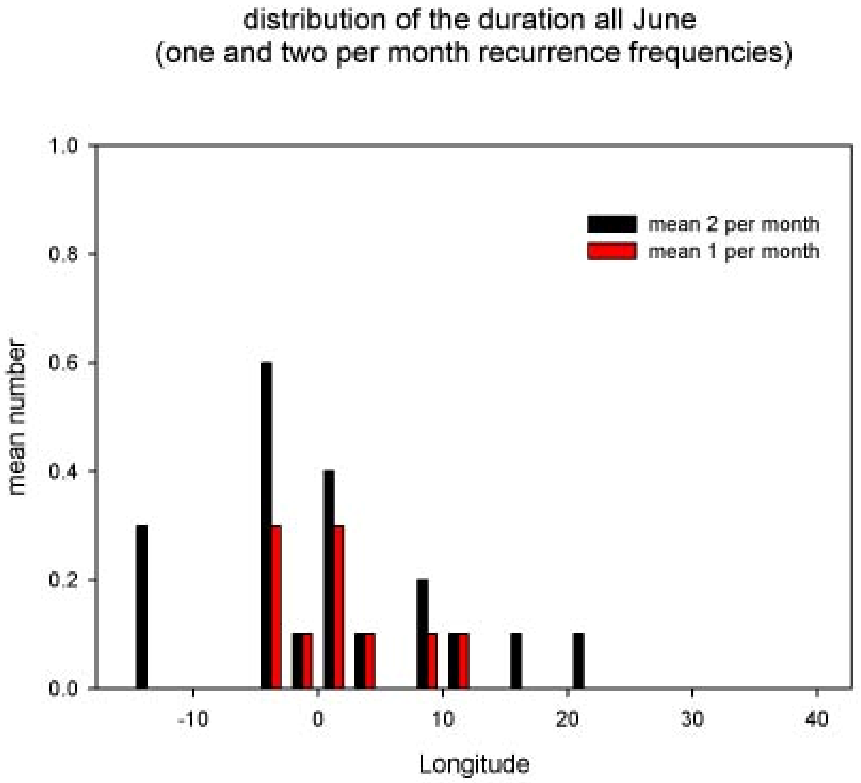

Figure 5-37 *Number of streaks belonging to the one per month and two per month duration recurrence frequencies and centred inside each 2.5° longitude band. The numbers of each category are the mean numbers of the 1996-2005 months of June.*

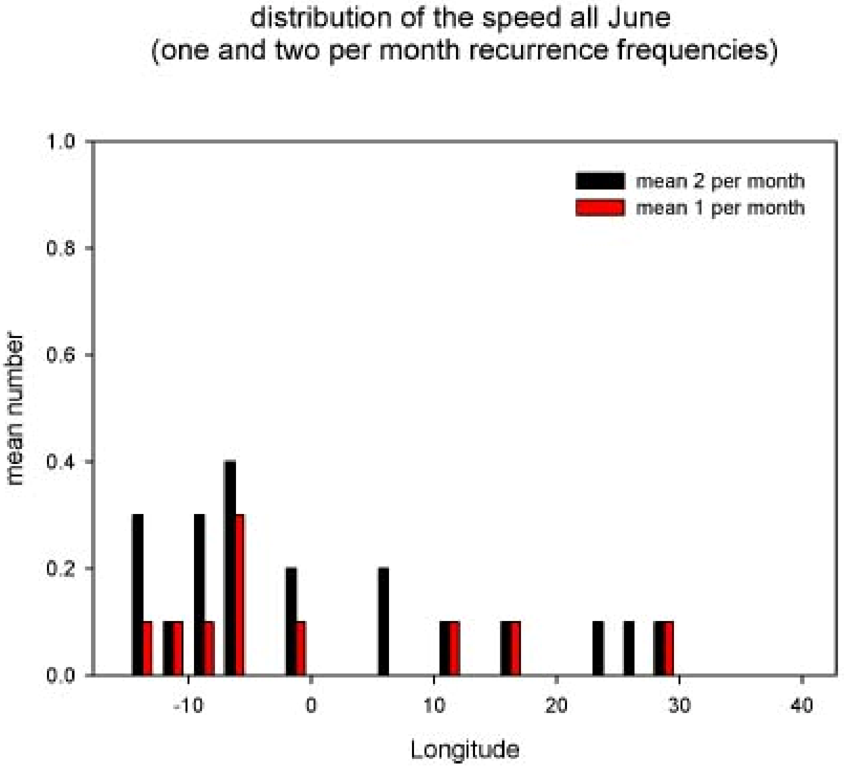

Figure 5-38 *Number of streaks belonging to the one per month and two per month speed recurrence frequencies and centred inside each 2.5° longitude band. The numbers of each category are the mean numbers of the 1996-2005 months of June.*

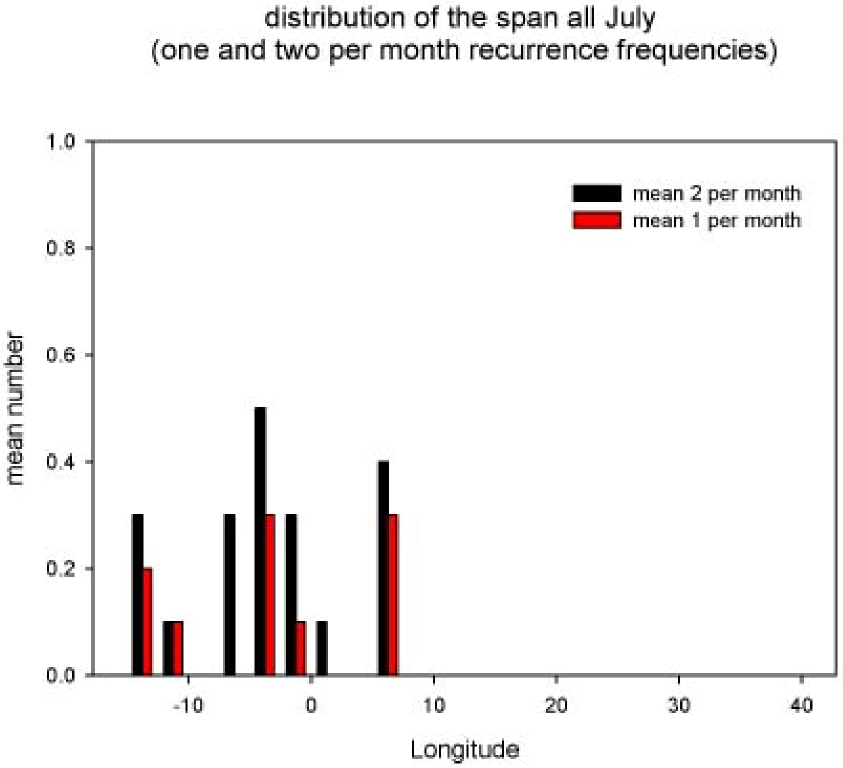

Figure 5-39 *Number of streaks belonging to the one per month and two per month span recurrence frequencies and centred inside each 2.5° longitude band. The numbers of each category are the mean numbers of the 1996-2005 months of July.*

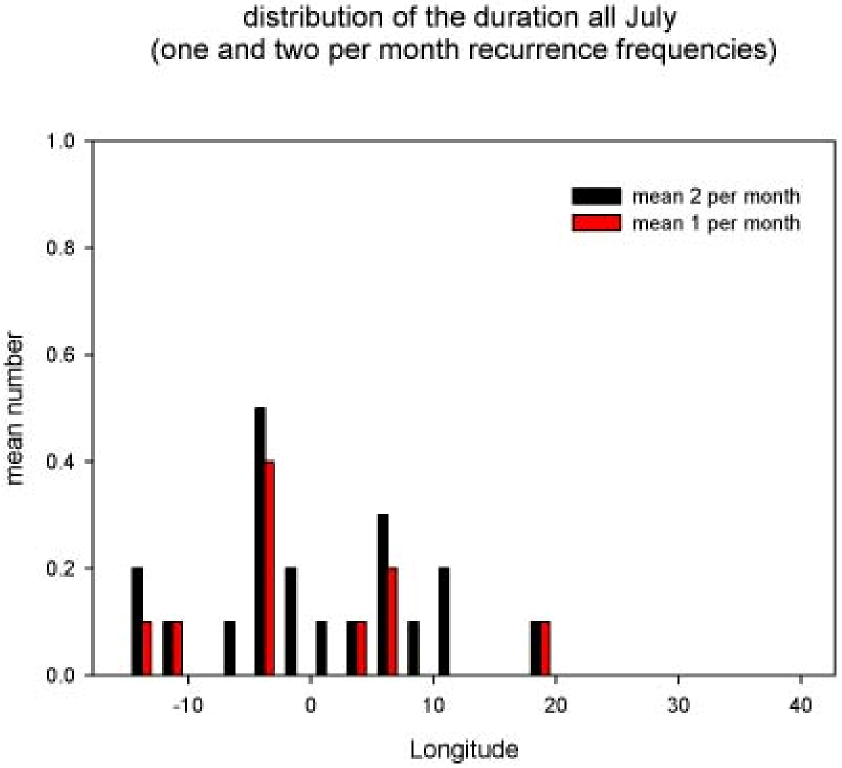

Figure 5-40 *Number of streaks belonging to the one per month and two per month duration recurrence frequencies and centred inside each 2.5° longitude band. The numbers of each category are the mean numbers of the 1996-2005 months of July.*

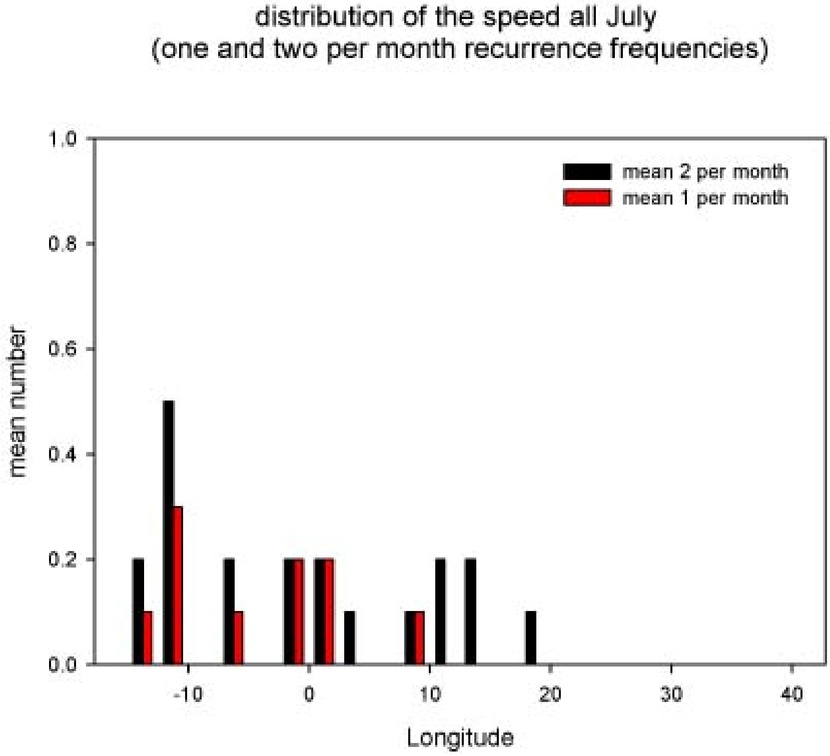

Figure 5-41 *Number of streaks belonging to the one per month and two per month speed recurrence frequencies and centred inside each 2.5° longitude band. The numbers of each category are the mean numbers of the 1996-2005 months of July.*

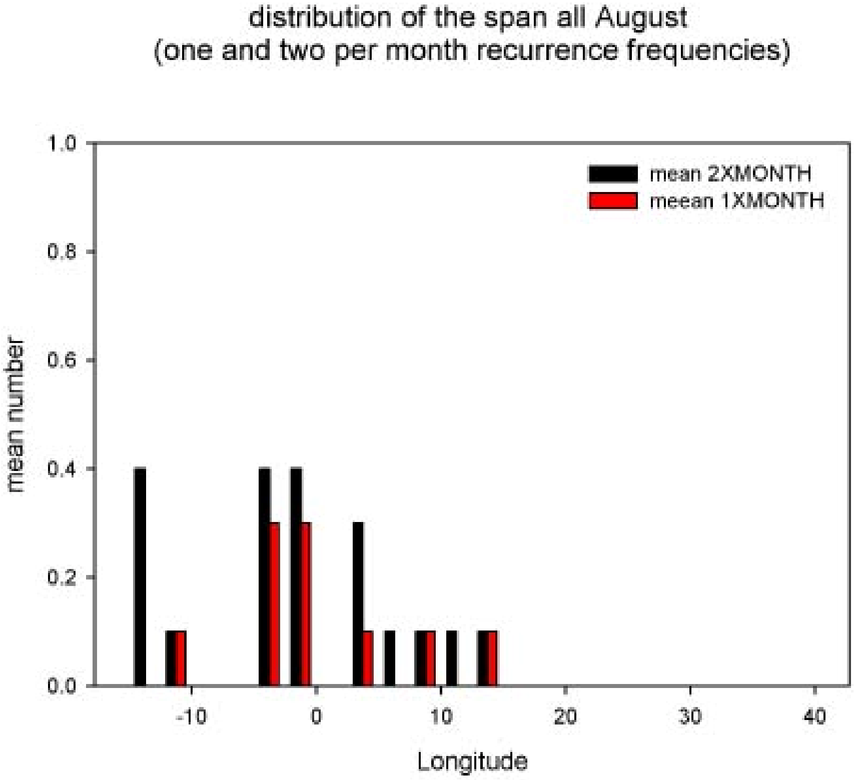

Figure 5-42 *Number of streaks belonging to the one per month and two per month recurrence frequencies considered according to the span and centred inside each 2.5° longitude band. The numbers of each category are the mean numbers of the 1996-2005 months of August.*

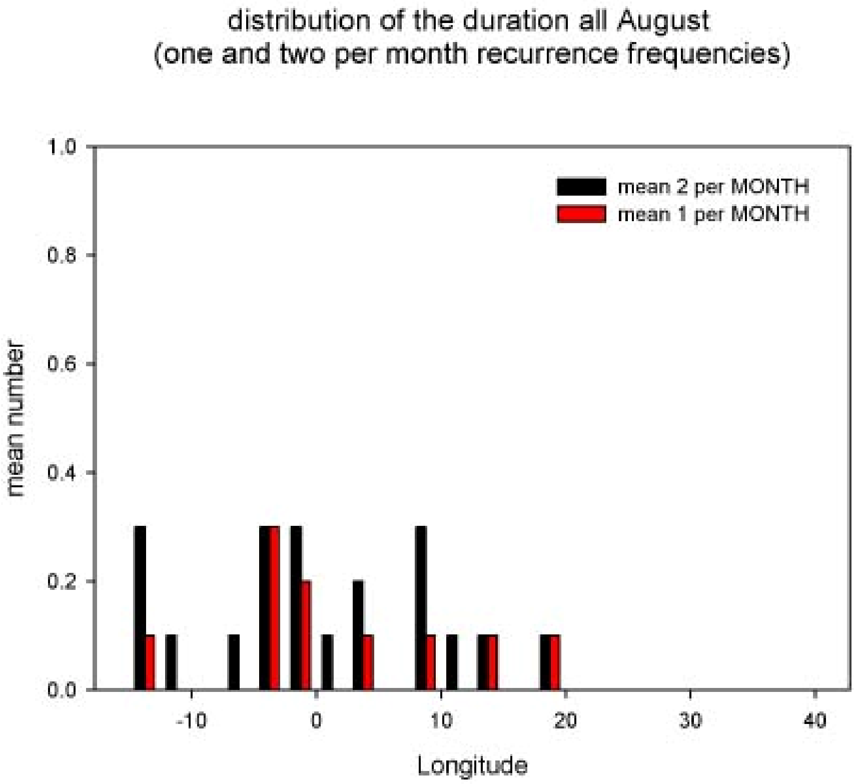

Figure 5-43 *Number of streaks belonging to the one per month and two per month duration recurrence frequencies and centred inside each 2.5° longitude band. The numbers of each category are the mean numbers of the 1996-2005 months of August.*

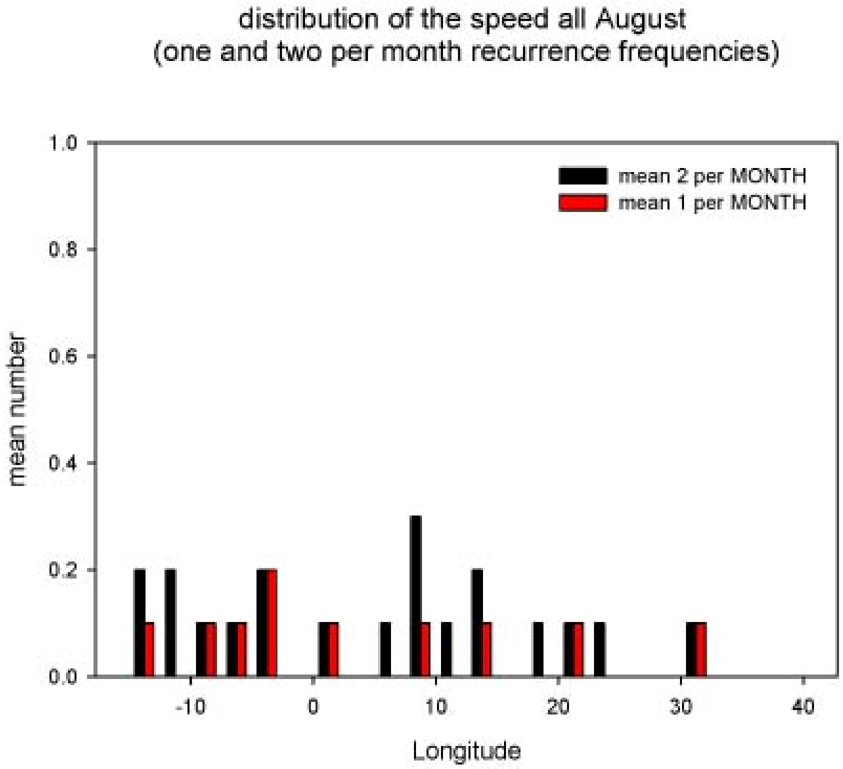

Figure 5-44 *Number of streaks belonging to the one per month and two per month speed recurrence frequencies and centred inside each 2.5° longitude band. The numbers of each category are the mean numbers of the 1996-2005 months of August.*

6. Frequency and periodicity of cloudiness

6.1 Spatial distribution of clod clouds

To evaluate the spatial distribution of cold cloud frequency, maps of percentage of cold cloud persistence were drawn for i) May-August mean of each year, ii) mean of each month for all 10 years, and iii) the average of the whole 10 year period. The latter is shown in Figure 6-1.

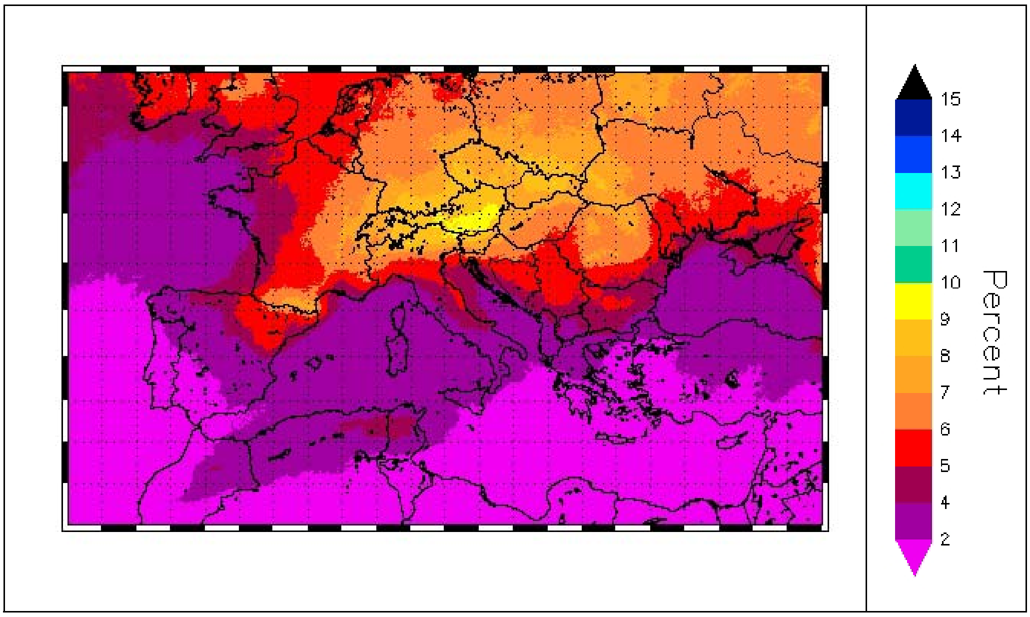

Figure 6-1 *Average cold cloud percentage persistence over the whole period May-August 1996-2005 .*

Yearly maps of cold cloud persistence during the period May to August reveal that a clear signal of persistence of clouds with cold top corresponds to the lee of the Alps, the Pyrenees, the Balkans and the Carpathians (see Figures in Appendix A). This signal is obviously smoothed in the 10 years mean map because of the averaging process.

To evaluate the seasonal distribution of cold clouds 10 years mean maps for each month that composes the warm season were considered.

The average spatial distribution of cold cloud frequency in Figure 6-2 shows distinct variations from May to August. Maximum percentage values of cold clouds are found in May (Fig. 6-2a), especially in correspondence of and in the lee of the Pyrenees, the Alps and Anatolia, indicating a clear role of these mountain chains in the initiation of convection; high values are also found over western Mediterranean pointing to an influence of the Atlas mountains of North Africa, and in the wake of the Balkans and the Carpathians.

The percentage frequency values decrease in magnitude in June (Fig. 6-2b) with a general northward shift of the maxima above 45°N while still maintaining a maximum in the lee of Pyrenees and some activity in North Africa; as to the rest of the domain, the cloudiness is mainly located over central and eastern Europe.

The June trend intensifies in July (Fig. 6-2c) with the maximum of cold clouds all located in central and eastern Europe. A substantial decrease of the percent cold cloud coverage over Europe is then found in August (Fig. 6-2d), which also sees a returning maximum over the Pyrenees and the Alps.

The cold cloud distribution seems thus connected with the Atlantic front passage over the area, which is more frequent during the last part of spring and almost totally ceases in summer over the Mediterranean due to the persistent anticyclonic circulation. A certain amount of cold cloud development remains at higher latitudes were the fronts still break in and induce local cloud development.

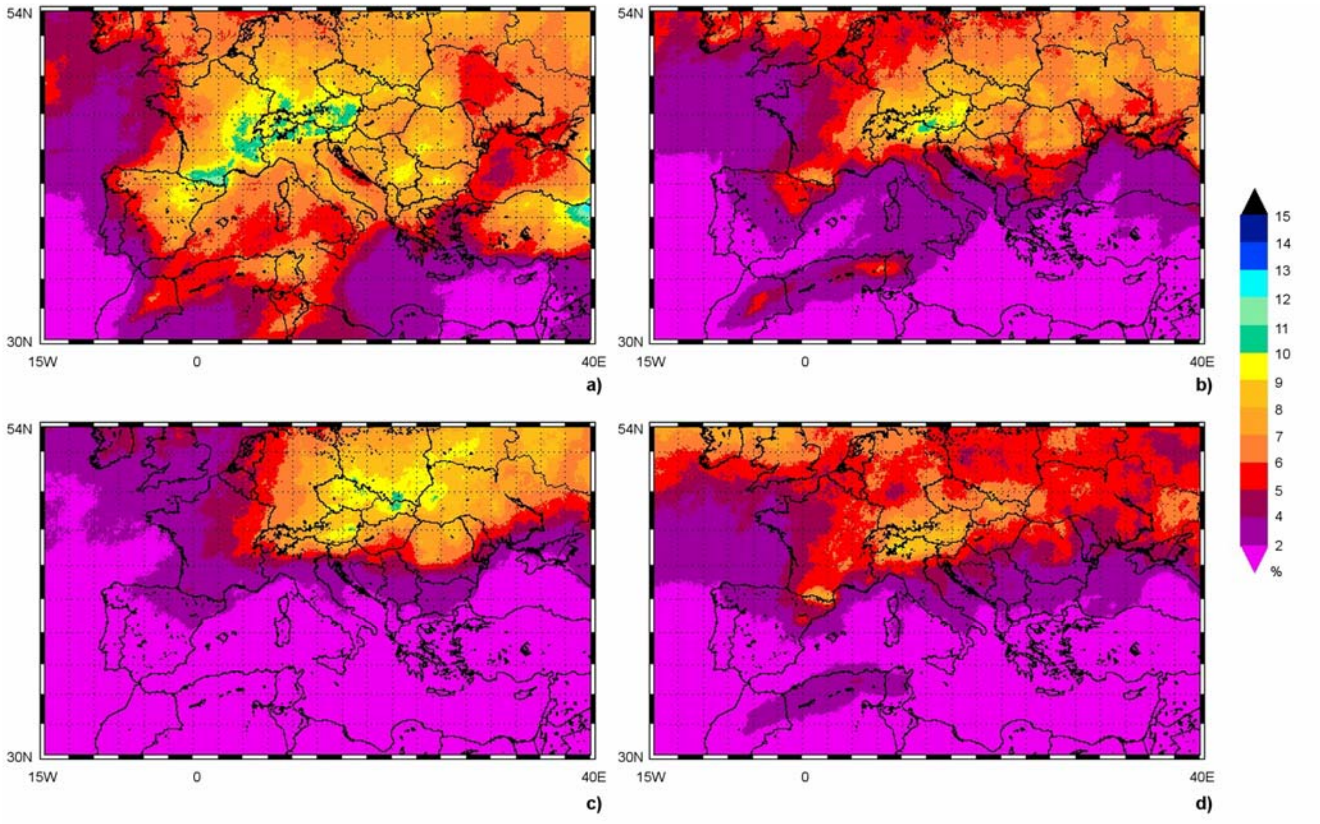

Figure 6-2 *Percentage of cloud coverage with $T_b < 241$ K averaged over the 1996-2005 period: a) May, b) June, c) July, and d) August.*

6.2 Periodicity of cold clouds

6.2.1 Fourier analysis

Two different methods are used to analyze the periodicity and phase of cloudiness over the selected domain (Ahijevych *et al.*, 2001; Carbone *et al.*, 2002):

1) frequency of clouds with T_bs < 241 K are averaged over months, seasons and the whole period 1996-2005 to examine coherent structures within the diurnal cycle;
2) discrete Fourier transforms (DFT) are applied along the time dimension of the frequency diagrams to identify those signals in the power spectra that point to diurnal and shorter period oscillations.

Here a brief explanation is presented concerning the nature and the interpretation of the technique, including the formulae directly applied to the analysis of the 10 year dataset.

The technique of harmonic analysis is discussed by many authors including, for example, Wilks (1995).

Fourier analysis, or harmonic analysis, analyzes the various frequency components of a time series. It consists of representing the fluctuations or variations in a time series as a sum of a series of sine and cosine functions. These trigonometric functions are "harmonic" in the sense that they are chosen to have frequencies exhibiting integer multiples of a "fundamental" frequency determined by the sample size of the data series.

In essence, the function *y(t)* can be decomposed into sinusoids of different frequencies ω, which integrate the original function:

$$y(t) = \frac{1}{2\pi}\int_{-\infty}^{\infty} Y(\omega)e^{i\omega t}d\omega \qquad (5\text{-}1)$$

where Y(ω) is defined by

$$Y(\omega) = \int_{-\infty}^{\infty} y(t)e^{-i\omega t}dt\,. \qquad (5\text{-}2)$$

The complex function Y(ω) is called the Fourier transform of *y(t).* It contains the complex amplitudes of the different frequency sinusoids that compose the original function.

In the relationships (5-1) and (5-2), the function *y(t)* is assumed to be defined at all times. However, in reality, one must work with time series constructed from measurements taken at discrete times. Therefore, the DFT must be used. In general, the k^{th} element y_k of an N-element time series *y* can be written as a linear combination of sinusoids.

$$y_k = \frac{1}{N}\sum_{s=0}^{N-1} Y_s e^{i2\pi sk/N} \qquad (5\text{-}3)$$

where each coefficient Y_s is equal to

$$Y_s = \sum_{k=0}^{N-1} y_k e^{-i2\pi sk/N}. \qquad (5\text{-}4)$$

Together, the N coefficients define the DFT of *y*. Each coefficient Y_s represents the complex amplitude of the s^{th} sinusoid component of y_k, while its magnitude equals the power associated with that component.

A convenient and practical formula to express a data series consisting of N points as a function of their harmonics can be obtained by applying trigonometric relationships to the previous formulae. In particular, the N points data series can be represented exactly by adding together a series of N/2 harmonic functions,

$$\begin{aligned} y_t &= \bar{y} + \sum_{k=1}^{N/2} \left\{ C_k \cos\left[\frac{2\pi kt}{N} - \phi_k\right]\right\} \\ &= \bar{y} + \sum_{k=1}^{N/2} \left\{ A_k \cos\left[\frac{2\pi kt}{N}\right] + B_k \sin\left[\frac{2\pi kt}{N}\right]\right\} \end{aligned} \qquad (5\text{-}5)$$

Where $\bar{y}$ is the mean of the data series, ϕ_k, the phase angle, and the coefficients A_k, B_k and C_k are defined as:

$$\phi_k = \begin{cases} \tan^{-1} B_k/A_k & A_k > 0 \\ \tan^{-1} B_k/A_k \pm \pi & A_k < 0 \\ \pi/2 & A_k = 0 \end{cases} \qquad (5\text{–}6)$$

$$\begin{aligned} A_k &= \frac{2}{N}\sum_{t=1}^{N} y_t \cos\left(\frac{2\pi kt}{N}\right) \\ B_k &= \frac{2}{N}\sum_{t=1}^{n} \sin\left(\frac{2\pi kt}{N}\right) \\ C_k &= \left[A_k^2 + B_k^2\right]^{1/2} \end{aligned} \qquad (5\text{–}7)$$

The cosine wave constituting the $k = 1$ term on the first line of Eq. (5-5) is simply the fundamental, or first harmonic. The other N/2 -1 terms in the summation of Eq. (5-5) are *higher harmonics* with frequencies

$$\omega_k = \frac{2\pi k}{N} \qquad (5\text{-}8)$$

that are integer multiples of the fundamental frequency ω_1.

The second line of Eq. (5-5) suggests the use of a multiple regression to find best fitting harmonics for a given data series y_t. Since the relationships between harmonic predictor variables and the data series y_t do not depend on how other harmonics functions are also being used to represent the series, the proportion of the variance of y_t accounted for by each harmonic is also fixed. When this proportion is expressed as R^2 statistics commonly computed in the regression, the R^2 for the k^{th} is simply

$$R_k^2 = \frac{N/2 * C_k^2}{(N-1) * s_y^2} \qquad (5\text{-}9)$$

The factor s_y^2 is the sample variance of the data series. Since each harmonic provides independent information about the data series, the joint R^2 exhibited by a regression equation with only harmonic predictors is the sum of the R_k^2 values for each harmonic. If all the N/2 possible harmonics are used as predictors, the total R^2 will be exactly 1.

Finally, a consideration about the Fourier line spectrum, or periodogram.

The periodogram is the graphic way to examine the characteristics of a time series that has been Fourier transformed into the frequency domain. In its simplest form, this plot of a spectrum consists of the squared amplitude C_k^2 as a function of the frequency ω_k.. The information contained in the phase angle ϕ_k is not portrayed in the spectrum. Therefore, the spectrum conveys the proportion of variation in the original data series accounted for by oscillations at the harmonic frequencies, but does not supply information about when in time these oscillations are expressed.

The horizontal axis of the line spectrum consists of N/2 frequencies ω_k if N is even, (N – 1)/2 frequencies if N is odd. The smallest of these will be the lowest frequency $\omega_1 = 2\pi/N$ (the fundamental frequency), and this corresponds to the cosine wave that executes a single cycle over the N time points. The highest frequency, $\omega_{N/2}$ is called the Nyquist frequency. It is the frequency of the cosine wave that executes a full cycle over only two time intervals, and that executes N/2 cycles over the full record. The Nyquist frequency depends on the time resolution of the original data series y_t, and imposes an important limitation on the information available from a spectral analysis.

6.2.2 *Analysis of the daily cycle*

The diurnal cycle of cloud patterns during the 10 seasons period is examined in order to infer and to provide basic information regarding periodicities at time scales equal or shorter than one day.

The variable considered for this study was the percentage of pixels with a brightness temperature lower than 241 K. Thus, the diurnally averaged longitude-time plots show the percentage of time that the area averaged brightness temperature met or was lower than 241 K for each longitude and time of the day, averaged from 30 to 54° N.

As noted by Carbone *et al.* (2002), coherent patterns of average frequency in this coordinate system can represent “phase-locked” occurrence of cold cloud tops and thus rainfall. Local phase-locked events would be associated with convection over diurnally heated fixed sources such as mountain chains, which would eventually transform into more global events when propagating along a certain direction and at a preferred speed.

Figure 6-3 shows the average diurnal cycle for the 10 seasons period.

The cycle is repeated twice (one on top of the other) to identify those features that span over more than one day; the scale is in percent and 45% means that a $T_b < 241$ K is detected at that specific longitude-time coordinate ~ 45% of the whole time period.

Note the evident diurnal variations across all longitudes over the continental area, while the diurnal signal is absent in the longitudinal band corresponding to the Atlantic Ocean (15 – 10° W). This is in agreement with the remarks that the most fundamental mechanism for diurnal convection is the destabilisation of the troposphere due to radiative heating and cooling effects, and the response of the marine atmosphere to solar heating is less strong compared to that of the land surfaces (Lieberman *et al.*, 1994).

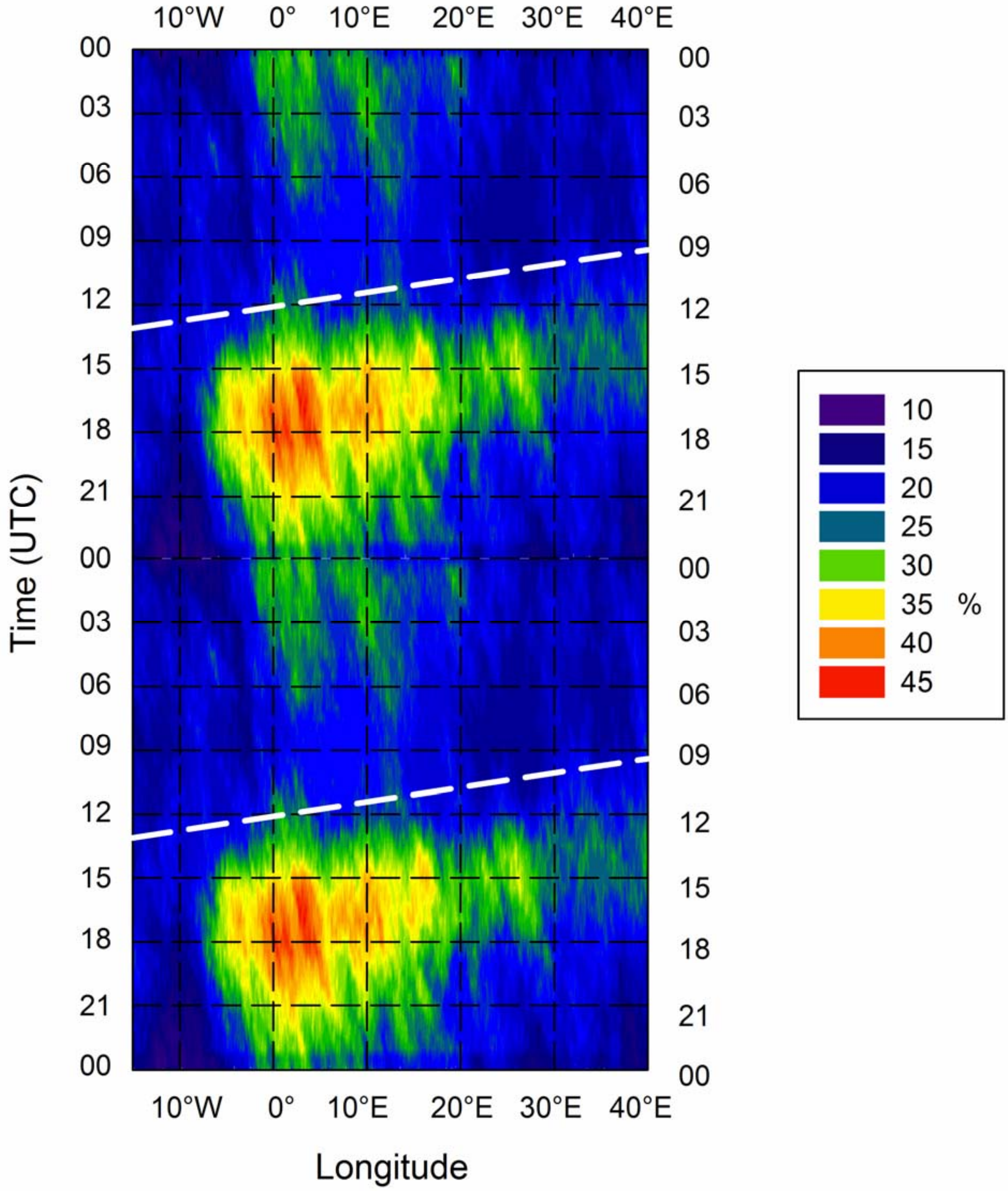

Figure 6-3 *Average diurnal cold cloud ($T_b < 241$ K) frequency Hovmöller diagram for the entire period of record (1996–2005). The diurnal cycle is repeated twice for clarity across the UTC day boundary as in Carbone et al. (2002). The scale corresponds to the percentage of days during which clouds are present at the given longitude–UTC hour coordinate. The local noon is indicated by the dashed lines.*

In Figure 6-3, four maxima were readily identified. The first was located at 7°-10° E, where convection had peak activity near 1700-1800 UTC, and had the lowest frequencies at 0700-0900 UTC. The second frequency centre was near 12°-18° E, where convection occurred most frequently near 1500-1800 UTC, and again the minimum happened in the morning. The third maximum was located in the band 22°-28° E, with the highest percentage around 1400-1600 UTC, and the lowest during the first hours of the day. The forth peak spanned from 33° to 40° E, and reached its maximum values around 1200-1600 UTC.

Note that moving farther to the east, the frequency maxima occurred earlier during the day, in agreement with the different diurnal thermal forcing along the longitudes. Such a configuration, nevertheless, was also linked in part to the eastward propagation of the cloud signals. So that, the maximum near 12°-18° E may be casually related to convection near 7°-10° E in the previous day.

Similar conditions for clouds/rainfall episodes were individuated and discussed by Carbone *et al.* (2002) and Wang *et al.* (2004).

Finally note also a moderate eastward propagation of the frequency maximum from all mountain chains across the domain can be seen.

The average diurnal cycle for each season of the 10 years was analysed to gain more information about the diurnal variability of the convection (see Figures in Appendix B). It is pointed out that the strength of the cycles varies considerably from year to year, being stronger on wetter years (2002, Fig. B-7 Appendix B) and weaker on drier years (2003, Fig. B-8 Appendix B). The diurnal cycles of some years presented maxima in the longitudinal band from 2° W to 5° E that are not evident in other years, because of the smoothing effect of averaging in time.

To evaluate seasonal variations and characteristics of the diurnal cycle, the average diurnal cycle for May, June, July, and August for the years 1996 to 2005 were mapped separately (Fig. 6-4).

Note that the strength of the cycles varies from May to August, being strongest on May 1996-2005 (Fig. 6-4a). In this period the maxima of percentage of cold cloud persistence were higher with respect to the other months and they spanned along a wider longitudinal band, from 5° W to the end of the domain.

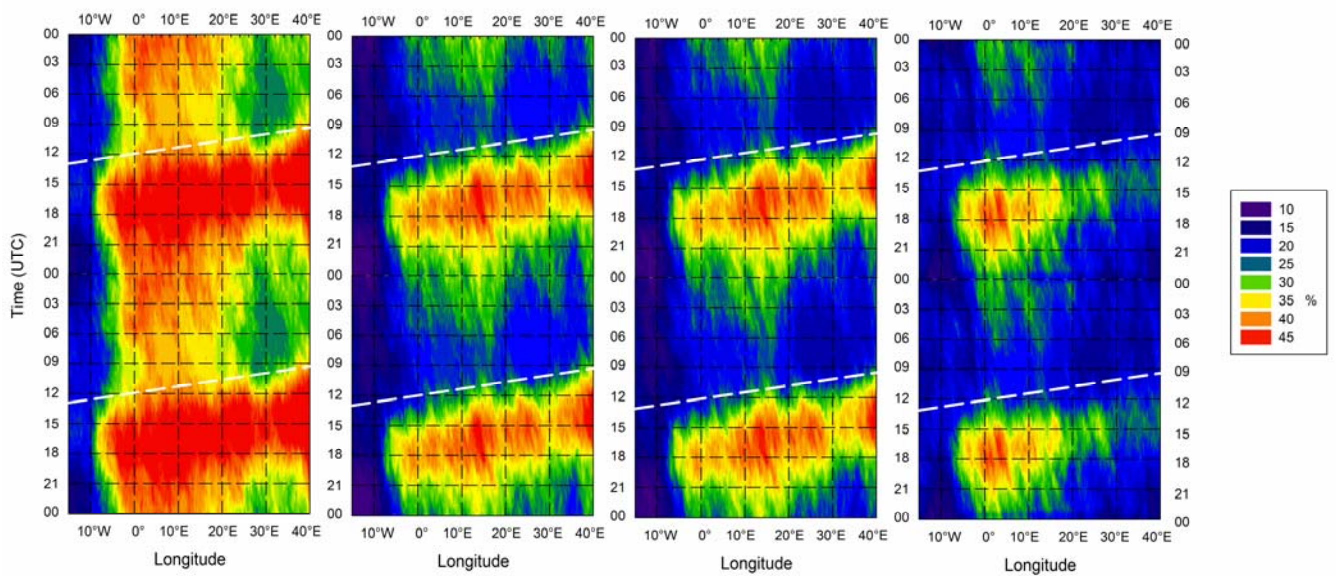

a) **b)** **c)** **d)**

Figure 6-4 *Same as in Fig. 6-3 but for a) all May, b) all June, c) all July, and d) all August of the 1996-2005 period. The local noon is indicated by the dashed lines.*

The daily cycle that characterized the period June 1996-2005 (Fig. 6-4b) presented lower percentages of cold cloud persistence with respect to May, but the longitudinal band interested by significant values remained extended along the longitude domain. Moving farther to the east, the frequency maxima occurred earlier during the day, shifting from 1900 UTC to 1100 UTC.

The average diurnal cycles for July 1996-2005 (Fig. 6-4c) and August 1996-2005 (Fig. 6-4e) were characterized by the lowest percentage values and had an interesting feature: in July the maximum frequency centre was near 22°-27° E, where convection occurred most frequently near 1300-1700 UTC, while in August the maximum was located at 2° W-5° E, with the peak around 1500-1900 UTC. Therefore, in these periods the more cloudy regions were localized in opposite areas of the domain.

The eastward propagation of cloud patterns (including both frequency maxima and minima) is maximum in May and still evident in June and July. The propagation remains confined to the western part of the continental domain, the Pyrenees and Western Alps, in August while it completely disappears together with the diurnal cycle in the eastern sector.

6.2.3 Fourier decompositions

The analysis of the average diurnal cycles allows for identifying five longitudinal bands characterized by a significant signal of cold cloud persistence. These bands are located in correspondence with the most relevant mountain chains or along the Atlantic coasts and are:

- 2° W – 5° E, the Pyrenees and Atlantic Coasts
- 7° -10° E, the Western Alps
- 10° - 18° E, the Eastern Alps
- 22° - 28° E, the Carpathian
- 33° - 40° E, the Anatolian Plateau and the Black Sea.

The signal obtained by the mean diurnal cycle of percentage of IR cloud-top brightness temperature lower than 241 K for each longitudinal band was subjected to Fourier decomposition and the wave numbers 0-2 were considered. This analysis regards the signals relative to the average of the warm seasons of all 10 years and those regarding May, June, July and August 1996-2005.

Figures 6-5 to 6-9 present the results of the decomposition.

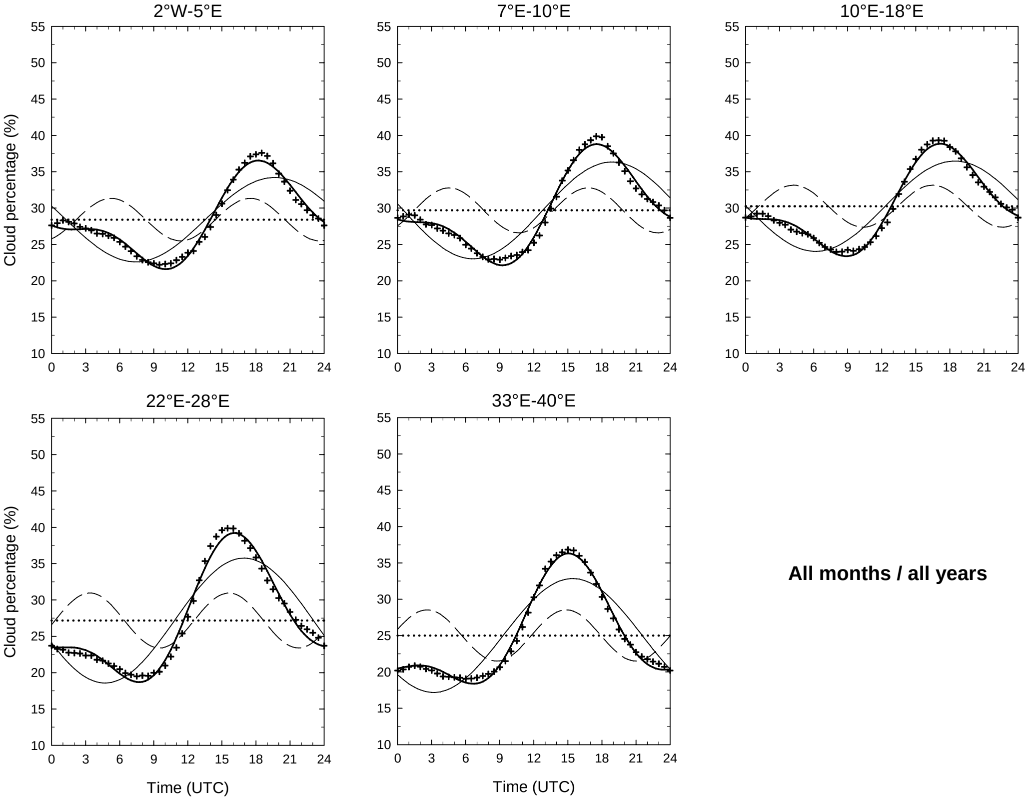

Figure 6-5 *Fourier decomposition (wave numbers 0-2) of mean diurnal cycle 1996-2005 of percentage of IR cloud-top brightness temperature < 241 K for the five analysedlongitudinal bands. Dotted, thin solid, dashed and thick solid are wave number0, 1, 2 and their sum, respectively. Crosses represent the original data before decomposition.*

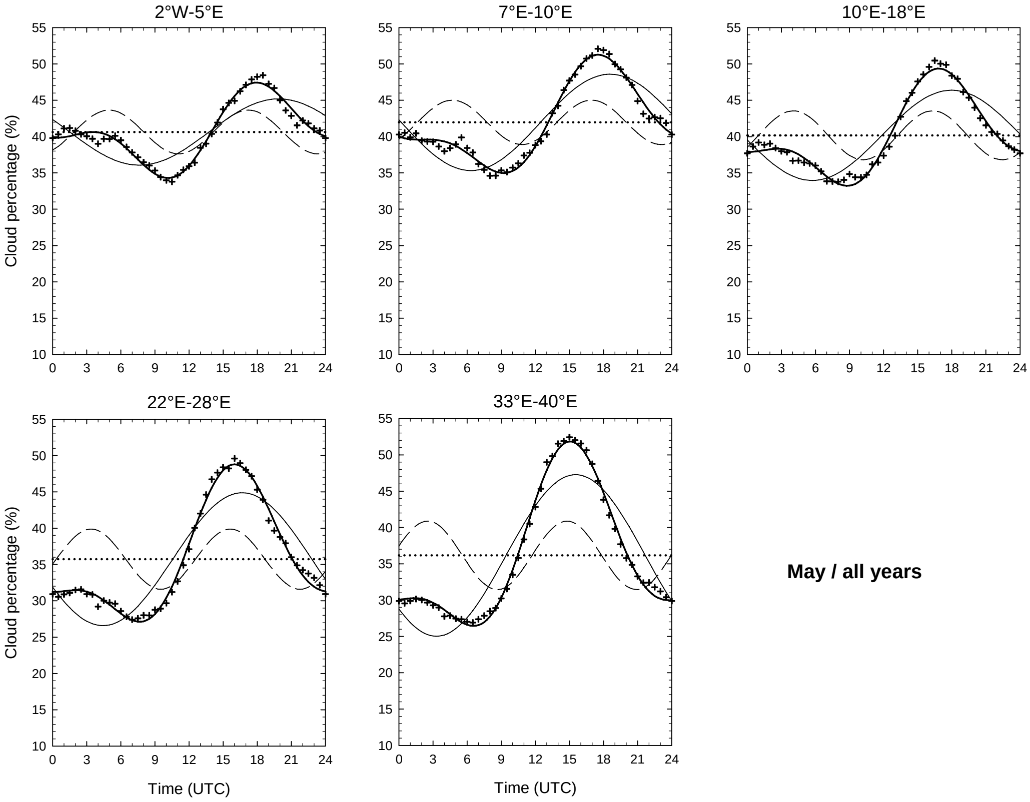

Figure 6-6 *Same as in Figure 6-5 but for the period May 1996-2005.*

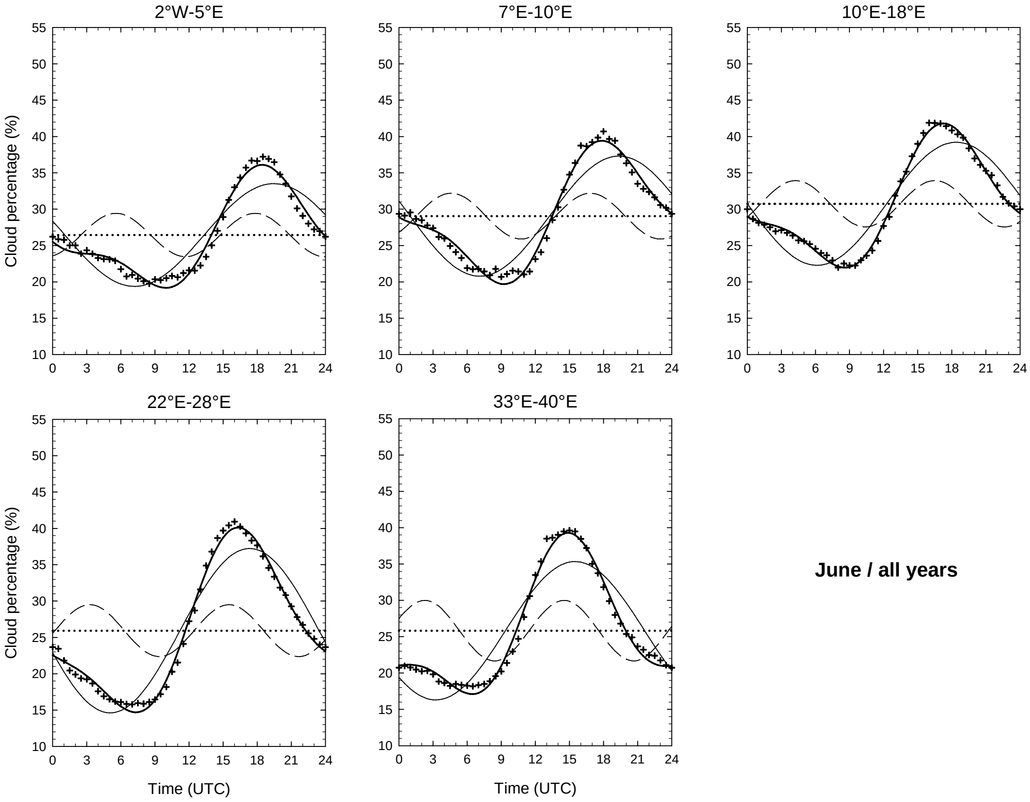

Figure 6-7 *Same as in Figure 6-5 but for the period June 1996-2005.*

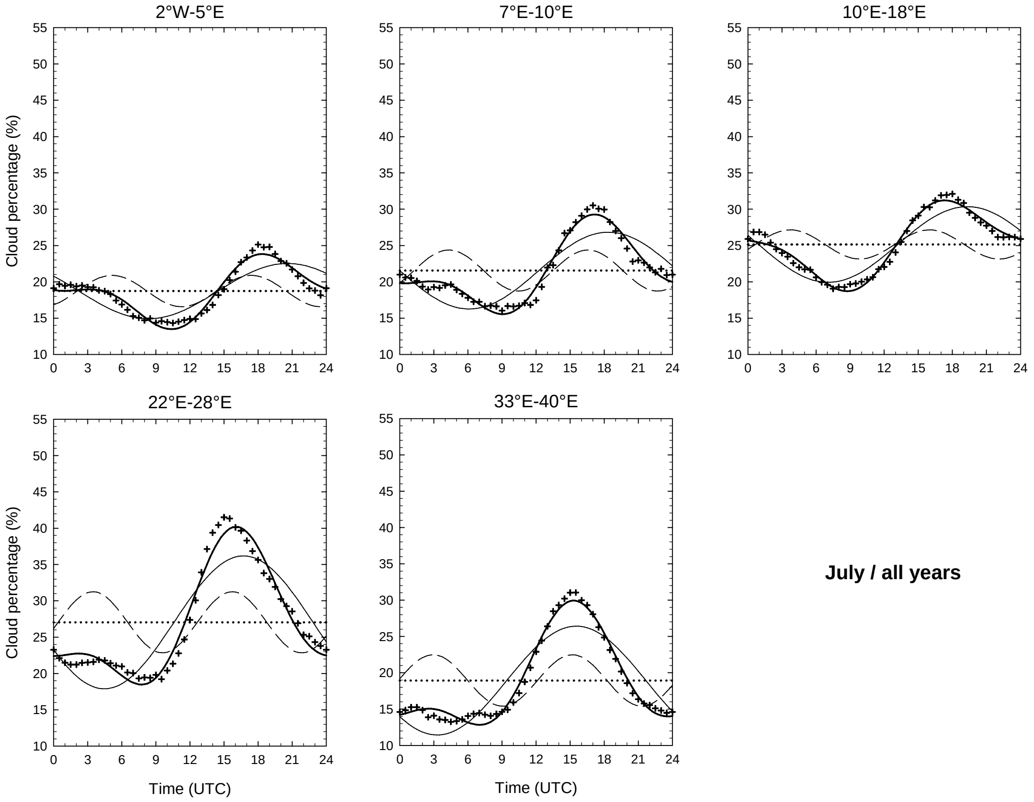

Figure 6-8 *Same as in Figure 6-5 but for the period July 1996-2005.*

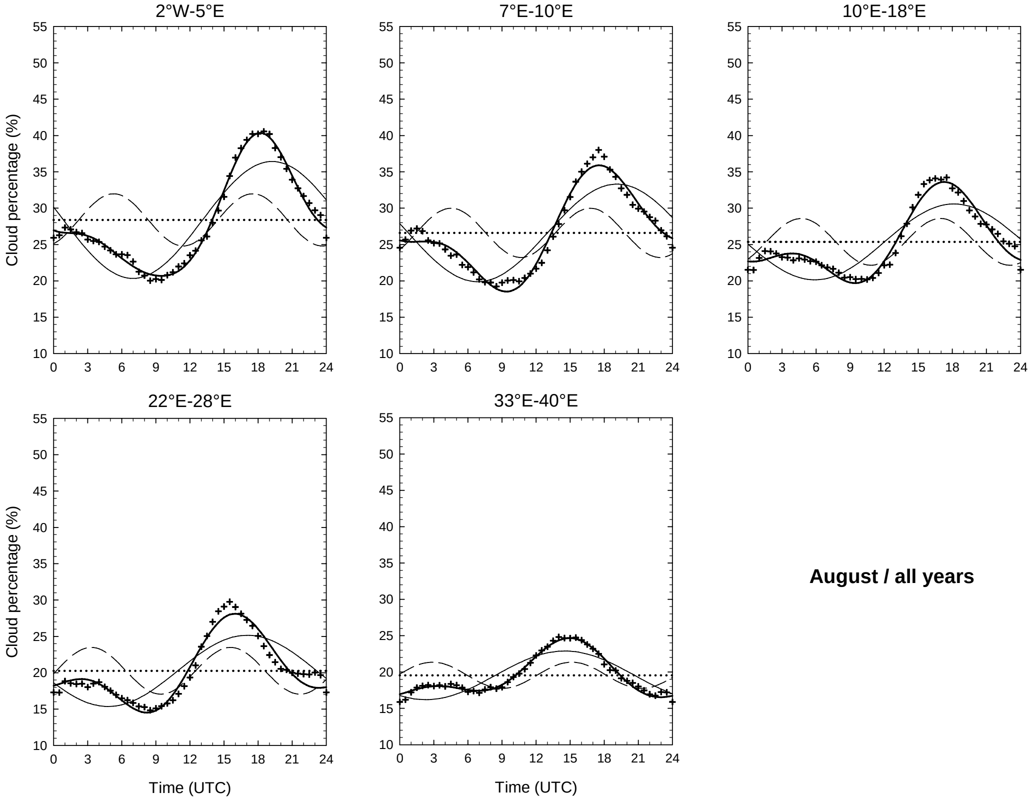

Figure 6-9 *Same as in Figure 6-5 but for the period August 1996-2005.*

The Fourier decomposition of the diurnal cycle for the overall 40-month data period (Fig. 6-5), averaged over the five longitudinal bands shows that the diurnal components of the signals were stronger in the eastern bands. The maxima of the diurnal components happened earlier during the day as we move from west to east. They occurred from 2000 UTC in the band 2° W-5° E to 1500 UTC in the band 33° - 40° E.

On average, waves 1 and 2 together explained 98.8 % of the total variance of all the warm season mean signal, and the summations of waves 0 to 2 were very similar to original data (crosses), so that high frequency harmonics can be considered as not very relevant.

When the seasonal diurnal cycles are considered and averaged along the five longitudinal bands, the Fourier decompositions (Fig. 6-6 to 6-9) evidence that waves 1 and 2 accounted for a smaller percentage of the total variance, with respect to the all season bands signals. In particular, for the periods May, June, July, and August 1996-2005, the mean percentage of the total variance explained by the first two harmonics are 98.0 %, 98.2%, 96.8 %, and 96.6 %, respectively. The superimposition of original data and the summations of waves 0 to 2 show some discrepancies between these two signals.

Moving from the western to the eastern band of the domain, the shifts earlier in time of the maxima of the diurnal signal were evident also in the seasonal Fourier decompositions.

Apart from the mean diurnal cycle of August 1996-2005, the diurnal cycles had larger amplitude in the easternmost bands.

The decomposition of signal relative to July 1996-2005 shows that the diurnal component had a greater amplitude along the three bands 10° - 18° E, 22° - 28° E, and 33° - 40° E.

The same analysis applied to the August 1996-2005 signal shows that the amplitude of the diurnal components are grater for the two western bands, i.e. 2° W – 5° E and 7° - 10° E.

6.2.4 Periodicity and harmonic analysis at longer periods

As an effort to better understand the periodicity of convection, the averaged power spectrum obtained applying the DFT analysis to the time series of the fraction of brightness temperature lower than 241 K in the Hovmöller space from 15 ° W to 40 ° E for the 10 warm seasons of the data period was examined. The result is presented in Fig. 6-10. The spectrum was plotted as a function of longitude and logarithm of periods and allowed for examination of activities at wavelengths up to 30 days.

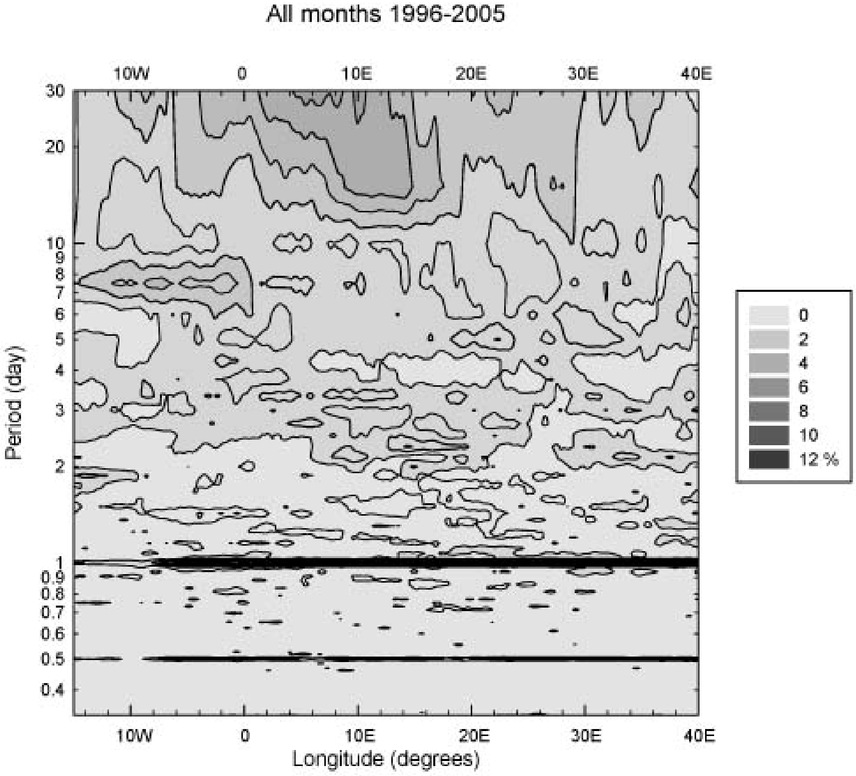

Figure 6-10 *Distribution of the mean power spectrum of time series of fraction of IR brightness temperature lower than 241 K in the Hovmöller space along each longitude from 15° W to 40° E (at 0.05° interval), plotted as a function of logarithm of period (day) and longitude (degree). The period analysed includes the 10 warm seasons 1996-2005 .*

In agreement with the daily cycle discussion, the diurnal signal was more evident over the continent than over the ocean. It becomes more clear East of 10° E.

Figure 6-11 shows the diurnal and semidiurnal components of the power spectrum plotted against the mountain ranges of the domain. While the maxima of the diurnal are well in phase with the presence of elevated terrain and generally with land masses, the interpretation of the result is not quite as direct as is in the North America (Carbone *et al.*, 2002). In other words, the very complex European orography does not lend itself to a straightforward identification of maxima and minima associated with north-to-south mountain chains and plains, respectively, as in the case of North America.

The presence of a clear semidiurnal signal in the spectrum needs to be commented. Semidiurnal signals in the continental precipitation patterns in summer have been identified also over the U.S. and Asia, but their physical forcing is debatable. Semidiurnal forcing of precipitation has long been associated with atmospheric tidal lifting. However, considering the similarity of diurnal and semidiurnal geographic variations emerged from this analysis, it is quite clear that in our case the semidiurnal signal is a computational effect due to DFT analysis. Also Carbone *et al.* (2003)

disagreed with the tidal interpretation of the semidiurnal signals for North America and explained it as an effect of calculation.

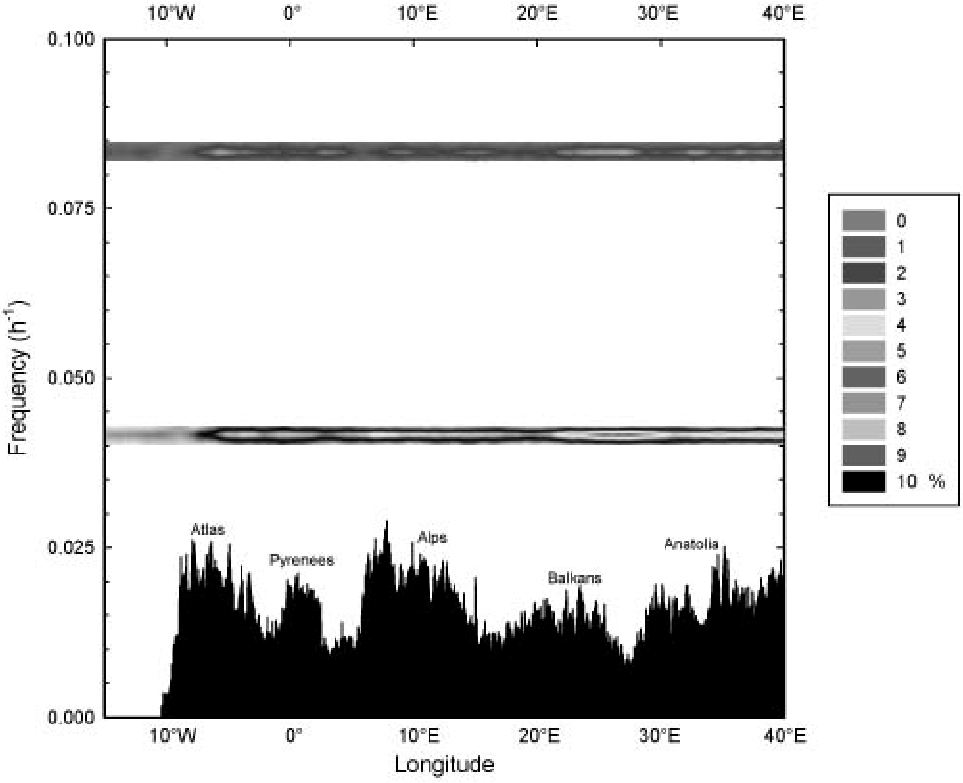

Figure 6-11 *Power spectrum vs. longitude and orography of the domain from 15° W to 40° E.*

The power spectrum (Fig. 6-10) shows that the signals peaked, at different periods, in precise longitudinal bands. In particular, activities at synoptic scales (periods roughly from 6 to 10 days) characterized the longitudes from 15° W to 0°. This is consistent with the periodicity of cloud systems arriving from the Atlantic Ocean.

Longer period activities (from 15 up to 30 days) were stronger around 10° W and from 5° W to 15° E.

Activities with period of about 30 days could be related to the Madden Julian Oscillation (Madden and Julian 1971, 1994), a tropical intra-seasonal oscillation that may affect mid-latitude weather too.

In order to examine which components of the signal associated to the fraction of IR brightness temperature lower than 241 K dominated during the different months of the warm season, mean power spectra of that signal for the periods May, June, July and August 1996-2005 were analysed (Fig. 6-12 to 6-15).

It is worth noting the different width of the longitudinal band characterised by the dominance of the diurnal components from May 1996-2005 to August 1996-2005.

With respect to July 1996-2005 and August 1996-2005, May 1996-2005 and June 1996-2005 presented a larger longitudinal area in which the diurnal component had a peak. Moreover, June 1996-2005 presented a quasi continue band starting from East of 10° W, while in the other periods the diurnal peaking area was more discontinuous. August 1996-2005 had the narrower band with a clear diurnal signal, from 12° W to 12° E.

The analysis of the seasonal variations of activities at longer periods evidences that synoptic scale phenomena (from 5 to 10 days) interested in particular the longitudes from 0° to 18° E in May, from 10° W to 10° E and from 18° to 40° E in June, from 15° W to 20° E in July and August.

Other interesting components of the power spectra were longer periods (from 15 to 30 days) activities in the band 2° - 20° E, 15° W – 26° E, 12° W – 28° E, and 15°W- 4° E together with 20° - 34° E, during May, June, July and August, respectively. The mean power spectrum of August 1996-2005 presented a peak roughly between 4° W and 8° E that corresponds to activities at three days period.

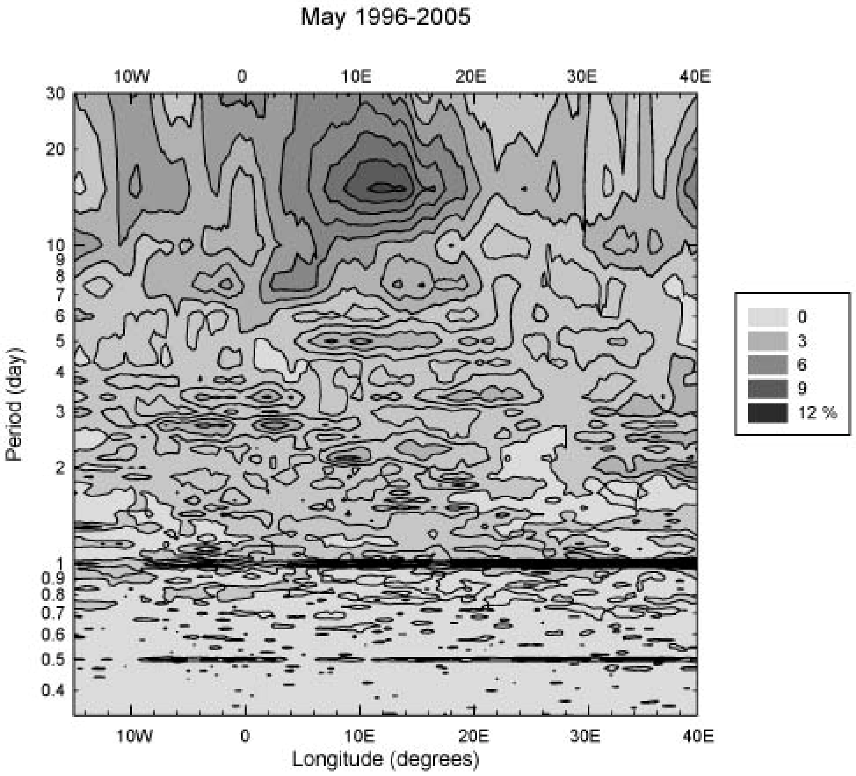

Figure 6-12 *Same as in Figure 6-10 but for the period May 1996-2005 .*

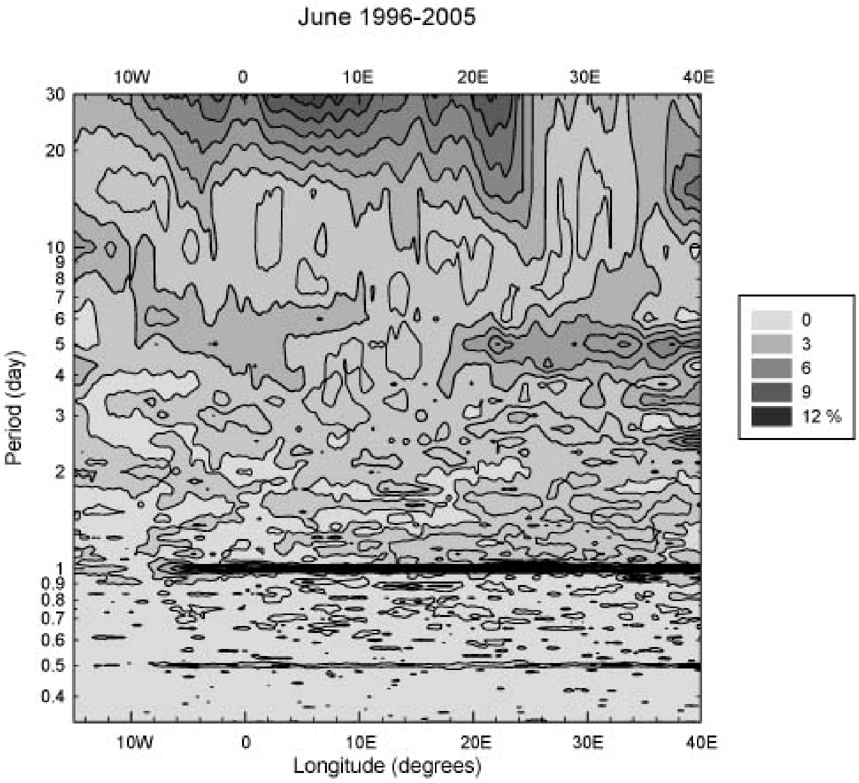

Figure 6-13 *Same as in Figure6-10 but for the period June 1996-2000.*

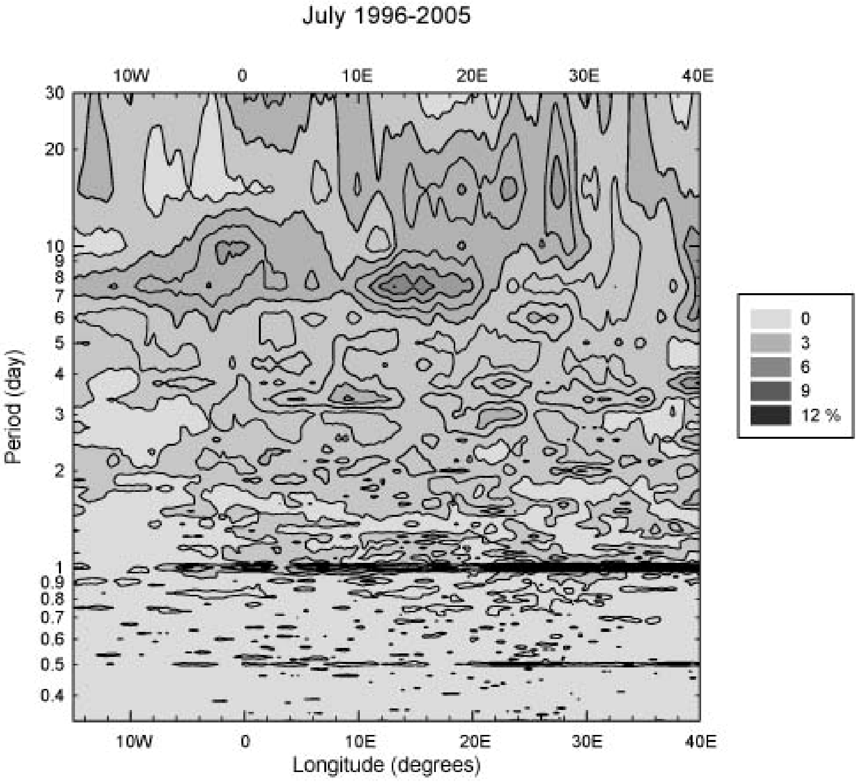

Figure 6-14 *Same as in Figure 6-10 but for the period July 1996-2005.*

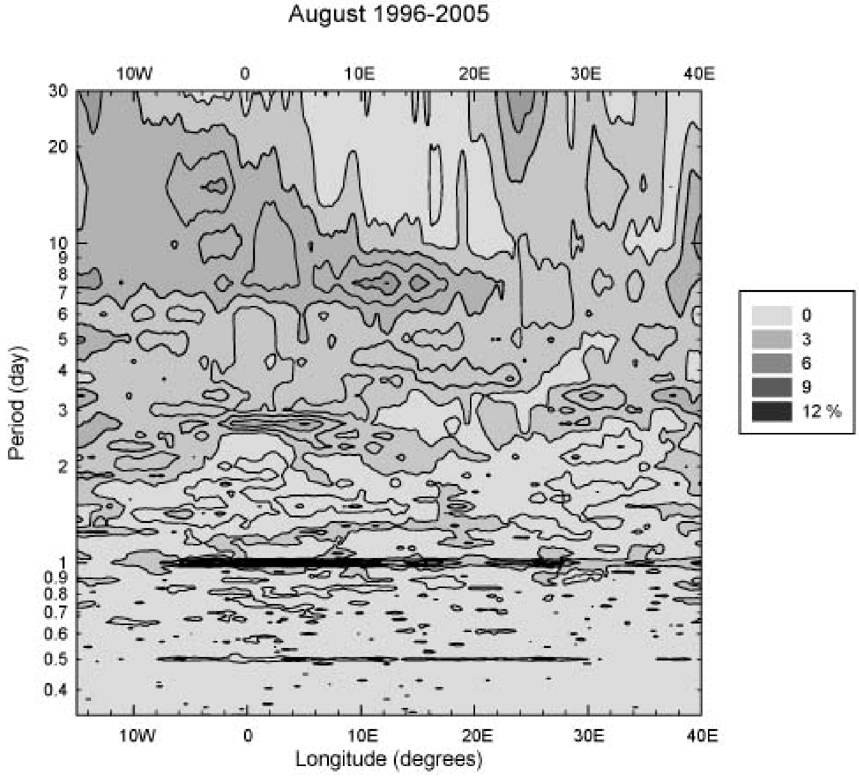

Figure 6-15 *Same as in Figure 6-10 but for the period August 1996-2005.*

The same five longitudinal bands previously analysed for the diurnal cycle, were considered for a further examination of the general characteristics of the periodicity of the cold cloud percentage signal at longer periods.

Figure 6-16 presents the power spectra of cloud percentage with brightness temperature lower than 241 K at the five longitudinal bands of 2°W-5°E, 7°-10°E, 10°-18°E, 22°-28°E, and 33°-40°E averaged through the 10 warm seasons.

Figures 6-17 to 6-20 show the same analysis but for the 10-months periods.

The power spectra relative to the overall 10 warm seasons data period (Fig. 6-16) reveal that the diurnal ($n = 30$[1]) signal had the largest amplitude than waves at any other wavelength in each band. In the three weastermost channels, activity at lower frequency (between $n = 1$ and $n = 14$) were significant.

---

[1] The formula applied to obtain the period associated to the wavenumber n is: Total period/n = 1 / frequency of this wave = period of this wave.
E.g. for $n = 30$, considering the total period of 30 days: 30 days / 30 = 1 / day

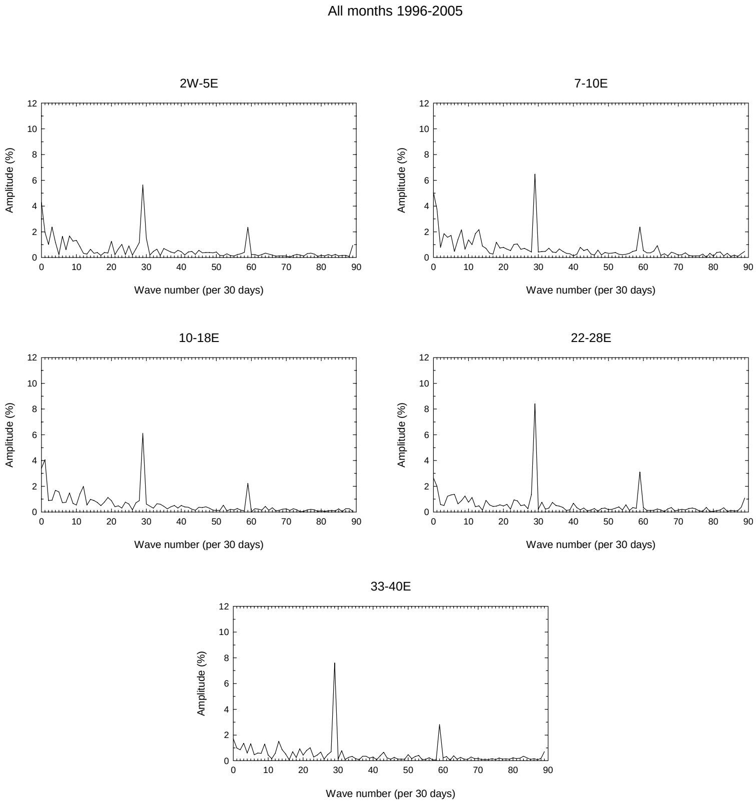

Figure 6-16 *Mean power spectrum of time series of fraction of IR brightness temperature lower than 241 K (%) averaged over the five longitudinal bands 2°W-5°E, 7°-10°E, 10°-18°E, 22°-28°E, and 33°-40°E for 1996-2005..*

The power spectra relative to May, June, July, and August 1996-2005 (Fig. 6-17 to 6-20) lend themselves to an evaluation of the seasonal variability of each channel signals.

The longitudinal band ranging from 2° W to 5° E, characterised by the presence of the Atlantic Coasts and the Pyrenees, had a power spectrum dominated by activities at low frequencies (from $n = 1$ to $n = 11$) during May, June, and July, while in August the greater amplitude corresponded to the diurnal signal, indicating a pronounced solar heating.

The second longitudinal band analysed ranges from 7° to 10° E and includes the western Alps. Its power spectra show that the diurnal component had a large amplitude during all the four periods analysed, but only in August it was the most important component of the spectra. Activities at frequency of 1/30 days and 1/15 days dominated during May and June, while in July the component correspondent to $n = 9$ had the highest amplitude, even if its values was very similar to the diurnal one.

At 10° - 18° E, the diurnal signal had the largest amplitude than waves at any other wavelength only in June. The dominant components of the power spectra in May and July corresponded to $n = 2$ and $n = 4$, respectively. In other words, phenomena with periods of 15 days and 7.5 days dominated. In August the component associated to $n = 4$ had the greatest amplitude in the spectrum. In general this band, in which the Eastern Alps are located, presented significant activities at low frequencies, associated to values of n from 1 to 10, during all the warm season.

In the fourth band, from 22° to 28° E, the longitudinal band of the Balkans, the power spectra reveal that the diurnal was the most important component of the spectra during all months of the warm season. Its amplitude was maximum in June and July, and reached its minimum value in August, but remaining the dominant wave of the signal. Components at lower frequencies ($n = 1$ to 10) were most evident in June and July, but May and August spectra show that waves associated to $n = 1$ and $n = 2$, typical of phenomena that reoccur every 30 and 15 days, were also important during those periods.

The last band, ranging from 33° to 40° E, had power spectra clearly dominated by the diurnal component during the first three months of the warm season. It is interesting to note that among other wavelengths, waves with $n = 1$ to 15 were important in May and June. In June a peak of the wave with period of 5 days ($n = 6$) was clearly evident. The power spectrum of August for this band presents maxima associated with waves with $n = 1$ to 10 and $n = 30$ (diurnal cycle), but their amplitudes are generally lower with respect to the other months.

Note that in the two easternmost longitudinal band (22° - 28° E and 33° - 40° E) the diurnal signal dominated the power spectra during all months of the warm season and starts to decrease in August. June and August were the two months during which the diurnal cycle was the most significant component of the spectra in the two more western band (2° W - 5° E and 7° - 10° E). The diurnal signal was the prevailing spectral component in the central band only in June. Finally, activities at lower frequencies were more significant with respect to the other waves, in the first three bands, analysed during May and July.

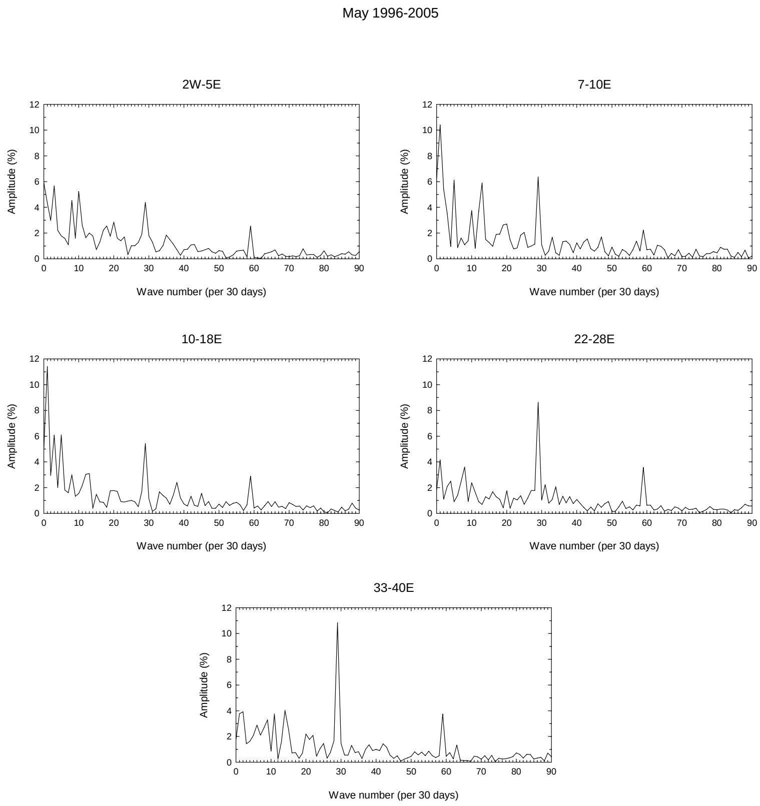

Figure 6-17 *Same as in Figure 6-16 but for the period May 1996-2005.*

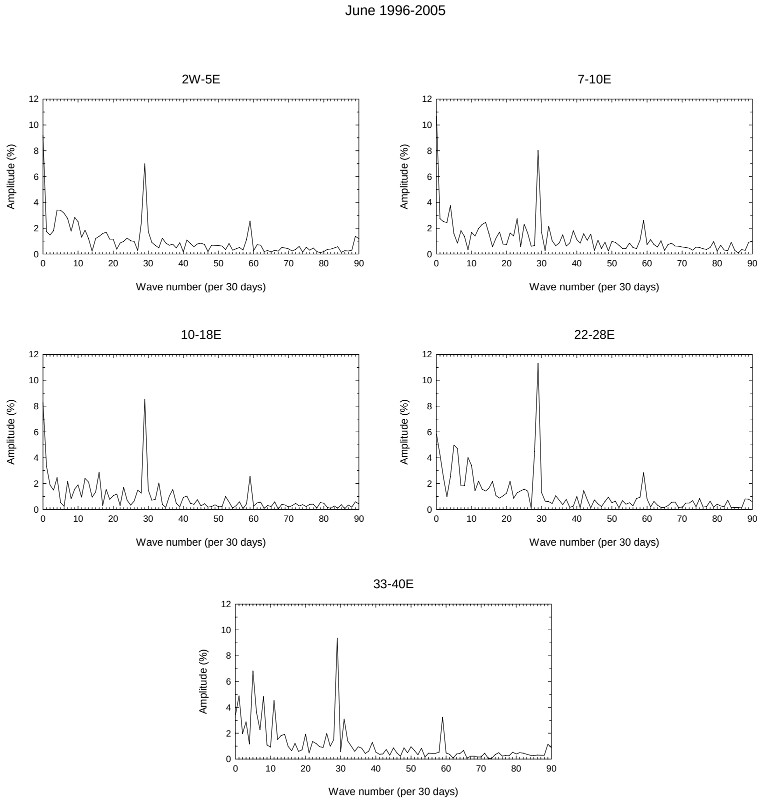

Figure 6-18 *Same as in Fig. 6-16 but for the period June 1996-2005.*

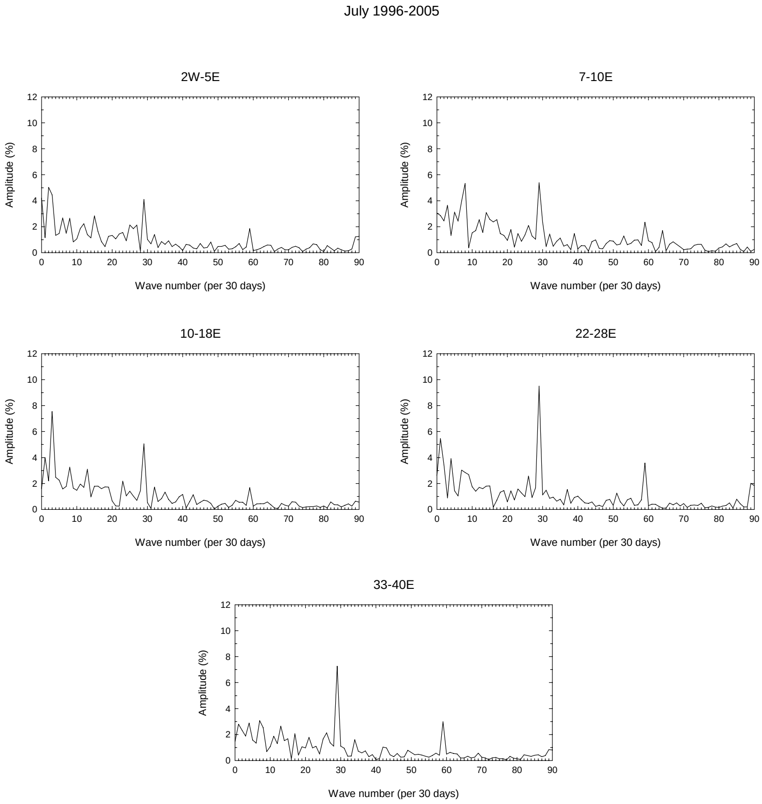

Figure 6-19 *Same as in Fig. 6-16 but for the period July 1996-2005.*

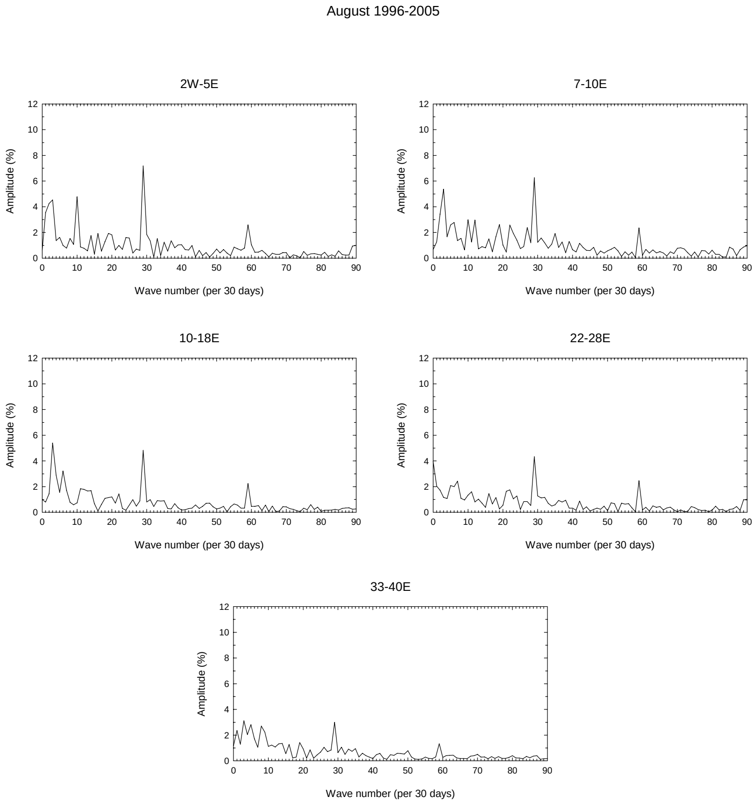

Figure 6-20 *Same as in Fig. 6-16 but for the period August 1996-2005.*

7. Conclusions

Meteosat MVIRI IR T_bs in the 10.5 – 12.5 μm spectral band were used over Europe and the Mediterranean to investigate the regional and intraseasonal variability of cold cloud episodes during late spring and summer months. The period studied is May-August 1996-2005.

In this study, cold cloud (cloud tops < 241 K) were considered correlated to precipitation even tough there are limitations due to cirrus contamination and to the not always one-to-one link between cloud top structure and precipitation at the ground. However, the absence of ground radar networks covering the area of study that could have supplied a more direct dataset of rainfall rates and the findings of other authors (e.g. Wang et al., 2004) using IR T_bs data justify the use of IR T_bs for this kind of climatological study.

The 241 K T_b threshold was identified after a sensitivity study carried out over the domain during the10-year period.

The latitude-longitude domain under scrutiny spans from 30 to 54°N and from 15°W to 45°E. The zonal component of motion of the cold cloud systems was examined by dividing the area into 1100 vertical strips of 0.05° width (~ 4 km) spanning from 30 to 54°N in the N-S direction.

The quantitative analysis was based on the application of a two-dimensional autocorrelation function to the T_b data in the Hovmöller longitude-time space.

Using the autocorrelation function, the convective events were quantified as to their coherency, duration, span and propagation speed. The statistical analysis of these dynamic properties was taken into account to evaluate could cloud systems characteristics.

Harmonic analysis using DFTs was used as an analysis tool together with diurnal cycle investigations in order to study the periodicity of the signal associated to cold cloud systems.

The major findings of this study can be outlined as follows.

The propagation of cold cloud systems is essentially zonal in nature as it is to be expected for the European region dominated by the westerlies. The meridional component is very weak and generally confined to relative narrow latitude belts as found by other authors.

The analysis of the persistence of cold clouds over the area evidences a role played by mountain chains in initiating convection. In particular, the Pyrenees and the Alps are significant in May and part of June; the Balkans and Anatolia play also a role in May, but their contribution is less evident. In July cold clouds are confined more over Eastern Europe with a moderate clustering in the eastern wake of the Alps. The activity reaches a minimum in August, when the local influence of the Pyrenees and the Alps starts again to have a role.

A diurnal oscillation is found across the analysis domain with a maximum marking the initiation of convection in the lee of the mountains and shifting from about 1400 UTC at 40°E to 1800 UTC at 0°. The amplitude of the diurnal cycle is more or less homogeneous across the 5°W-40°E longitude domain. There is a moderate eastward propagation of the frequency maximum from all mountain chains across the domain and the diurnal maxima are completely suppressed west of 5°W.

The eastward propagation of cloud patterns, that regards both frequency maxima and minima, is maximum in May and remains evident in June and July.

One dimensional DFT analysis shows a clear signal correspondent to the period of one day which characterise all Europe while it disappears west of 10°W, that is over the Ocean.

Local maxima peaked roughly between 6 and 10 days characterized the longitudes from 15° W to 0° and indicate the activity of the westerlies with frontal passage over the continent.

Longer periods activities (from 15 up to 30 days) were stronger around 10° W and from 5° W to 15° E and are likely related to the Madden Julian Oscillation influence.

The maxima of the diurnal signal are well in phase with the presence of elevated terrain and generally with land masses, but the complexity of European orography makes the result difficult to be interpreted.

A much weaker semidiurnal signal is found over the same longitudinal band over the continent. The interpretation of this signal is somewhat not straightforward.

The harmonic decomposition of the signal shows that there is a general tendency to increase the diurnal amplitude from west to east while the diurnal signal peak shifts earlier in the day from west to east (roughly from 2000 UTC to 1600 UTC).

The analysis of the longer and longer lasting events (i.e., span $\geq$ 1000 km and duration $\geq$ 20 h) shows that their median zonal phase speed is 16.1 ms^{-1} in agreement with the result obtained over East Asia and Australia with an analogous satellite-based study method.

The findings of the present thesis represent an essential contribution to a scientific paper on a major journal by Levizzani et al. (2010).

8. References

Ahijevych, D. A., R. E. Carbone, J. D. Tuttle, and S. B. Trier, 2001: Radar data and climatological statistics associated with warm season precipitation episodes over the Continental U.S. *NCAR Tech. Note TN-448+STR*, Boulder, CO, 81 pp.

Alpert, P., B. U. Neeman, and Y. Say-El, 1990a: Climatological analysis of Mediterranean cyclones using ECMWF data. *Tellus.*, **42A**, 65-77.

Alpert, P., B. U. Neeman, and Y. Say-El, 1990b: Intermonthly variability of cyclone tracks in the Mediterranean. *J. Climate*, **3**, 1474-1478.

Anderson, C., and R. Arritt, 1998: Mesoscale convective complexes and persistent elongated convective systems over the United States during 1992 and 1993. *Mon. Wea. Rev.*, **126**, 578-599.

Arkin, P. A., and P. Xie, 1994: The Global Precipitation Climatology Project: First algorithm intercomparison project. *Bull. Amer. Meteor. Soc.*, **85**, 401-419.

Augustine, J. A., and F. Caracena, 1994: Lower-tropospheric precursors to nocturnal MCS development over the Central United States. *Wea. Forecasting*, **9**, 116-135.

Carbone, R. E., J. D. Tuttle, and D. Ahijevych, 2003: Fact and fiction: semidiurnal forcing of convective rainfall. *Bull. Amer. Meteor. Soc.*, **11,** 1511-1512.

Carbone, R. E., J. D. Tuttle, D. Ahijevych, and S. B. Trier, 2002: Inferences of predictability associated with warm season precipitation episodes. *J. Atmos. Sci.*, **59,** 2033-2056.

Carbone, R. E., J. W. Conway, N. A. Crook, and M. W. Moncrieff, 1990: The generation and propagation of a nocturnal squall line. Part I: Observations and implications for mesoscale predictability. *Mon. Wea. Rev.*, **118,** 26-49.

Carbone, R. E., J. D. Tuttle, W. A. Cooper, V. Grubisc, and W-C Lee, 1998: Tradewind rainfall near the windward coast of Hawaii. *Mon. Wea. Rev.*, **126,** 2847-2863.

Chaboureau, J. P., and C. Claud, 2003: Observed variability of North Atlantic Ocean precipitating systems during winter. *J. Geophys. Res.*, **108 (D14),** 4435, doi: 10.1029/2002JD003343.

Chaboureau, J. P., and C. Claud, 2006: Satellite-based climatology of Mediterranean cloud systems and their association with large scale circulation. *J. Geophys. Res.*, **111 (D1),** D01102, doi: 10.1029/2005JD006460.

Crook, N. A., R. E. Carbone, M. W. Moncrieff, and J. W. Conway, 1990: The generation and propagation of a nocturnal squall line. Part II: Numerical simulation. *Mon. Wea. Rev.*, **118,** 50-65.

Doneaud, A. A., S. Ionescu-Niscov, D. L. Priegnitz, and P. L. Smith, 1984: The area-time integrals an indicator for convective rain volumes. *J. Climate Appl. Meteor.*, **23**, 555-561.

Davis, R.E., D. A. Ahijevych, and S. B. Trier, 2002: Detection and prediction of warm season midtropospheric vortices by Rapid Update Cycle. *Mon. Wea. Rev.*, **130**, 24-42.

Davis, R. E., B. P. Hayden, D. A. Gay, W. L. Phillips, and G.V. Jones, 1997: The North Atlantic subtropical anticyclone. *J. Climate*, **10**, 728-744.

Davis, R. E., K. W. Manning, R. E. Carbone, S. B. Trier, and J. D. Tuttle, 2003: Coherence of warm season continental rainfall in numerical weather prediction models. *Mon. Wea. Rev.*, **131**, 2667-2679.

Fritsch, J. M., and R. E. Carbone, 2004: Improving quantitative precipitation forecasts in the warm season. A USWRP research and development strategy. *Bull. Amer. Meteor. Soc.*, **85**, 955-965.

Fritsch, J. M., R. J. Kane, and C. H. Chelius, 1986: The contribution of mesoscale convective weather systems to the warm season precipitation in the United States. *J. Climate. Appl. Meteor.*, **25**, 1333-1345.

Fritsch, J. M., R. A. Houze Jr., R. Adler, H. Bluestein, L. Bosart, J. Brown, F. Carr, C. Davis, R. H. Johnson, N. Junker, Y.-H. Kuo, S. Rutledge, J. Smith, Z. Toth, J. W. Wilson, E. Zipser, and D. Zrnic, 1998: Quantitative precipitation forecasting: Report of the Eighth Prospectus Development Team, U.S. Weather Research Program. *Bull. Amer. Meteor. Soc.*, **79**, 285-299.

Griffith, C. G., W. L. Woodley, P. G. Gruber, D. W. Martin, J. Stout, and D. N. Sikdar, 1978: Rain estimation from geosynchronous satellite imagery visible and infrared studies. *Mon. Wea. Rev.*, **106**, 1152-1171.

Hernandez, E., L. Canal, J. Diaz, R. Garcia, and L. Gimeno, 1998: Mesoscale Convective Complexes over the Western Mediterranean area during 1990-1994. *Meteorol. Atmos. Phys.*, **68**, 1-12.

Keenan, T. D., and R E Carbone, 2008: Propagation and diurnal evolution of warm season cloudiness in the Australian and maritime continent region. *Mon. Wea. Rev.*, **136**, 973-994.

Kidder, S. Q., and T. H. Vonder Haar, 1995: *Satellite meteorology An introduction*. Academic Press**,** 466 pp.

Knupp, K. R., B. Geerts, and J. D. Tuttle, 1998: Analysis of a small vigorous mesoscale convective system. Part II: Evolution of the stratiform precipitation and mesoscale flows. *Mon. Wea. Rev.*, **126**, 1837-1858.

Koch, S. E., and C. O'Handley, 1997: Operational forecasting and detection of mesoscale gravity waves. *Wea. Forecasting*, **12**, 253-281.

Laing, A. G., and J. M. Fritsch, 1997: The global population of mesoscale convective complexes. *Quart. J. Roy. Meteor. Soc.*, **123**, 389-405.

Laing, A. G., and J. M. Fritsch, 2000: The large-scale environments of the global populations of mesoscale convective complexes. *Mon. Wea. Rev.*, **128**, 2756-2776.

Laing, A. G., R. E. Carbone, V. Levizzani, and J. D. Tuttle, 2008: The propagation and diurnal cycle of deep convection in northern tropical Africa. *Quart. J. Roy. Meteor. Soc.*, **134**, 93-109.

Levizzani, V., R. Ginnetti, A. G. Laing, and R. E. Carbone, 2006: Warm season precipitation climatology: First European results. *Adv. Geosci.*, **7**, 15-18.

Levizzani, V., F. Pinelli, M. Pasqui, S. Melani, A. G. Laing, R. E. Carbone, 2010: A 10-year climatology of warm season cloud patterns over Europe and the Mediterranean from Meteosat IR observation. In press on *Atmos. Res.*

Lieberman, R. S., B. A. Boville, and B. P. Briegleb, 1994: Diurnal heating and cloudiness in the NCAR community climate model (CCM2). *J. Climate*, **7**, 869-889.

Liu, C., M. W. Moncrieff, and J. D. Tuttle, 2008: A note on propagating rainfall episodes over the Bay of Bengal. *Quart. J. Roy. Meteor. Soc.*, **134**, 787-792.

Lopez, R. E., J. Thomas, D. O. Blanchard, and R. L. Holle, 1983: Estimation of rainfall over extended region using only measurements of the area covered by radar echoes. *Prepr. 21st Conf. Radar Meteor.*, American Meteorological Society, Boston, pp. 681-686.

Lovejoy, S., and G. L. Austin, 1979: The source of error in rain amount estimating scheme for GOES visible and IR satellite data. *Mon. Wea. Rev.*, **107**, 1048-1054.

Madden, R. A., and P. R. Julian, 1971: Description of a 40-50 day oscillation in the zonal wind in the tropical Pacific. *J. Atmos. Sci.,* **28,** 702-708.

Madden, R. A., and P. R. Julian, 1994: Observations of the 40-50 Day Tropical Oscillation – A Review. *Mon. Wea. Rev.,* **122,** 814-837.

Maddox, R. A., 1980: Mesoscale convective complexes. *Bull. Amer. Meteor. Soc.,* **61,** 1374-1387.

Maddox, R. A., L. R. Hoxit, and C. F. Chappel, 1979: Synoptic and meso-scale aspects of flash floods events. *Bull. Amer. Meteor. Soc.,* **60,** 115-123.

Morel, C., and S. Senesi, 2002: A climatology of mesoscale convective systems over Europe using satellite infrared imagery. II: Characteristics of European mesoscale convective systems. *Quart. J. Roy. Meteor. Soc.*, **128**, 1973-1995.

Olson, D. A., N. W. Junker, and B. Korty, 1995: Evaluation of 33 years of quantitative precipitation forecasting at the NMC. *Wea. Forecasting*, **10,** 498-511.

Schiesser, H., R. Houze, and H. Huntrieser, 1995: The mesoscale structure of severe precipitation systems in Switzerland. *Mon. Wea. Rev.*, **123,** 2070-2097.

Trier, S. B., C. A. Davis, and J. D. Tuttle, 2000: Long-lived mesoconvective vortices and their environment. Part I: Observations from the Central United States during the 1998 warm season. *Mon. Wea. Rev.*, **128,** 3376-3395.

Trigo, I. F., T. D. Davies, and G. R. Bigg, 1999: Objective climatology of cyclones in the Mediterranean region. *J. Climate*, **12,** 1685-1696.

Trigo, I. F., G. R. Bigg , and T. D. Davies, 2002: Climatology of cyclogenesis in the Mediterranean. *Mon. Wea. Rev.*, **130,** 549-569.

Tuttle, J. D., R. E. Carbone, and P. A. Arkin, 2008: Comparison of ground-based radar and geosynchronous satellite climatologies of warm-season precipitation over the United States. *J. Appl. Meteor. Climatol.*, **47,** 3264-3270.

Wang, C.-C., G. T.-J. Chen, and R. E. Carbone, 2004: A climatology of warm season cloud patterns over east Asia based on GMS infrared brightness temperature observations. *Mon. Wea. Rev.*, **132,** 1606-1629.

Wang, C.-C., G. T.-J. Chen, and R. E. Carbone, 2005: Variability of warm-season cloud episodes over east Asia based on infrared brightness temperature observations. *Mon. Wea. Rev.*, **133**, 1478-1500.

Weiss, M., and E. A. Smith, 1987: Precipitation discrimination from satellite infrared temperatures over CCOPE mesonet region. *J. Climate Appl. Meteor.*, **26**, 687-697.

Wilks, D. S., 1995: *Statistical methods in the atmospheric sciences: An introduction*. Academic Press**,** 592 pp.

Wilson, J. W., and W. E. Schreiber, 1986: Initiation of convective storms at radar-observed boundary- layer convergence lines. *Mon. Wea. Rev.*, **114,** 2516-2536.

Wilson, J. W., R. E. Carbone, J. D. Tuttle, and T. D. Keenan, 2001: Tropical island convection in the absence of significant topography. Part II: Nowcasting. *Mon. Wea. Rev.*, **129,** 1637-1655.

Zhang, F., R. Yu, H. Chen, A. Dai, and Y. Pan, 2008: Summer precipitation frequency, intensity, and diurnal cycle over China: a comparison of satellite data with rain gauge observations. *J. Climate*, **21,** 3997-4010.

Acronyms

CAPE	Convective Available Potential Energy
DFT	Discrete Fourier Transform
ECMWF	European Centre for Medium-Range Weather Forecasts
EUMETSAT	European Organisation for the Exploitation of Meteorological Satellites
GMS-5	Geostationary Meteorological Satellite-5 (Japanese)
GOS	Global Observing Systems
IODC	Indian Ocean Data Coverage
IR	Infrared
MCC	Mesoscale Convective Complex
MCS	Mesoscale Convective System
MCV	Mesoscale Convective Vortex
MVIRI	Meteosat Visible and InfraRed Imager
NOAA	National Oceanic and Atmospheric Administration
NESDIS	National Environmental Satellite, Data and Information Service
QPF	Quantitative Precipitation Forecasting
RAMMB	Regional and Mesoscale Meteorology Branch
TOVS	TIROS-N Operational Vertical Sounder
VIS	Visible
WSR-88D	Weather Surveillance Radar-88 Doppler
WV	Water Vapour
WWRP	World Weather Research Programme

Appendix A – Yearly maps of cold clouds persistence

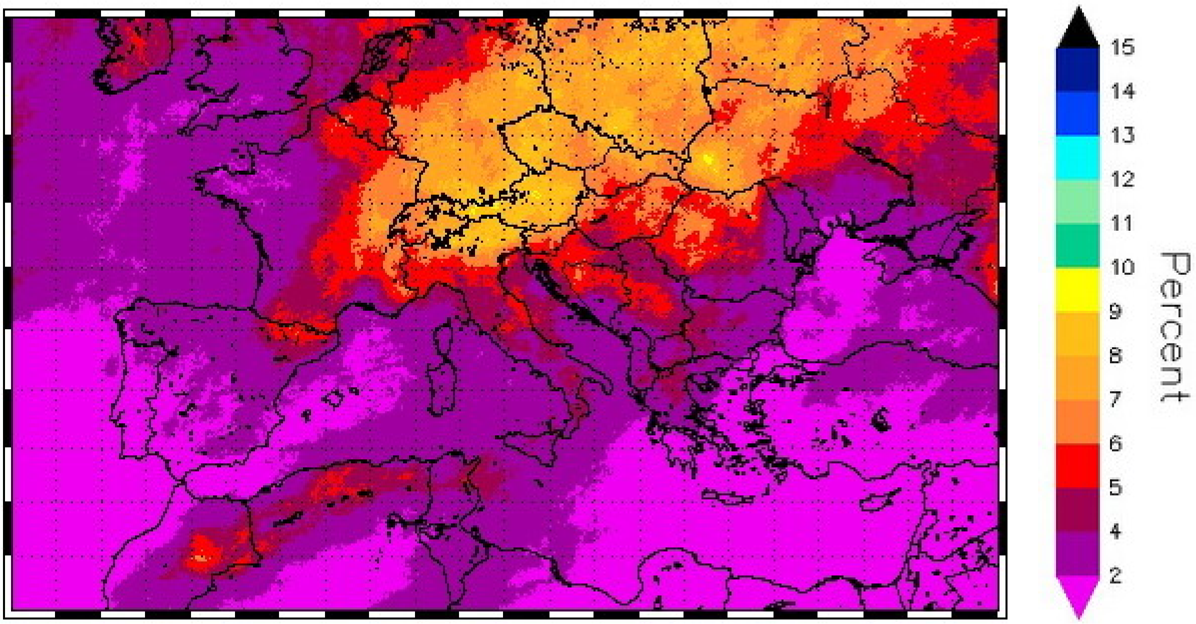

Figure A - 1 *Average cold cloud percentage persistence over the period May-August 1996.*

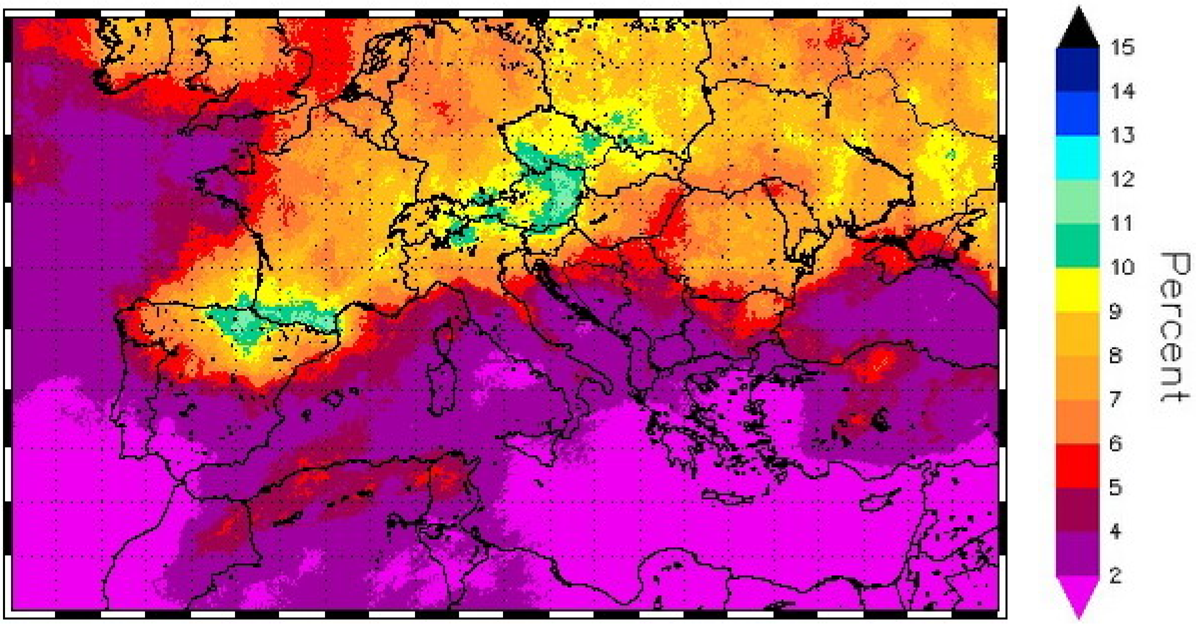

Figure A - 2 *Same as in Fig. A-1 but for the period May-August 1997.*

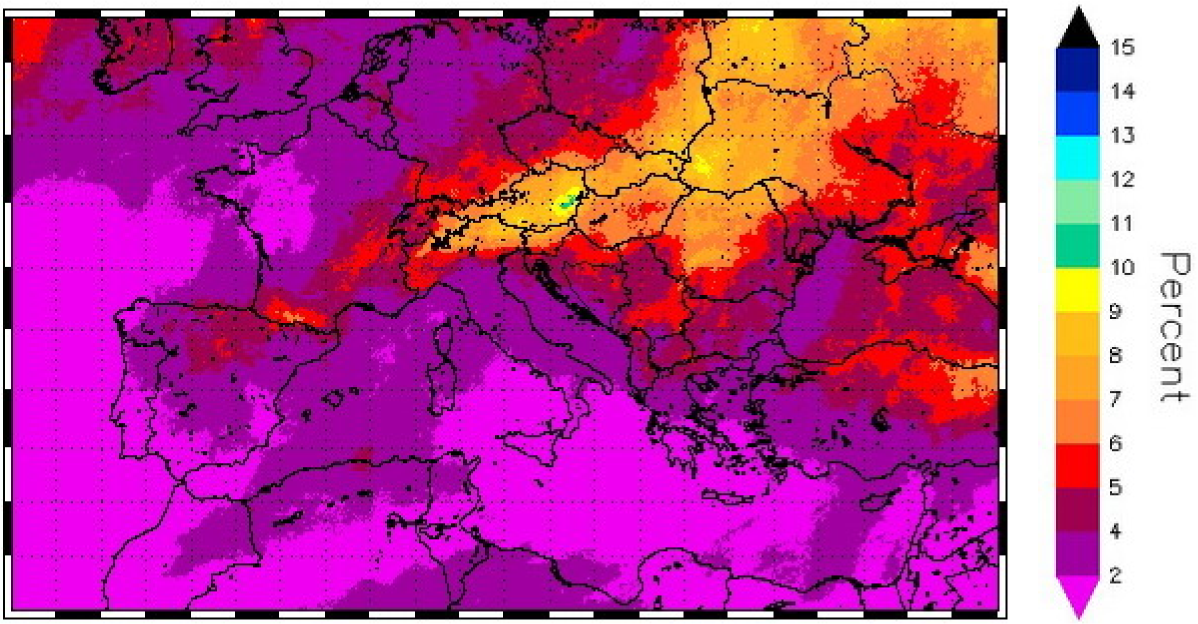

Figure A - 3 *Same as in Fig. A-1 but for the period May-August 1998.*

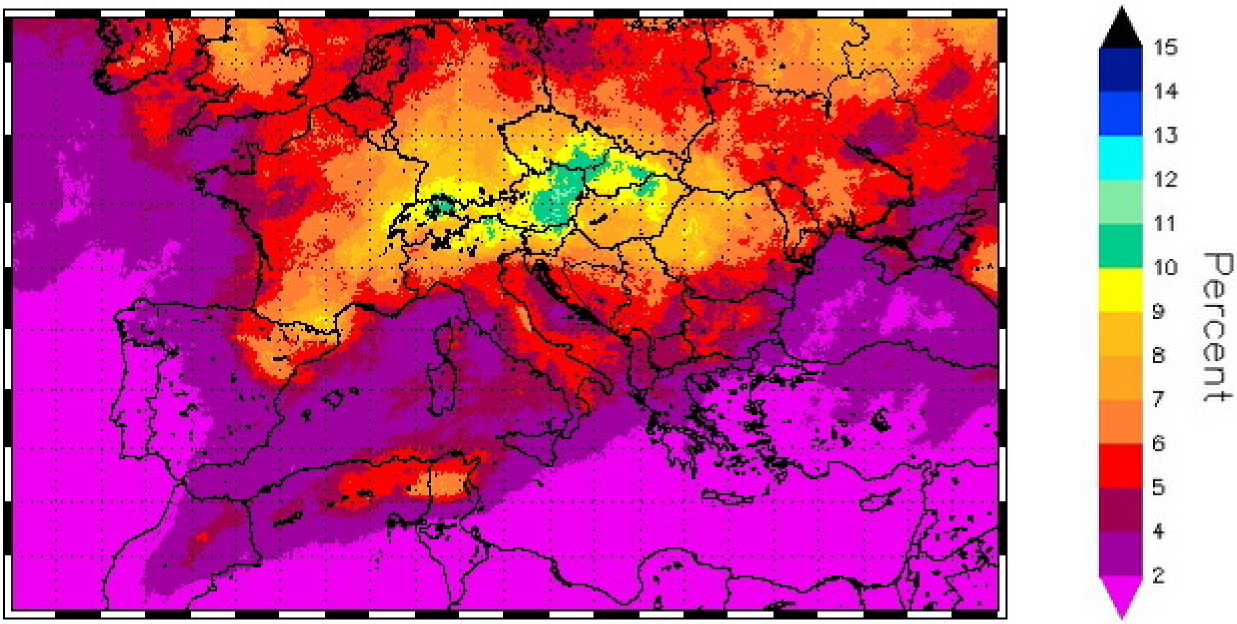

Figure A - 4 *Same as in Fig. A-1 but for the period May-August 1999.*

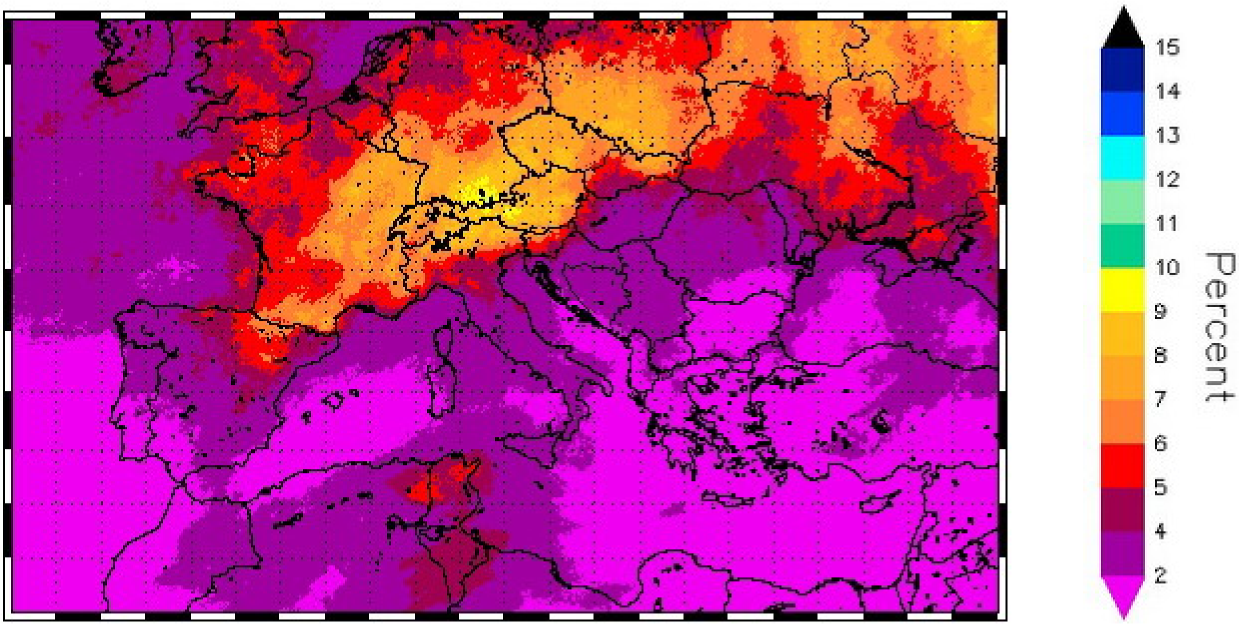

Figure A - 5 *Same as in Fig. A-1 but for the period May-August 2000.*

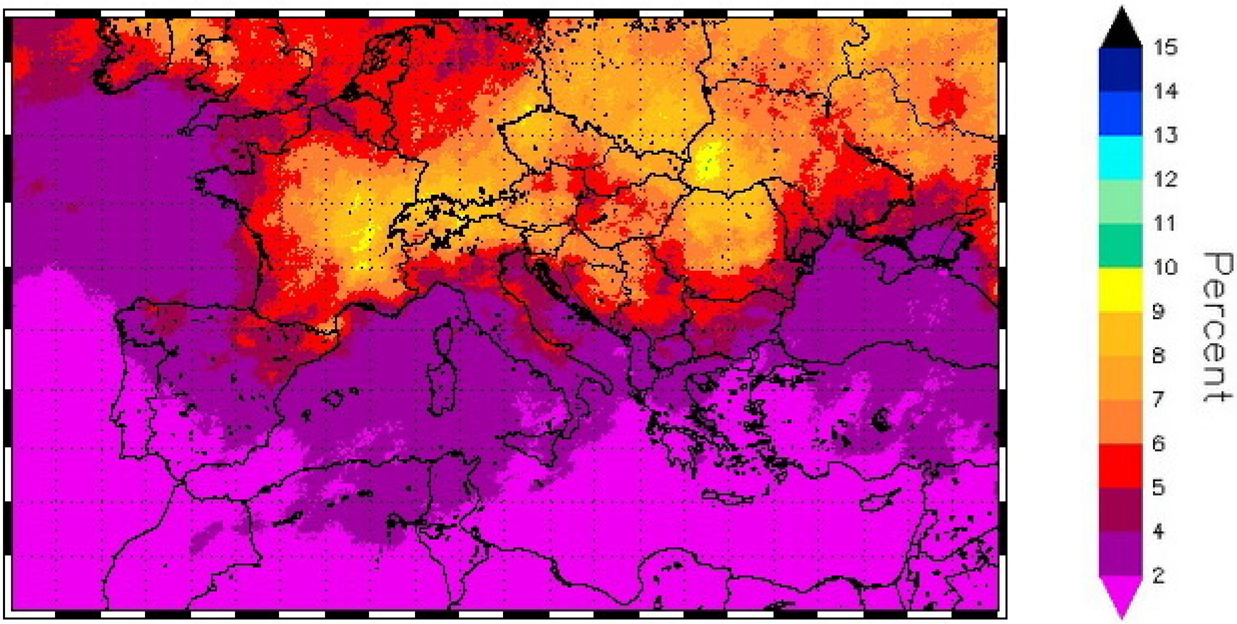

Figure A - 6 *Same as in Fig. A-1 but for the period May-August 2001.*

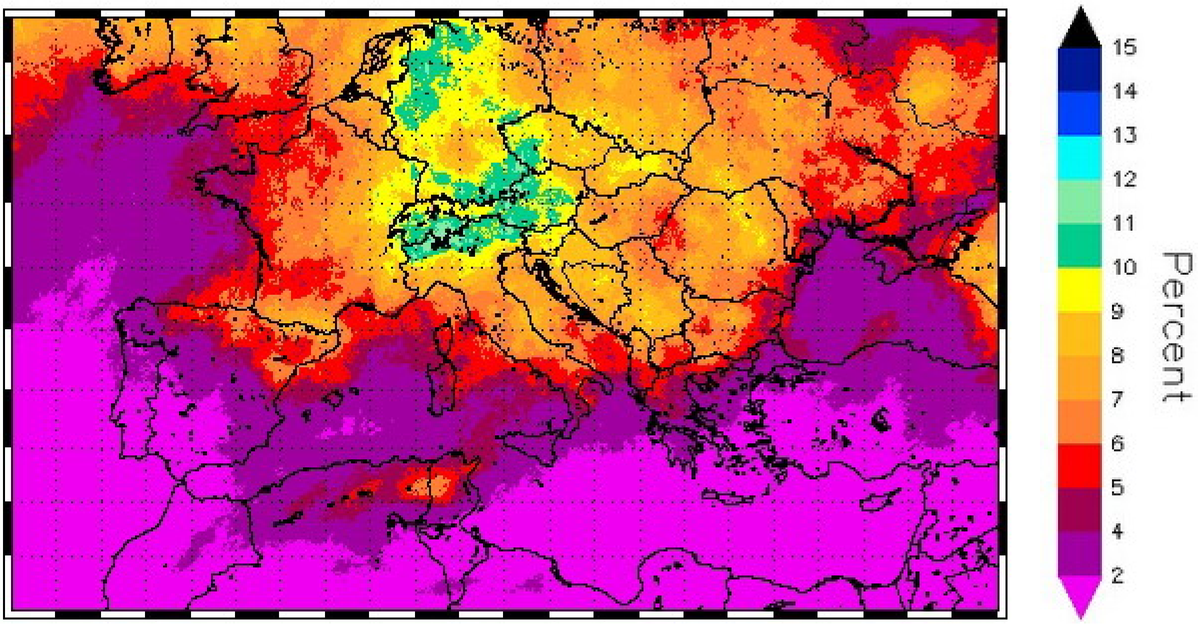

Figure A - 7 *Same as in Fig. A-1 but for the period May-August 2002.*

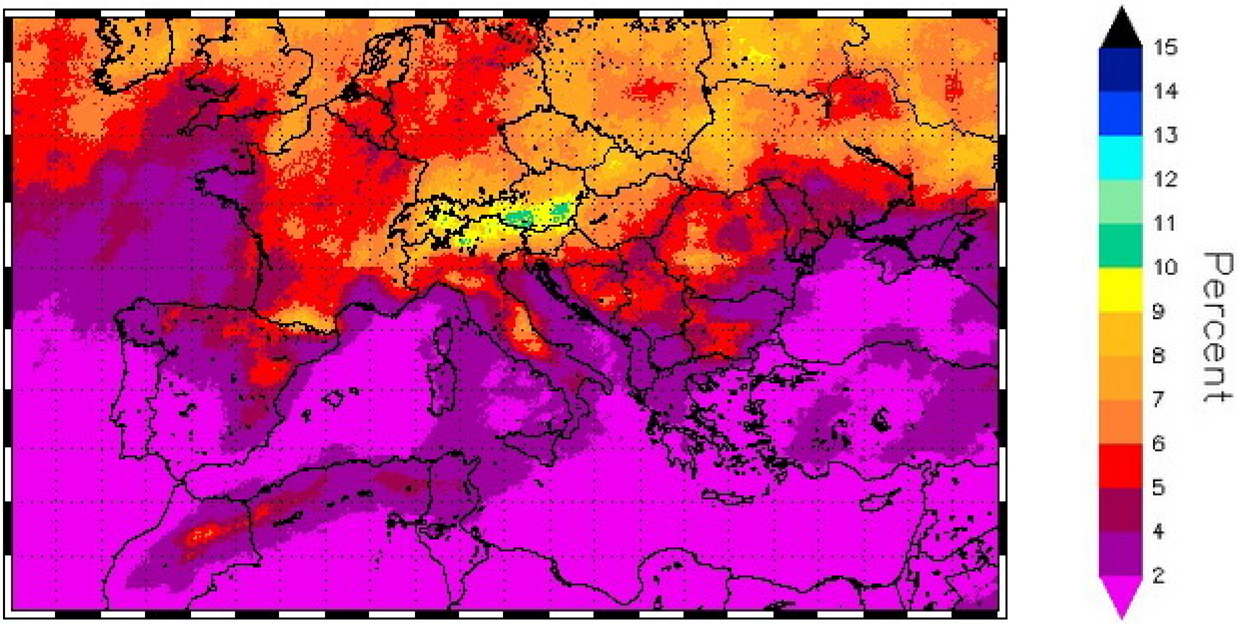

Figure A - 8 *Same as in Fig. A-1 but for the period May-August 2003.*

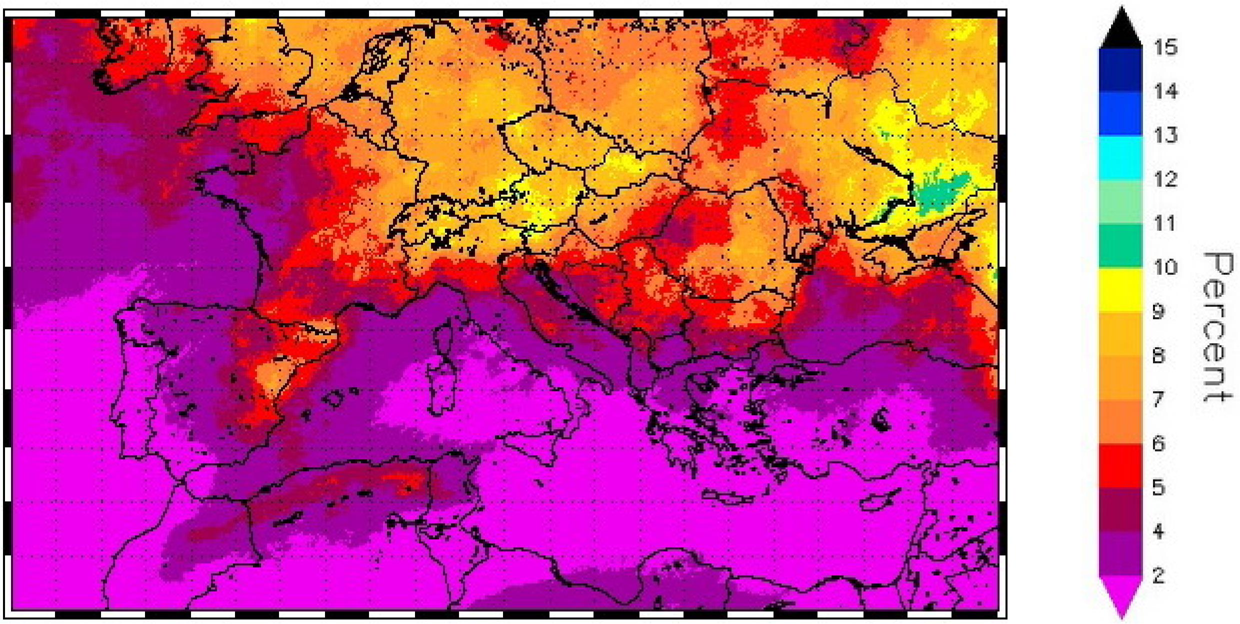

Figure A - 9 *Same as in Fig. A-1 but for the period May-August 2004.*

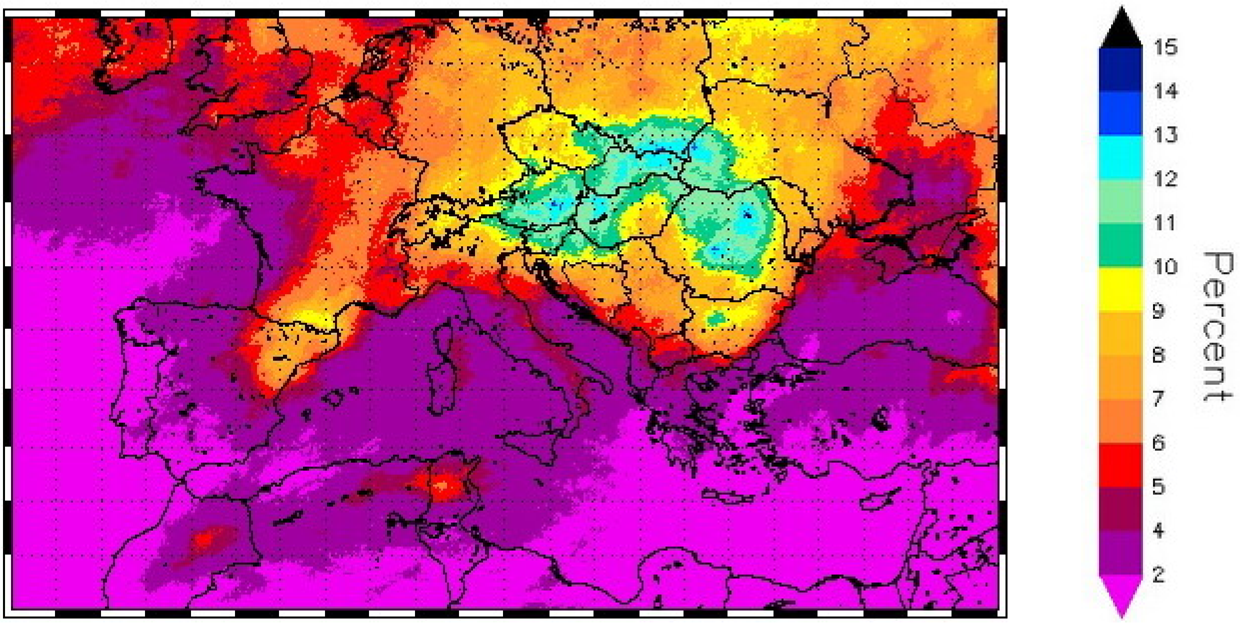

Figure A - 10 *Same as in Fig. A-1 but for the period May-August 2005.*

Appendix B – Yearly diurnal cold clouds (T_b < 241 K) frequency Hovmöller diagrams

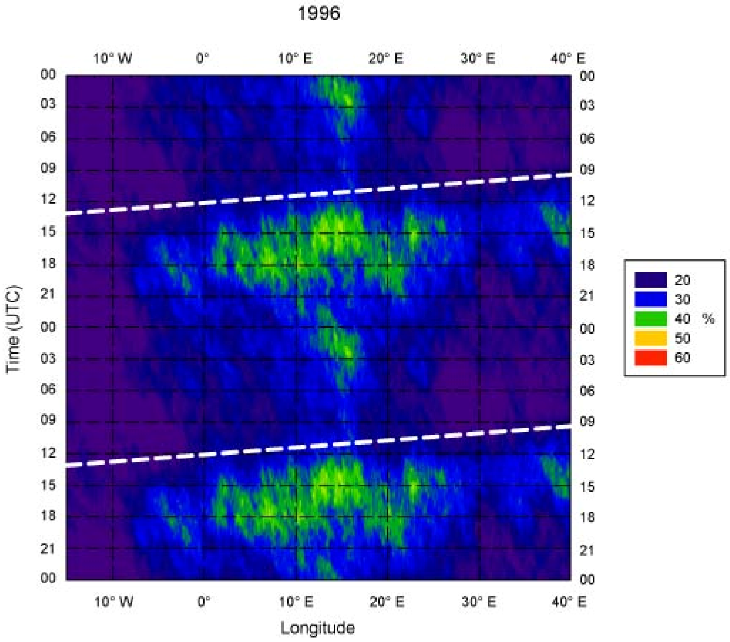

Figure B - 1 *Average diurnal cold cloud frequency Hovmöller diagram for the period May-August 1996. The scale corresponds to the percentage of days during which clouds are present at a given longitude-UTC time. The local noon is indicated by dashed lines.*

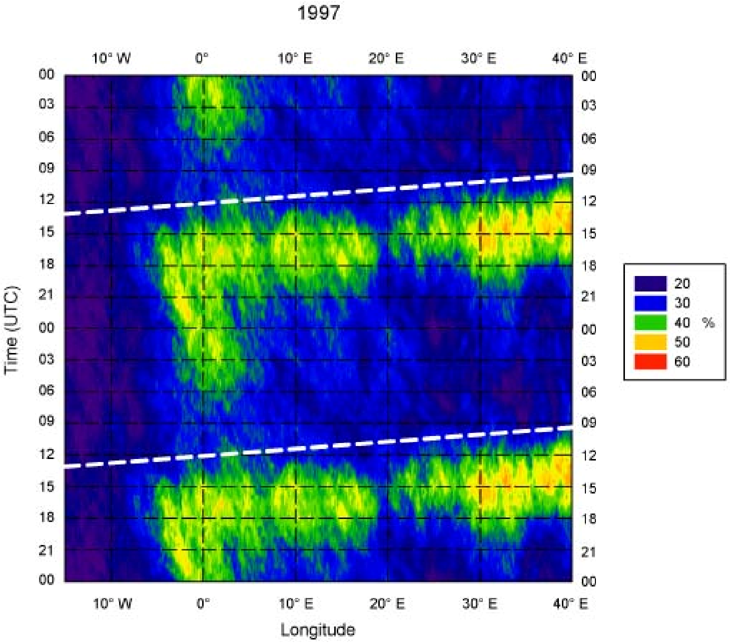

Figure B - 2 *Same as in Fig. B-1 but for May-August 1997.*

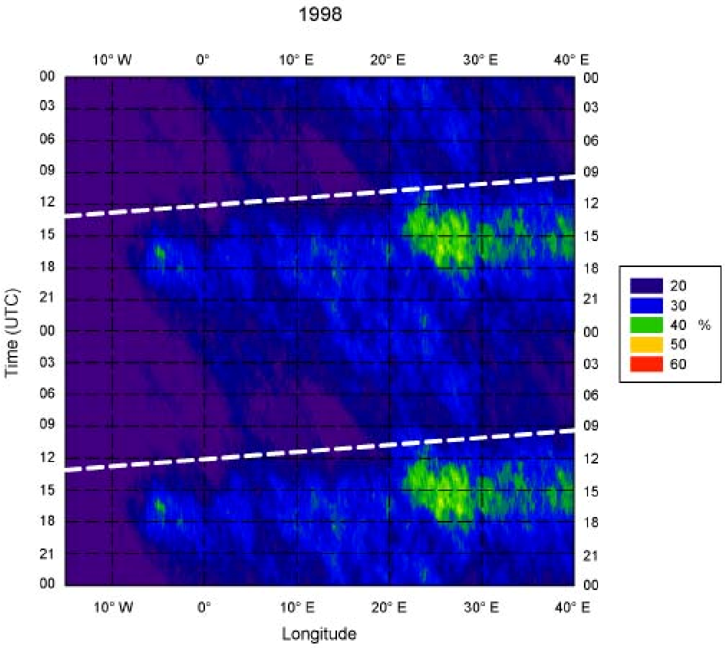

Figure B - 3 *Same as in Fig. B-1 but for May-August 1998.*

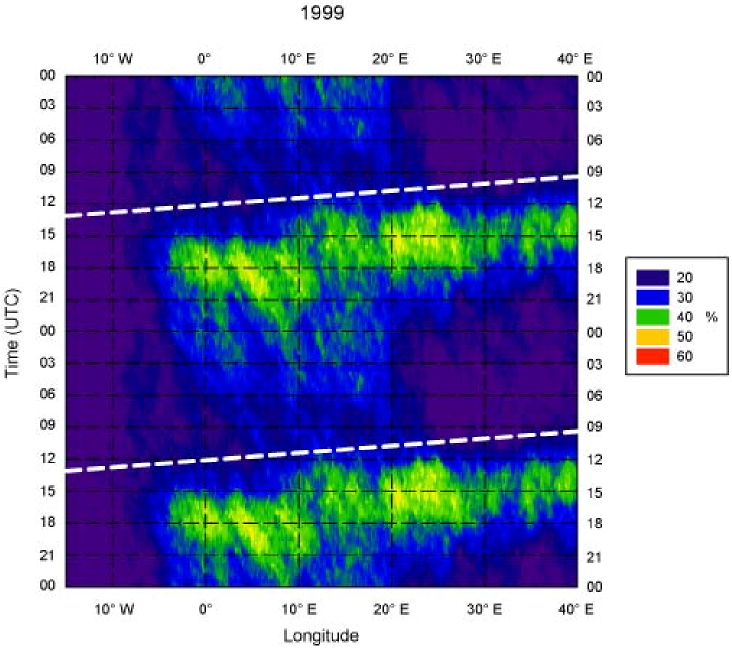

Figure B - 4 *Same as in Fig. B-1 but for May-August 1999.*

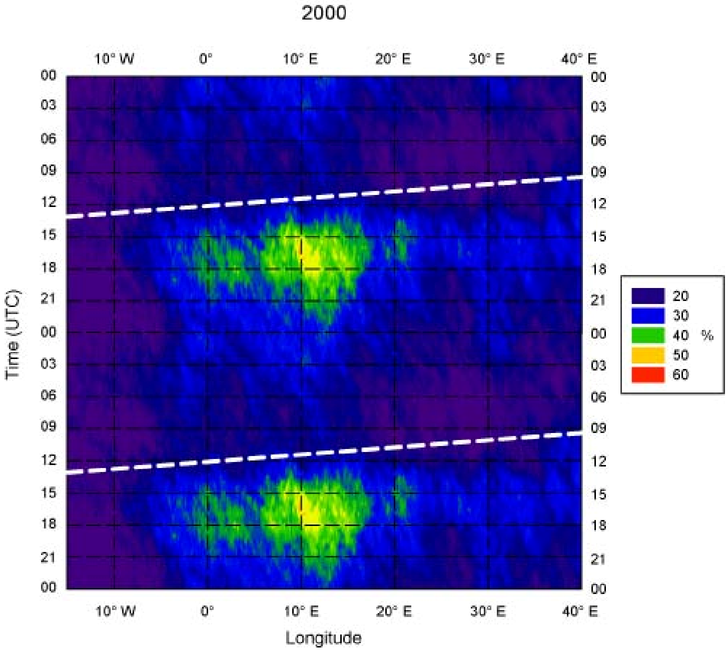

Figure B - 5 *Same as in Fig. B-1 but for May-August 2000.*

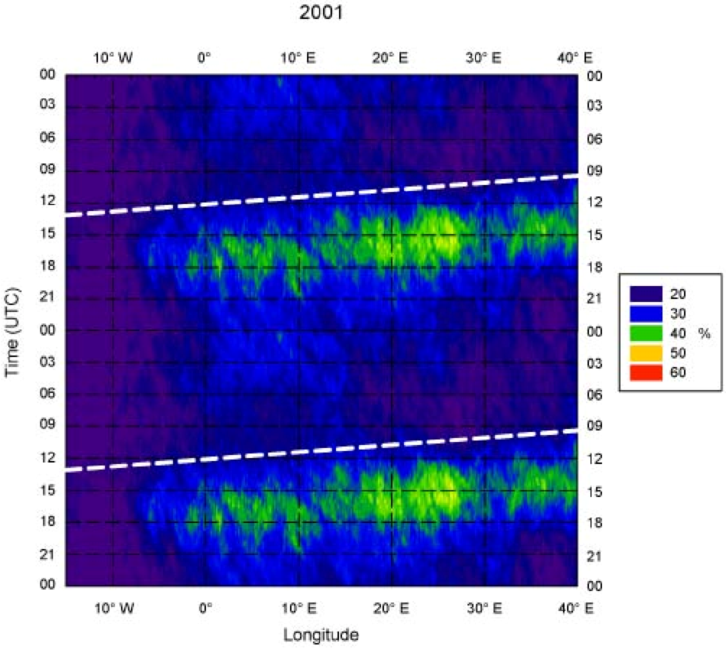

Figure B - 6 *Same as in Fig. B-1 but for May-August 2001.*

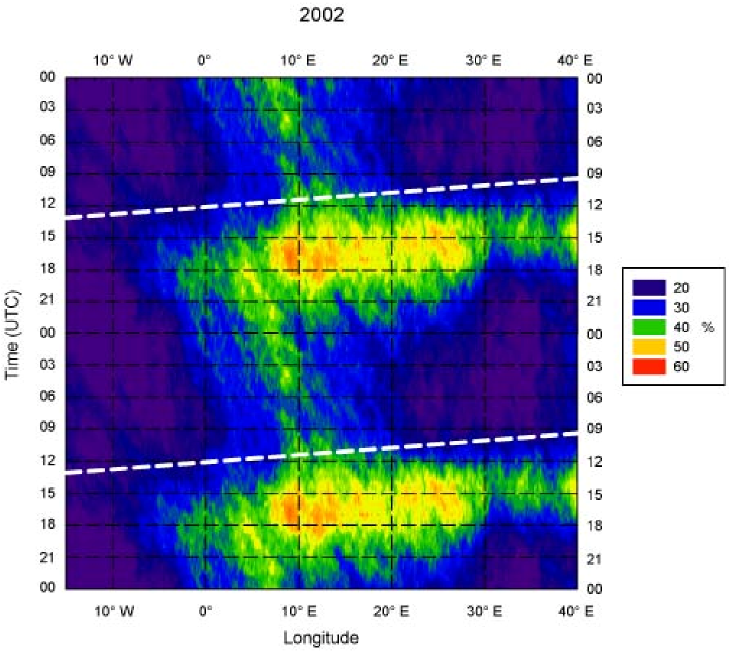

Figure B - 7 *Same as in Fig. B-1 but for May-August 2002.*

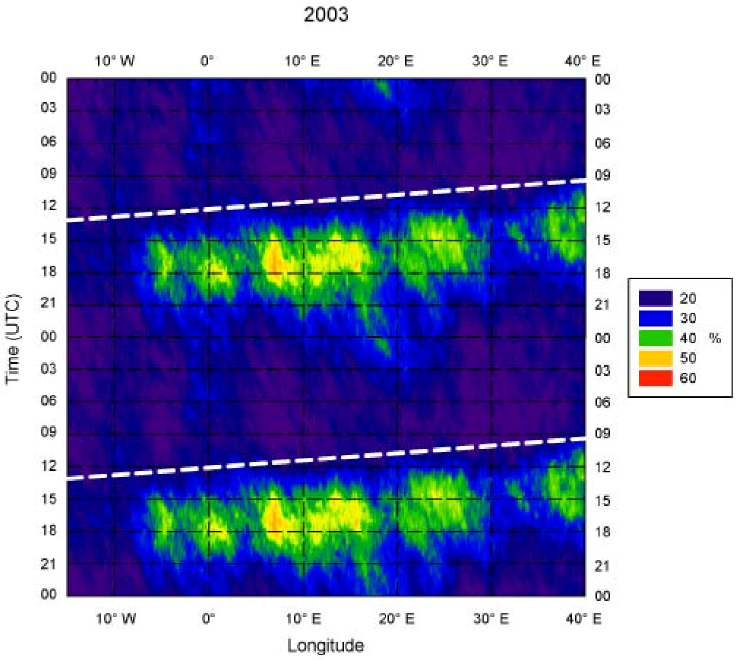

Figure B - 8 *Same as in Fig. B-1 but for May-August 2003.*

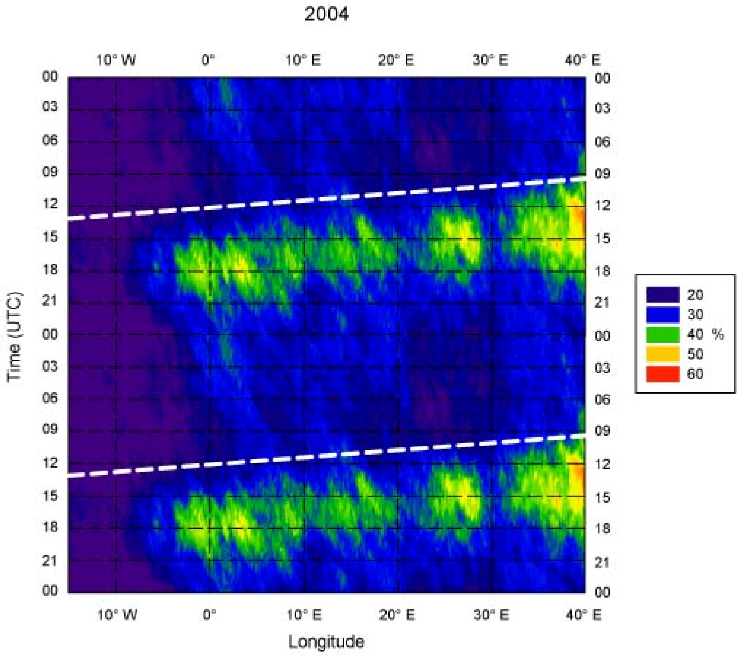

Figure B - 9 *Same as in Fig. B-1 but for May-August 2004.*

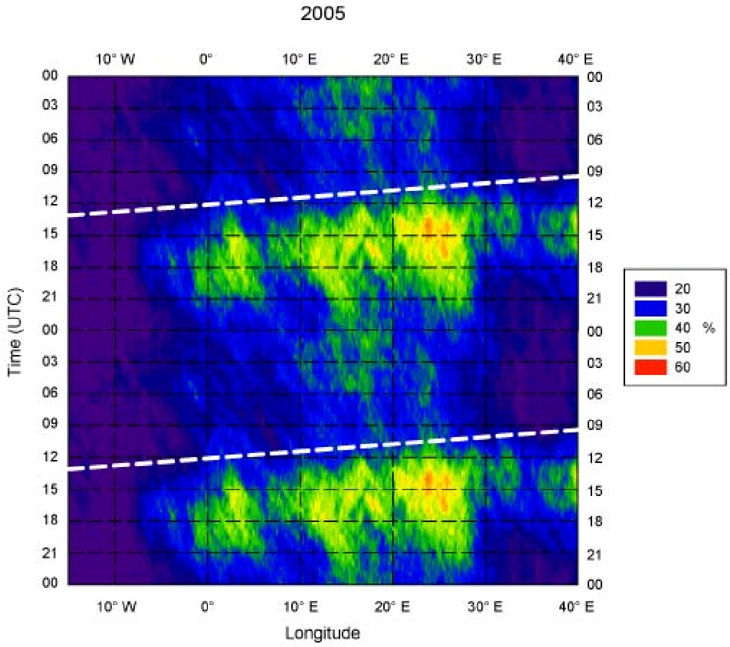

Figure B - 10 *Same as in Fig. B-1 but for May-August 2005.*